THERMAL TRANSPORT PROPERTIES OF INDIVIDUAL NANOWIRES

BUI CONG TINH

(B.Sc - Vietnam National University of Hanoi, Vietnam)

A Thesis Submitted for the Degree of Doctor of Philosophy

NUS GRADUATE SCHOOL FOR INTEGRATIVE SCIENCES

AND ENGINEERING

NATIONAL UNIVERSITY OF SINGAPORE

2011

Acknowledgments

First of all, I would like to thank my supervisor, Professor Li Baowen, and my co-supervisors, Professor Andrew Tay A. O. and Associate Professor John Thong Thiam Leong, for their inspiring and encouraging way in guiding me to understand and carry out the research work. Their guidance and comments over the duration of my graduate study are invaluable for me. I would also like to thank the chairman of my thesis advisory committee, Prof Wu Yihong, for his valuable advice in the course of my work.

I also would like to thank staff members, Mrs. Ho Chiow Mooi, Mr. Koo Chee Keong, Ms. Linn Linn, Mr. Wang Lei, Dr. Hao Yu Feng, and Dr. Sinu Mathew, and students, Mr. Wang Ziqian, Mr. Wang Rui, Ms. Liu Dan, Mr. Wang Jiayi, in CICFAR lab for their help, support, and fruitful discussions. Especially, I would like to express my deepest appreciation to Dr. Xie Rongguo who helped me with the experimental work, and with whom I had many discussions

I would like to thank Dr. Zhang Qingxin for his supervision and instruction during my research attachment at the Institute of Microelectronics, Agency for Science, Technology and Research, Singapore.

Finally, I would like to express my gratitude to my parents who have been behind me at every stage, providing unwavering support.

Table of Contents

Summary

This thesis aims to study thermal transport in various kinds of nanowires (NWs) to elucidate phonon transport in quasi one-dimensional nanostructures. The thermal transport properties of zinc oxide (ZnO), vanadium dioxide (VO_2), and silicon (Si) NWs are reported in this thesis. The correlation between electrical and thermal properties in metal-insulator transition VO_2 NWs is also studied in the vicinity of transition temperature. All the thermal and electrical measurements were carried out using a home-made measurement set-up and micro-electro-thermal system (METS) devices.

Thermal conductivities of individual single crystalline ZnO NW with different diameters were measured over a temperature range of 77 – 400K. The measured thermal conductivities of the ZnO NWs are more than one order of magnitude lower than that of bulk ZnO. With decreasing diameter, the corresponding thermal conductivity is reduced over the entire measured temperature range due to phonon boundary scattering. It is found that the thermal conductivity is approximately linear with the cross-sectional area of the NWs in the measured diameter range. The results show that boundary scattering is dominant at low temperature, and Umklapp scattering, which reduces the thermal conductivity with temperature, becomes important and comes to dominate at higher temperature. Impurity scattering (including isotope scattering) and Umklapp scattering become increasingly significant at intermediate and high temperatures. The thermal conductivities of the ZnO NWs are found to be insensitive to the surface amorphous carbon coating but are greatly degraded by ion irradiation at even low dose.

The experimental results of both thermal and electrical properties of single

crystalline VO_2 NWs have shown many interesting phenomena in the vicinity of metal-insulator-transition (MIT) temperature. The NWs exhibit either single domain or co-existing metal-insulator domains depending on temperature sweeping conditions. A reduction in electrical resistance after several measurements indicates that metallic domains are pinned inside the NW. A mechanism is proposed to explain the pinning effect. Interestingly, a strong external uniaxial tensile stress applied to the NW can mostly recover the resistance, which indicates that the pinned metallic domains are released. Thermal property measurements in the low temperature range (77 – 300 K) show that the thermal conductivity of NW decreases approximately with temperature as $\sim T^{1.5}$. The thermal conductivity of VO_2 NW with pinned metallic domains increases by about 15% across the MIT temperature which is different from that observed in bulk VO_2, the latter showing minimal changes..

The thermal conductivity of Si NWs of different diameters was measured. The thermal conductivity scales linearly with temperature in the temperature range of 77 K to 120 K, which is opposed to the T^3 dependence predicted by Debye's model for phonon transport. Meanwhile, in the high temperature range beyond the peak temperature, the thermal conductivity decreases approximately with temperature as $T^{1.5}$. The thermal conductivity decreases significantly for small NW, which indicates strong boundary scattering in thin wires. Under ion beam irradiation, an amorphous region was created in the surface layer of the NW due to the collision cascade between the incident ions and the lattice atoms. We observe significant reduction of thermal conductance of the wires, which is attributed to the shrinkage of the crystalline part of the NW and the enhanced phonon boundary scattering at the amorphous – crystalline interface.

List of Tables

List of Figures

Nomenclature

1-D	One-Dimensional
AFM	Atomic Force Microscopy
BTE	Boltzmann Transport Equation
CNT	Carbon Nanotube
DIP	Dual In-line Package
DUV	Deep Ultraviolet
EBIC	Electron Beam Induced Conductivity
EBID	Electron Beam Induced Deposition
FET	Field Effect Transistor
FIB	Focused Ion Beam
FIBID	Focused Ion Beam Induced Deposition
HRTEM	High Resolution Transmission Electron Microscope
IC	Integrated Circuit
LA	Longitudinal Acoustic
MD	Molecular Dynamics
MEMS	Micro-Electro-Mechanical Systems
METS	Micro-Electro-Thermal System
MicroPL	Micro-Photoluminescence
MIT	Metal-Insulator Transition
MOS	Metal-Oxide-Semiconductor
NT	Nanotube
NW	Nanowire
PECVD	Plasma Enhanced Chemical Vapor Deposition
PRT	Platinum Resistance Thermometer

PTC	Platinum Coil
RIE	Reactive Ion Etching
SAED	Selected Area Electron Diffraction
SEAM	Scanning Electron Acoustic Microscopy
SEM	Scanning Electron Microscope / Microscopy
SMU	Source Measurement Unit
SPM	Scanning Probe Microscope
SREP	Spatially Resolved Electron-beam Probing
SRIM	Stopping and Range of Ions in Matters
TA	Transverse Acoustic
TCR	Temperature Coefficient of Resistance
TE	Thermoelectric
TEM	Transmission Electron Microscope / Microscopy
VLS	Vapor-Liquid-Solid
VPT	Vapor Phase Transport

Chapter 1: Introduction

Nanoscale materials such as two-dimensional quantum well structures, one-dimensional nanowires (NWs) and nanotubes (NTs), and zero-dimensional quantum dots have attracted considerable attention in the past few decades. With the availability of many methods for nanomaterial synthesis as well as powerful observation and manipulation tools such as the scanning electron microscope (SEM), the transmission electron microscope (TEM), and various scanning probe microscopies (SPM), many intriguing properties of nanomaterials have been discovered and investigated thoroughly. Among them, one-dimensional (1-D) nanoscale materials (NWs, NTs) have stimulated great interest due to their importance in fundamental scientific researches [1 – 3]. NWs with their unusual mechanical, optical, electrical, and thermal properties hold promise for potential applications in nanoscale electronics, optoelectronics, photonics, sensors, and energy conversion devices [4 – 8]. NWs are also interesting systems for investigating the dependence of various physical properties on size and dimensionality. Among the physical properties of interest, relatively less research has been carried out on the thermal transport properties of NWs. Even though there has been a recent spate of theoretical and numerical studies on thermal transport in various NWs [9 – 15], experimental data is still lacking.

For NWs, the thermal conductance can be suppressed due to two primary reasons. First, as the diameter of the wire reduces to the order of the phonon mean free path in the bulk material (order of 10 nm or 100 nm), phonon scattering by the boundary increases, which reduces the thermal conductivity of the NWs [12]. The

second reason for thermal conductivity suppression in NWs is size confinement which modifies the phonon frequency versus wave-vector dispersion relation from that of the bulk material, and consequently reduces the phonon group velocity [15]. The suppressed thermal conductivity of NWs has positive implications if applied to thermoelectric (TE) devices which could convert waste heat to electricity. Recently, anomalous thermal and thermoelectric properties of silicon NWs have been reported [16, 17], in which the thermal conductivity of 50 nm silicon NWs with rough surfaces is 100 times lower than that of bulk silicon, without significant changes in the electrical conduction and the power factor, yielding a thermoelectric figure of merit $ZT = 0.6$ at room temperature. These results make rough silicon NWs as efficient TE materials and are expected to apply to other types of semiconductor NWs. Exploring new NW materials for TE applications requires further investigation on thermal transport and thermoelectric properties of various semiconductor NWs.

Another abnormal phenomenon observed in 1-D nanostructures is thermal rectification which recently attracted a lot of interest in the research community. Thermal rectifying effects were discovered in 1-D heterostructures through both simulation [18, 19] and experiment [20]. Subsequent simulation studies on one-dimensional nanostructures have shown the principles of thermal diodes, thermal transistors [21], thermal logic gates [22], and thermal memory [23], which could be the fundamental components in phononic information processing. Although the thermal rectification effect has been experimentally observed in NT with non-uniform axial mass distribution, the rectification is, however, relatively small (~ 7%) [20]. In order to experimentally realize large thermal rectification effect, further efforts need to be focused on the study and deep understanding of thermal transport in various asymmetrical 1-D nanostructures.

Understanding nanoscopic heat transport is also very important in nanoscale electronic devices and integrated circuits (ICs). Increasing integration accompanied by decreasing transistor feature sizes lead to a heat management problem. The amount of heat energy transported away from a given device and a circuit is limited by the thermal conductance of circuit elements with nanoscale dimensions and thermal interfaces. Thermal modeling based on bulk material parameters and Fourier's Law is unlikely to yield accurate results at nanoscopic dimensions, a problem that will be further exacerbated with further device scaling.

Motivated by these considerations, in this thesis we systematically investigate the thermal transport properties of 3 types of NWs, namely, zinc oxide (ZnO), silicon (Si), and vanadium dioxide (VO_2) NWs. ZnO NWs are of great interest as a wide band gap semiconductor, and there is no experimental work done on their thermal conductivity so far. On the other hand, while thermal transport studies have been carried out on Si NWs, more experimental data are required to validate some proposed theoretical models. Furthermore, this thesis sets out to study the impact of modifications to the surface morphology on the thermal conductivity of Si NWs. Lastly, the metal-insulator transition in VO_2 NWs presents an interesting opportunity to explore the correlation between their electrical and thermal properties around the transition temperature.

To measure the thermal and electrical properties of such nanostructures, micro characterization devices were designed and fabricated, and a measurement system was established. The contributions of different phonon scattering mechanisms are discussed in light of the experimental results. The effects of surface coating and ion beam irradiation on thermal transport of NWs were also studied. The thermal

transport properties correlated with electrical properties in VO_2 NWs were also studied by utilizing the four-point electrical contacts integrated within the thermal characterization devices. The aim of this work is to elucidate the underlying mechanisms of thermal transport in individual NWs. This understanding will provide useful information for the design of NW-based applications.

This thesis is organized as follows. Chapter 2 covers the background of phonon transport in bulk crystals and in NWs. The design and fabrication of the micro characterization device, the experimental setup, and the measurement approach to determine the thermal conductance and electrical properties of NWs are described in Chapter 3. Chapter 4 presents the thermal conductivity results for single-crystalline ZnO NWs and examines the effects of surface coating and ion beam irradiation on thermal transport properties. The electrical and thermal properties of metal-insulator-transition VO_2 NWs in the vicinity of transition temperature are presented in Chapter 5, in which the phenomenon of room temperature metallic domains pinned in NWs is discussed. In Chapter 6, we present a study on the thermal conductivity of individual single crystalline Si NWs, where the NWs were further irradiated with gallium (Ga) ions thereby significantly affecting their thermal conductance. Finally, Chapter 7 concludes the thesis and proposes future work that can be carried out to deepen our understanding of heat transfer in NWs.

References

1. Xia, Y.; Yang, P.; Sun, Y.; Wu, Y.; Mayers, B.; Gates, B.; Yin, Y.; Kim, F.; and Yan, H.; "One-Dimensional Nanostructures: Synthesis, Characterization, and Applications", *Adv. Mater.* Vol. 15, pp. 353 – 389, 2003.

2. Zhang, Z.; Sun, X.; Dresselhaus, M. S.; and Ying, J. Y.; "Electronic Transport Properties of Single-Crystal Bismuth Nanowire Arrays", *Phys. Rev. B* Vol. 61, pp. 4850 – 4861, 2000.

3. Kim, P.; Shi, L.; Majumdar, A.; and McEuen, P. L.; "Thermal Transport Measurements of Individual Multiwalled Nanotubes", *Phys. Rev. Lett.* Vol. 87, 215502, 2001.

4. Sirbuly, D. J.; Law, M.; Yan, H.; and Yang, P.; "Semiconductor Nanowires for Subwavelength Photonics Integration", *J. Phys. Chem. B* Vol. 109, pp. 15190 – 15213, 2005.

5. Duan, X.; Huang, Y.; Wang, J.; and Lieber, C. M.; "Indium Phosphide Nanowires as Building Blocks for Nanoscale Electronic and Optoelectronic Devices", *Nature* Vol. 409, pp. 66 – 69, 2001.

6. Huang, M. H.; Mao, S.; Feick, H.; Yan, H.; Wu, Y.; Kind, H.; Weber, E.; Russo, R.; and Yang, P.; "Room-Temperature Ultraviolet Nanowire Nanolasers", *Science* Vol. 292, pp. 1897 – 1899, 2001.

7. Cui, Y.; and Lieber, C. M.; "Functional Nanoscale Electronic Devices Assembled Using Silicon Nanowire Building Blocks", *Science* Vol. 291, pp. 851 – 853, 2001.

8. Dresselhaus, M. S.; Lin, Y. M.; Cronin, S. B.; Rabin, O.; Black, M. R.; Dresselhaus, G.; and Koga, "Quantum Wells and Quantum Wires for Potential Thermoelectric Applications", *Semiconductors and Semimetals* Vol. 71, pp. 1 – 121, 2001.

9. Walkauskas, S. G.; Broido, D. A.; Kempa, K.; and Reinecke, T. L.; "Lattice Thermal Conductivity of Wires", *J. Appl. Phys.* Vol. 85, pp. 2579 – 2582, 1999.

10. Chen, Y.; Li, D.; Yang, J.; Wu, Y.; and Lukes, J. R.; "Molecular Dynamics Study of the Lattice Thermal Conductivity of Kr/Ar Superlattice Nanowires", *Physica B-Condensed Matter* Vol. 349, pp. 270 – 280, 2004.

11. Mingo, N.; Yang, L.; Li, D.; and Majumdar, A.; "Predicting the Thermal Conductivity of Si and Ge Nanowires", *Nano Lett.* Vol. 3, pp. 1713 – 1716, 2003.

12. Volz, S. G.; and Chen, G.; "Molecular Dynamics Simulation of Thermal Conductivity of Silicon Nanowires", *Appl. Phys. Lett.* Vol. 75, pp. 2056 – 2058, 1999.

13. Zou, J.; and Balandin, A.; "Phonon Heat Conduction in a Semiconductor Nanowire", *J. Appl. Phys.* Vol. 89, pp. 2932 – 2938, 2001.

14. Mingo, N.; “Calculation of Si Nanowire Thermal Conductivity Using Complete Phonon Dispersion Relations”, *Phys. Rev. B* Vol. 68, 113308, 2003.

15. Khitun, A.; Balandin, A.; and Wang, K. L.; “Modification of the Lattice Thermal Conductivity in Silicon Quantum Wires due to Spatial Confinement of Acoustic Phonons”, *Superlatt. Microstruct.* Vol. 26, pp. 181 – 193, 1999.

16. Boukai, A. I.; Bunimovich, Y.; Tahir-Kheli, J.; Yu, J. K.; Goddard, W. A.; and Heath, J. R.; “Silicon Nanowires as Efficient Thermoelectric Materials”, *Nature* Vol. 451, pp. 168 – 171, 2008.

17. Hochbaum, A. I.; Chen, R.; Delgado, R. D.; Liang, W.; Garnett, E. C.; Najarian, M.; Majumdar, A.; and Yang, P.; “Enhanced Thermoelectric Performance of Rough Silicon Nanowires”, *Nature* Vol. 451, pp. 163 – 167, 2008.

18. Li, B.; Lan, J.; and Wang, L.; “Interface Thermal Resistance Between Dissimilar Anharmonic Lattices”, *Phys. Rev. Lett.* Vol. 95, 104302, 2005.

19. Li, B.; Wang, L.; and Casati, G.; “Thermal Diode: Rectification of Heat Flux”, *Phys. Rev. Lett.* Vol. 93, 184301, 2004.

20. Chang, C. W.; Okawa, D.; Majumdar, A.; and Zettl, A.; “Solid-State Thermal Rectifier”, *Science* Vol. 314, pp. 1121 – 1124, 2006.

21. Li, B.; Wang, L.; and Casati, G.; “Negative Differential Thermal Resistance and Thermal Transistor”, *Appl. Phys. Lett.* Vol. 88, 143501, 2006.

22. Wang, L.; and Li, B.; “Thermal Logic Gates: Computation with Phonons”, *Phys. Rev. Lett.* Vol. 99, 177208, 2007.

23. Wang, L.; and Li, B.; “Thermal Memory: A Storage of Phononic Information”, *Phys. Rev. Lett.* Vol. 101, 267203, 2008.

Chapter 2: Background and Literature Review

In this chapter, we present a review of the experimental and theoretical works on thermal transport in one-dimensional (1-D) nanostructures, such as nanowires (NWs) and nanotubes (NTs). In particular, phonon scattering mechanisms and models of thermal transport in 1-D nanostructures are discussed.

2.1. Lattice thermal conductivity

Heat conduction in nanostructures is due to transport of energy carriers such as phonons and free electrons. While heat transport in metals is mainly due to electrons, for non-metallic crystals such as semiconductors or insulators, the heat transport is usually dominated by phonons. By definition, phonons are the quanta of excitations of the normal modes of lattice vibration. In heavily doped semiconductors, although the electronic contribution to heat conduction may become significant, most of the heat is still carried by phonons [1]. In real lattice crystals, phonons do not travel directly in a straight path from one end to the other end but scatter with other phonons, impurity atoms, defects, boundaries or electrons. The scattering events induce a resistance to the energy transport by phonons and give rise to finite phonon thermal conductivity. Phonon transport in a crystal behaves similar to that of gas molecules in a container, and can be treated by kinetic theory [2]. From the kinetic theory of gas, the flux of particles in the x direction is $\frac{1}{2} n \left\langle \left| v_x \right| \right\rangle$, where n is the concentration of molecules, and $\left\langle ... \right\rangle$ denotes average value. When moving from a region at local temperature $T + \Delta T$ to a region at local temperature T, a particle will give up energy of $c\Delta T$, where c is the

specific heat of the particle. The temperature difference between the ends of a free path of the particle is given by

$$\Delta T = \frac{dT}{dx} l_x = \frac{dT}{dx} v_x \tau \tag{2.1}$$

where τ is the average time between collisions. The flux of energy (heat flux) is

$$q_x = -n \left\langle v_x^2 \right\rangle c\tau \frac{dT}{dx} = -\tfrac{1}{3} n \left\langle v^2 \right\rangle c\tau \frac{dT}{dx} \tag{2.2}$$

If v is constant, the heat flux becomes

$$q_x = -\frac{1}{3} Cvl \frac{dT}{dx} \tag{2.3}$$

where $l = v\tau$ is the phonon mean free path, and $C = nc$ is the lattice specific heat of the material. The thermal conductivity is simply

$$k = -\frac{1}{3} Cvl \tag{2.4}$$

The specific heat of the material can be expressed via the phonon density of states as [2]:

$$C = \sum_p \int \frac{d < n >_p}{dT} \hbar \omega_p D_p(\omega) d\omega \tag{2.5}$$

The density of states $D(\omega)$ is usually a very complex function of frequency which can be obtained by measuring the dispersion relation, ω versus the wave vector K, in selected crystal directions by inelastic neutron scattering and then analytical fitting to give the dispersion relation in a general direction. The most famous theoretical modeling for the specific heat calculation is the Debye model, in which the velocity of

sound is taken as constant for each polarization type $\omega = vK$. With that assumption, the specific heat can be rewritten as:

$$C = \frac{3V\hbar^2}{2\pi^2 v^3 k_B T^2} \int_0^{\omega_D} \frac{\omega^4 e^{\hbar\omega/k_B T}}{\left[e^{\hbar\omega/k_B T} - 1\right]^2} d\omega \tag{2.6}$$

where the coefficient 3 comes from the three polarizations of the crystal, and ω_D is cut-off frequency in the Debye model. At very high temperature, $T \gg \theta_D$, the specific heat approaches the classical value of $3Nk_B$. At very low temperature, the specific heat can be approximated by letting the upper limit go to infinity as follows

$$C \cong 234 N k_B \left(\frac{T}{\theta_D}\right)^3 \tag{2.7}$$

which is the Debye T^3 approximation. Similarly, for 2D and 1D structure, the specific heat is proportional to T^2 and T, respectively. Substituting the expression for the specific heat into Eq. 2.4 and introducing the concept of relaxation time, τ, which is average time between two collision events, the thermal conductivity can be expressed as

$$k = \frac{1}{2\pi^2 v} \frac{1}{k_B T^2} \int_0^{\omega_c} (\hbar\omega)^2 \omega^2 \frac{e^{\hbar\omega/k_B T}}{\left(e^{\hbar\omega/k_B T} - 1\right)^2} \tau(\omega) d\omega \tag{2.8}$$

where $\tau(\omega)$ is the frequency-dependent relaxation time, which is determined by different scattering mechanisms. Phonons can be scattered by defects or dislocations in the crystal, impurities such as dopants, boundaries, electrons, or by interaction with other phonons [3, 4]. The scattering mechanisms can be divided into two types. The first is elastic scattering between a phonon and a lattice imperfection where the

phonon frequency does not change. From the kinetic theory, the average time, τ_i, between collisions with imperfections can be expressed as [3]

$$\tau_i = \frac{1}{\alpha \sigma \rho v} \tag{2.9}$$

where σ is the scattering cross section, ρ is the number of scattering sites per unit volume of defect density, and α is a constant. The expression for σ was proposed by Majumdar as [5]

$$\sigma = \pi R^2 \left(\frac{\chi^4}{\chi^4 + 1} \right) \tag{2.10}$$

with a size parameter $\chi = 2\pi R / \lambda = \omega R / v$, where R is the radius of the lattice imperfection and λ is the phonon wavelength. The other type of scattering is inelastic scattering between phonons where the phonon frequency changes. Inelastic scattering arises from the inter-atomic potential energy not being purely harmonic, which changes the spring stiffness with deformation. As a result, the acoustic impedance of the incident lattice wave is changed, consequently giving rise to wave scattering. There are two types of three-phonon collision process: the normal (Figure 2.1a) and the Umklapp (Figure 2.1b) processes. In the normal process, the total energy and total momentum of the phonons are not changed ($\omega_1 + \omega_2 = \omega_3$, and $\boldsymbol{K}_1 + \boldsymbol{K}_2 = \boldsymbol{K}_3$). Consequently, the normal processes do not produce any resistance to heat flow. In the Umklapp process, the total energy is conserved but the magnitude of the sum $\boldsymbol{K}_1 + \boldsymbol{K}_2$ exceeds the maximum limit set by the edge of the first Brillouin zone. Since the only meaningful phonon momentums lie in the first Brillouin zone so that any longer $\boldsymbol{K}$ produced in a collision must be brought back into the first Brillouin zone. Hence the magnitude and direction of momentum of the third phonon is defined by adding the

reciprocal lattice vector, $\boldsymbol{G}$ with a magnitude of $2\pi/a$, where a is the lattice constant, as shown in Figure 2.1b:

$$\boldsymbol{K}_1 + \boldsymbol{K}_2 = \boldsymbol{K}_3 + \boldsymbol{G} \tag{2.11}$$

Such processes are always possible in a periodic lattice. During the Umklapp process the phonon momentum is not conserved, and therefore this process produces a resistance to heat flow. At high temperature, Umklapp scattering is the dominant scattering mechanism for lattice thermal conductivity.

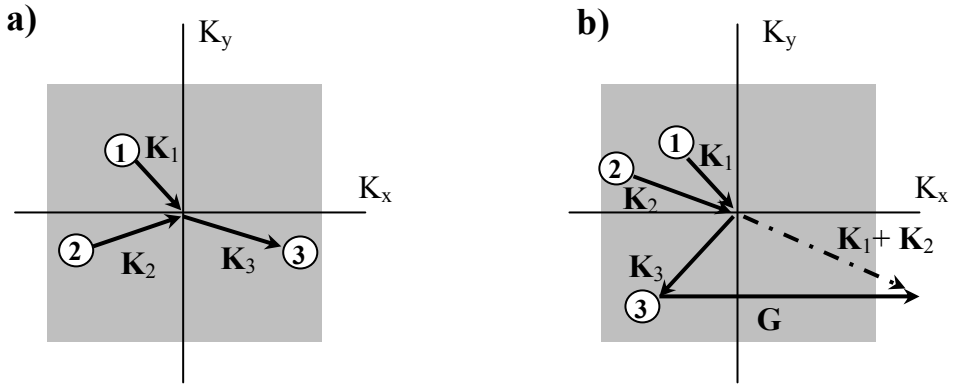

Figure 2.1: (a) Normal $\boldsymbol{K}_1 + \boldsymbol{K}_2 = \boldsymbol{K}_3$ and (b) Umklapp $\boldsymbol{K}_1 + \boldsymbol{K}_2 = \boldsymbol{K}_3 + \boldsymbol{G}$ phonon collision processes in a two-dimensional square lattice. The grey square in each figure represents the first Brillouin zone in the phonon $\boldsymbol{K}$ space [2].

The phonon lifetime in Eq. 2.8, τ, is commonly given by Matheissen's rule in which the total inverse lifetime is the sum of the inverse lifetimes corresponding to different scattering mechanisms including impurity, anharmonic, and boundary scattering. The total inverse lifetime can then be expressed as [6]

$$\frac{1}{\tau} = \frac{1}{\tau_i} + \frac{1}{\tau_{ph-ph}} + \frac{1}{\tau_b} \tag{2.12}$$

where,

- τ_i is the phonon lifetime corresponding to impurity scattering, including isotope scattering.

- $\tau_{ph\text{-}ph}$ is the phonon lifetime corresponding to phonon-phonon scattering, including the Umklapp (τ_U), and normal (τ_N) processes.

- τ_b is the phonon lifetime corresponding to boundary scattering.

Quite a number of modeling efforts have been carried out to predict the thermal conductivity of bulk crystals [1, 7]. The pioneering work in modeling lattice thermal conductivity was carried out by Callaway in 1959 [7]. In crystals with one atom in the primitive cell, the phonon dispersion relation contains longitudinal acoustic (LA) and transverse acoustic (TA) branches, each having different group velocities in different crystal directions. In Callaway's work, the Debye dispersion relation for a single effective acoustic branch was assumed to be the same for longitudinal and transverse phonons, and an average speed of sound was used in the calculation. In his approach, the following scattering processes were assumed:

(1) Boundary scattering, described by a constant relaxation time L/v, where v is the speed of sound and L is some length characteristic of the material;

(2) Normal three-phonon processes with a relaxation time $\tau_N^{-1} = B_2\omega^2T^3$, where ω is the circular frequency and T is the absolute temperature;

(3) Umklapp scattering with a relaxation time expressed as $\tau_U^{-1} = B_1^{'}e^{\theta_D/aT}\omega^2T^3 = B_1\omega^2T^3$, where θ_D is the Debye temperature and α is a constant characteristic of the phonon spectrum of the materials – for

germanium, on account of its extreme dispersion in the vibration spectrum, α may be of the order of 8 [8];

(4) Impurity scattering, including isotope scattering, with a relaxation time independent of temperature and was taken as $\tau_i^{-1} = A\omega^4$.

In the lattice thermal conductivity calculation, B_1 and B_2 are treated as adjustable parameters and represent the normal and Umklapp scattering effects. Callaway's model fits the experimental data well for germanium (Ge). For thermal conductivity of bulk crystalline silicon (Si), however, this model only fits the experimental data [9] at low temperature fairly well, but yields a much lower value at higher temperature.

Unsatisfied with the discrepancies between Callaway's results and the experimental data at high temperature, Holland [1] assumed that the three-phonon relaxation times strongly depend on the actual phonon branch and the dispersion relation in the phonon spectrum needs to be treated differently between longitudinal and transverse phonons in order to get a reasonable prediction across the entire temperature range. In Holland's approach, the longitudinal and transverse phonon branches were separated with a two-piecewise-linear dispersion relation for each branch. Another average speed of sound v_s was used for both the boundary scattering and impurity scattering. The expressions for relaxation time for different scattering mechanisms were:

(1) Boundary scattering, $\tau_b^{-1} = v / LF$, where a new parameter F is introduced to represent a correction due to both the smoothness of the surface and the finite length to thickness ratio of the sample;

(2) Impurity scattering, which is kept the same as Callaway's expression

$\tau_i^{-1} = A\omega^4$;

(3) Umklapp scattering, the relaxation time for longitudinal acoustic (LA) phonons is kept the same as that in Callaway's model, $\tau_U^{-1} = B_L \omega^2 T^3$. For transverse acoustic (TA) phonons, the Umklapp scattering is a piecewise function expressed as $\tau_U^{-1} = 0$ for $\omega < \omega_1$, and $\tau_U^{-1} = B_{TU}\omega^2 / \sinh(\hbar\omega / k_B T)$ for $\omega_1 < \omega < \omega_2$, where ω_1 is the frequency at which the Umklapp processes start and ω_2 is the highest transverse mode frequency.

(4) Normal scattering, for LA phonons, the relaxation time is assumed to have the same frequency and temperature dependence as the Callaway's model with the adjustable parameter B_L. For the TA phonons, the scattering rate is expressed as $\tau_{TN}^{-1} = B_T \omega T^4$.

With Holland's approach, modeling results on bulk Si are in good agreement with the experimental data up to 1000 K. Although Callaway's and Holland's models fit quite well with experimental results of bulk crystalline materials such as Ge and Si, their validity for thermal conductivity of one-dimensional nanostructures such as NWs or NTs is uncertain.

2.2. Thermal transport in one-dimensional nanostructures

The pioneering experiment studies on phonon transport in NWs were carried out by Tighe *et al.* [10]. The thermal conductance of GaAs beams was measured at very low temperature (<6 K) by a micro-device containing a thin, rectangular intrinsic GaAs thermal reservoir suspended above the substrate by four intrinsic GaAs beams

(200 nm × 300 nm). The isolated reservoir is Joule heated by a source transducer patterned above it. The reservoir cools through the long, narrow intrinsic GaAs bridges. Measurement of the reservoir temperature, arising in response to the heat input, is achieved using a second local sensing transducer. These transducers are made of highly doped GaAs with line-width of 100 nm and thickness of 150 nm. Using this device, they successfully measured the total thermal conductance of the four GaAs bridges and deduced the phonon mean-free path in GaAs.

In this vein, efforts to study thermal transport in NWs have shown the significant reduction of thermal conductivity compared with the bulk counterparts. The explanations include the variation in the phonon spectrum and related properties [11, 12], and the influence of boundary scattering [12, 13]. In NWs, phonons collide with the boundary more often than in bulk materials. Consequently, phonon boundary scattering poses much more resistance to phonon transport than in bulk materials. When the NW diameter is comparable to phonon wavelength, the phonon dispersion relation can also be changed due to boundary confinement. This change leads to smaller phonon group velocities, consequently reducing further the thermal transport. The studies showed that the lattice thermal conductivity of a 20 nm diameter Si NW is predicted to be less than 10% of the bulk Si value [12].

Beside the effects of boundary scattering and changing phonon dispersion relation, quantum thermal conductance effects were also observed in particular NW systems [14 – 16]. Rego *et al.* [15] predicted that a dielectric NW would exhibit quantized thermal conductance at low temperatures in a ballistic transport regime. The phonon energy spectrum for all objects is actually discrete so that the allowed wave-vectors can only occur at integer multiples of π/L, where L is the characteristic length

of the object in the given direction. If L is large enough, the finite spacing becomes small, and the spectrum may be treated as continuous. However, in a NW, the continuous dispersion relation may no longer be a valid approximation for the discrete spectrum in the transverse direction. When the phonons travel through the NW from the hot end to the cold end, the effects of the quantized thermal states restricts transport at specific frequencies: the phonon with the longest wavelength that just fits within the wire dimensions is allowed, while other longer wavelengths are not permitted. This phenomenon results in ballistic transport, and consequently, quantized thermal conductance. The first observation of a quantized limiting value of thermal conductance in nitride beams at very low temperature (< 6 K) was reported by Schwab *et al.* [16]. The device was a modified version of the micro-device in Ref [10] where silicon nitride films were used instead of GaAs, with Cr/Au resistors serving as the heater and thermometer. The shape of the beam was also modified to ensure ideal coupling between the phonon mode and thermal reservoirs. The experimental results showed that at extremely low temperature, thermal conductance by ballistic phonon transport through the 1D channel approaches a maximum value of $G_0 = \pi^2 k_B^2 T / 3h$, the universal quantum of thermal conductance. Because of the limitation in scaling the beam samples down to tens of nanometers, this method has only been used to mainly study the quantum transport of phonons in the lowest energy modes in nanostructures at ultra low temperature. No further attempt has been carried out to measure the thermal conductance in a higher temperature range up to room temperature using this method.

In contrast to NWs, boundary scattering is nearly absent in carbon nanotubes (CNTs) due to their unique crystalline structure, which leads to super high electrical and thermal conductivity [17 – 19]. Mingo *et al.* [20] have also demonstrated ballistic

thermal conductance in CNTs. At low temperature, CNTs exhibit linear temperature dependence of thermal conductance with a maximum possible value $G = 4\pi^2 k_B^2 T / 3h$, corresponding to four quanta of thermal conductance. In their work, Mingo *et al.* also claimed that the sample lengths in which phonon transport remains ballistic are considerably long (~ 1.5 μm). Experimentally, Chang *et al.* [21] have shown the breakdown of Fourier's empirical law of thermal conduction in individual multiwalled carbon and boron-nitride NTs. In their work, individual multiwall tubes were placed on a custom-designed microscale thermal conductivity test device consisting suspended SiN_x pads with integrated Pt film resistors serving as either heaters or sensors. This kind of microscale device have been initially designed, fabricated, and employed for thermal conductance measurement of 1-D nanostructures by Shi *et al.* [22]. The thermal conductance of a NT was determined by supplying power to the heater and measuring the resulting temperature changes of the heater and sensor pads. For length-dependent thermal conductance investigations, after each measurement they deposited an additional thermal contact pad between the original pads and then measured the thermal conductance of shortened suspended NTs again. The results showed that Fourier's law is violated in NT samples regardless of whether the sample length is much longer than the phonon mean free-path.

Among NWs, silicon nanowire (SiNW) has probably attracted the most attention since silicon is foundation of modern electronics. Alongside experimental studies, theoretical and numerical investigations of phonon transport in SiNWs have been carried out. A molecular dynamics (MD) study predicted that for SiNWs with square cross sections of 1.61 nm × 1.61 nm, 2.14 nm × 2.14 nm, 2.68 nm × 2.68 nm, and 5.35 nm × 5.35 nm, thermal conductivities could be two orders of magnitude smaller than those of bulk Si crystals in a temperature range (200 – 500K) [13].

Boltzmann transport equation (BTE) was also solved with different specularity parameters for boundary scattering and it is found that with a specularity value of 0.45, the MD results matched BTE solutions reasonably well. Khitun *et al.* [11] calculated the phonon dispersion change for a 20 nm diameter SiNW and found that the overall value of the average phonon group velocity is only about half of the bulk phonon group velocity. The thermal conductivity of this 20 nm diameter SiNW was then calculated following Callaway's approach [7]. The predicted thermal conductivity from 300 K to 700 K is more than one order of magnitude smaller than the corresponding bulk value. Later on, the thermal conductivity of a 10nm diameter SiNW was calculated by Volz *et al.* [23] based on phonon transport equation. In this work, the boundary specularity characteristics were considered and different scattering mechanisms were also discussed. A Monte Carlo simulation on SiNW thermal conductivity based on the bulk dispersion and NW dispersion has been carried out by Chen *et al.* [24]. The Monte Carlo results also suggest that the dispersion relation change will lead to a significant reduction in thermal conductivity.

In 2003, Li *et al.* [25] reported a systematic experimental study of the size effect on the SiNW thermal conductivity. The thermal conductivity of individual single crystalline intrinsic SiNWs, which were synthesized by the vapor – liquid – solid (VLS) method [26], with diameters of 22, 37, 56, and 115 nm were measured using a microfabricated suspended device [22] over a temperature range of 20 – 320 K. The observed thermal conductivity was more than two orders of magnitude lower than the bulk value. Their experimental results are shown in Figure 2.2a and the temperature dependence of the thermal conductivity between 20 and 60 K is shown in Figure 2.2b.

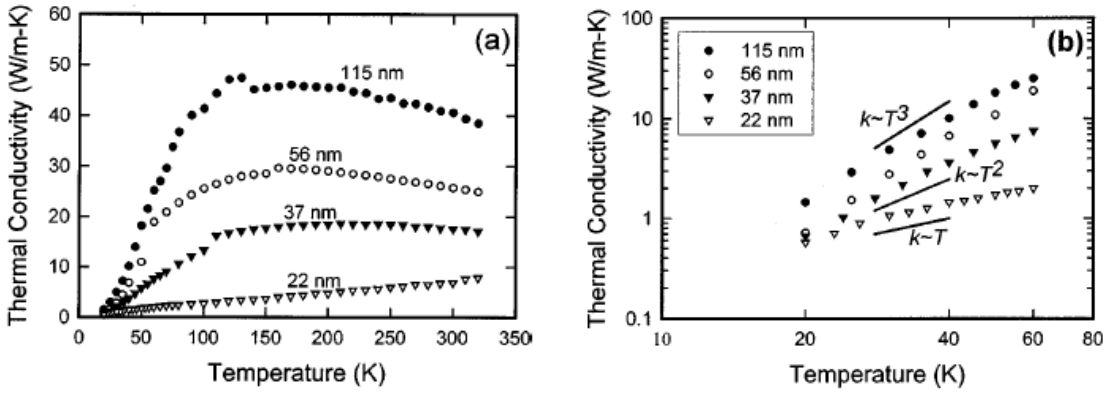

Figure 2.2: (a) Measured thermal conductivity of different diameter SiNWs. The number beside each curve denotes the corresponding wire diameter. (b) Low temperature experimental data on a logarithmic scale [25].

The strong diameter dependence of the thermal conductivity clearly indicates that enhanced boundary scattering has a strong effect on phonon transport in SiNWs. From the double-log plot, it can be seen that the 115 and 56 nm diameter NWs fit the Debye T^3 law quite well in the low temperature range. It was suggested that boundary scattering, which is frequency and temperature independent, is the dominant phonon scattering mechanism. Hence, the thermal conductivity follows the temperature dependence of specific heat. Interestingly, for the smallest diameter wire (22 nm) the deviation from Debye law can be clearly seen. This result reveals that besides phonon boundary scattering, some other effects, such as the change in phonon dispersion relation due to confinement, could play important roles. Following this work, theoretical and numerical efforts were made to understand and fit these experimental data [27, 28]. Mingo *et al.* [27] theoretically predicted the temperature dependent thermal conductivity of Si and Ge NWs, in which they used their "real dispersions" approach. The thermal conductivity calculations using Callaway's [7] and Holland's [1] approaches were also carried out for Si NWs. Their approach is actually a simple modification to Callaway's model. Calculations showed that Callaway's model

predicts an Umklapp scattering rate that is more than one order of magnitude higher than the Umklapp scattering rate for the TA phonons predicted by the Holland's model. The model proposed by Mingo *et al.* yields an Umklapp scattering rate that is in between that of the Callaway's and Holland's predictions. Besides the Umklapp scattering rate, their model assumes a single acoustic branch following Callaway. They took the cut-off frequency, ω_c, as an adjustable parameter instead of fixing it at the Debye frequency. They argued that the selection of the cut-off frequency is not very important for bulk Si thermal conductivity calculation. However, in NWs, for which the frequency-independent boundary scattering is dominant, the cut-off frequency is a crucial parameter and has to be adjusted. Their results showed that, while the calculated thermal conductivity of Si NWs using Callaway's and Holland's models showed large disagreements with experiment data, their real dispersions approach yields good agreement with experiments for Si NWs between 37 and 115 nm. Figure 2.3 shows theoretical predictions of thermal conductivities of Si NWs using (a) Callaway's model, (b) Holland's model, and (c) their real dispersions approach, compared with Li *et al.*'s experimental data [25].

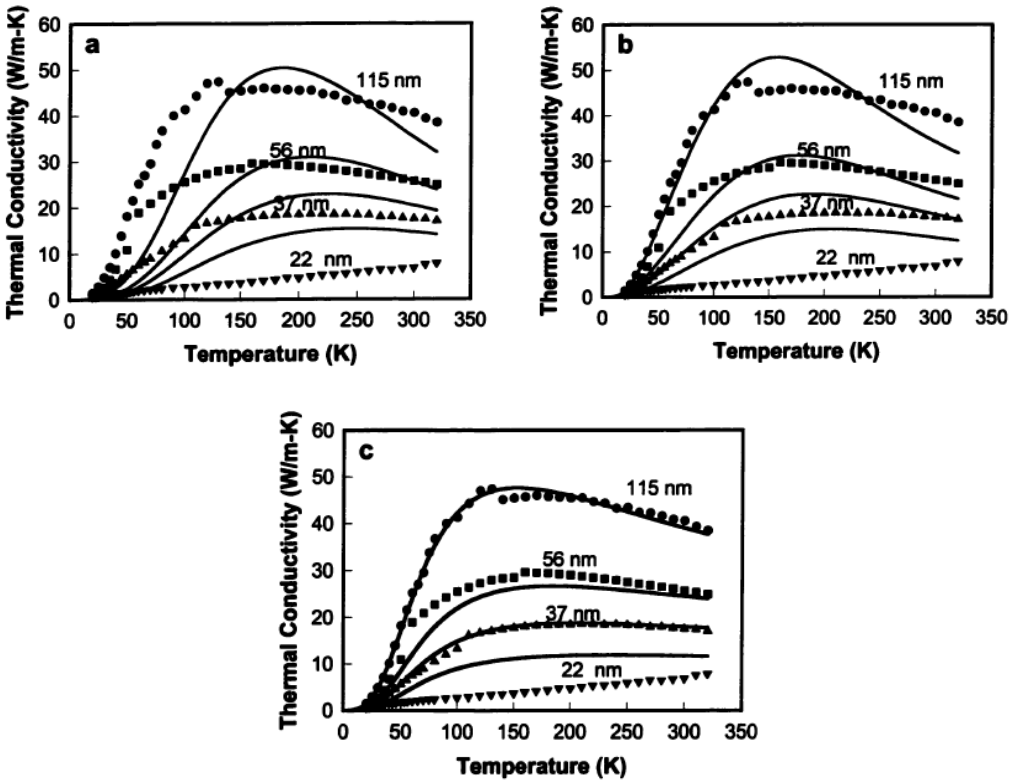

Figure 2.3: Theoretical predictions of thermal conductivities of Si NWs by (a) Callaway's model, (b) Holland's model, and (c) Mingo *et al.*'s model [27].

It can be seen that the results from Callaway's model do not follow the temperature dependence and the difference between the model prediction and the experimental results is quite large. On the other hand, Holland's model presents better results than Callaway's model and the temperature dependence shows a more similar trend. In contrast with Callaway's and Holland' model, the real dispersions model fit the experimental data reasonable well for the 37, 56, and 115 nm diameter NWs. The temperature dependence of the thermal conductivity also fit the experimental results. A further effort by Mingo [28] calculated the thermal conductivity of crystalline Si NWs using complete phonon dispersions, which does not require any externally imposed cut-off frequency. The results showed even better agreement with experimental results for NWs wider than 35 nm (Figure 2.4).

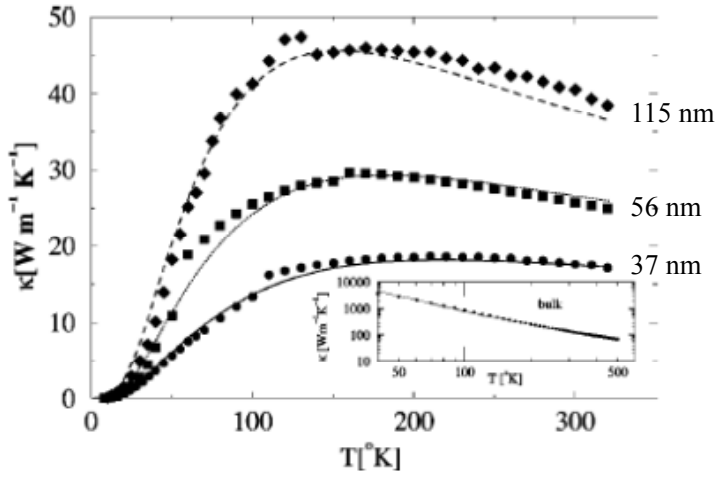

Figure 2.4: Thermal conductivity versus temperature calculated using the complete dispersions transmission function for 37, 56, and 115 nm diameter Si NWs [28].

However, these theoretical calculations are only expected to apply to Si NWs wider than ~ 35 nm for which phonon confinement effects are not important and a diffusive boundary scattering is assumed. Similar conclusions were also drawn from measurements on tin dioxide (SnO_2) nanobelts [29] and bismuth telluride (Bi_xTe_{1-x}) NWs [30]. Exceptionally, it can be seen that the predicted conductivity for the 22 nm diameter NW are about twice the experimental data value. Several other attempts were made [31, 32] to explain the low thermal conductivity as well as the unusual linear behavior of temperature dependent thermal conductivity in the low temperature range. However, the modeling results did not quantitatively agree with the experimental data.

In order to understand the underlying physics of the thermal transport properties of thin Si NWs, Chen *et al.* [33] systematically examine the phonon transport in thin Si NWs with diameters less than 30 nm both experimentally and theoretically. They observed that the thermal conductance of thin Si NWs initially

increases with temperature from 20 K to around 200 K, and then becomes flat or decreases at high temperature (Figure 2.5a). More interestingly, as shown in the double-log plot at low temperature (Figure 2.5b), the thermal conductance was observed to vary approximately linearly with temperature for all thin NW samples, which is consistent with results for the 22 nm Si NW in Ref. [25].

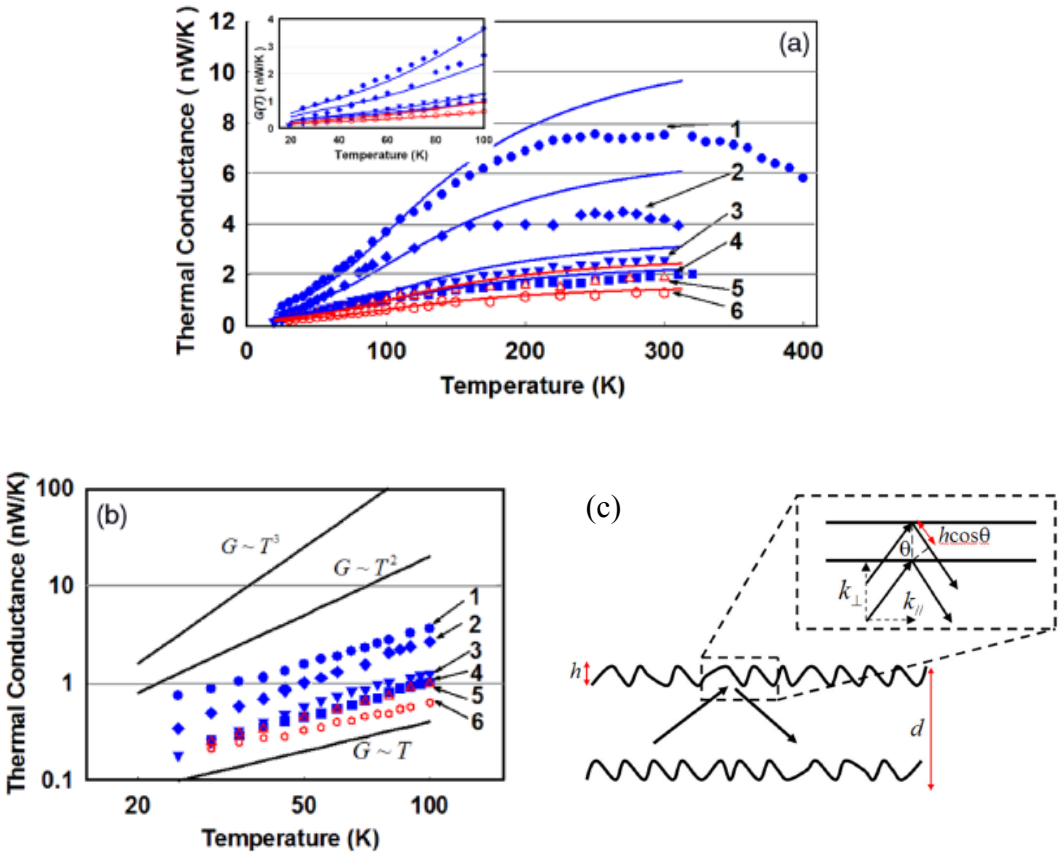

Figure 2.5: (a) Thermal conductance versus temperature ($G(T)$) of thin Si NWs. The number beside each curve denotes the sample with different synthesis methods (diameter-reduced method: #1 to #4; and as-grown Pt-catalyzed method: #5, #6), and different diameter (the diameter of #1, #2, #3, and #4 increases gradually from the tip to the base of NW with the value of 31 – 50, 26 – 34, 20 – 29, and 24 – 30 nm, respectively; and the diameter of #5, #6 is relatively uniform with the value of 17.9 ± 3.1 nm). The solid lines are the corresponding modeling results. (b) The $G(T)$ in log – log scale from 20 K to 100 K. (c) Schematic diagram of the NW boundary scattering used in Chen *et al.*'s model [33].

They also had developed a theoretical model which is based on the Landauer expression of the thermal conductance of a cylinder with boundary scattering in terms of the transmission probabilities of different modes of the cylinder. The results from their proposed model fit well to the thermal conductance experimental data in the low temperature range (20 – 100K) (referring to solid lines in Figure 2.5a). Figure 2.5c shows the schematic diagram of the NW boundary used in their model. The component of the wave vector of a phonon mode perpendicular to the NW axis is $k_{\perp} = k\cos\theta$. For $hk_{\perp} \ll 1$, the phonon should scatter specularly from the boundary and the mean free path depends on the frequency as follows:

$$l^{-1} = B\left(\frac{h}{d}\right)^2 \frac{1}{d}\left(\frac{\omega}{\omega_D}\right)^2 N(\omega) \tag{2.13}$$

where d is the diameter of the NW, ω is the frequency of the phonon mode, ω_D is the Debye frequency, and $N(\omega)$ is the number of modes with frequency ω. For the modes with $hk_{\perp} > 1$, where diffusive transport is applicable, the mean free path is assigned the value d, the diameter of the NW. The number of modes at a given frequency is given by

$$N(\omega) = 4 + A\left(\frac{d}{a}\right)^2\left(\frac{\omega}{\omega_D}\right)^2 \tag{2.14}$$

where a is the lattice spacing, and the number "4" arises because of four modes: one longitudinal, one torsional, and two flexural modes. The total number of modes include the number of modes with mean free path l, $N_1(\omega)$, and the number of modes with mean free path d, $N_2(\omega)$. The thermal conductance is finally given by the Landauer formula [34]:

$$G = \frac{1}{2\pi\hbar}\int\left(\frac{N_1(\omega)}{1+L/l(\omega)}+\frac{N_2(\omega)}{1+L/d}\right)\frac{\hbar^3\omega^2}{k_B T^2}\frac{e^{\hbar\omega/k_B T}}{(e^{\hbar\omega/k_B T}-1)^2}d\omega \qquad (2.15)$$

where L is the length of the NW. The theoretical prediction from this model, however, consistently over-estimates the experimental results of thermal conductance of Si NWs. The reason is that Umklapp scattering was not included in their theoretical model.

Although lot of works have been carried out on thermal transport in 1-D nanostructures, the theoretical and numerical investigations still cannot fully explain anomalous phenomena in the experimental data. In this thesis, we wish to systematically study the thermal transport properties in various NWs, including zinc oxide (ZnO), vanadium dioxide (VO_2), and Si NWs, in order to elucidate the nature of thermal transport in these materials, and to explore potential applications.

References

1. Holland, M. G.; “Analysis of Lattice Thermal Conductivity”, Phys. Rev. Vol. 132, pp. 2461 – 2471, 1963.

2. Kittel, C.; *Introduction to Solid State Physics*. New York: John Wiley & Sons, 1996.

3. Tien, C. L.; Majumdar, A.; and Gerner, F. M.; *Microscale Energy Transport*. Washington, D. C.: Taylor & Francis, 1998.

4. Ziman, J.; *Electrons and Phonons*. Oxford: Oxford University Press, 2001.

5. Majumdar, A.; “Microscale Heat Conduction in Dielectric Thin Films”, *J. Heat Trans.* Vol. 115, pp. 7 – 16, 1993.

6. Asen-Palmer, M.; Bartkowski, K.; Gmelin, E.; Cardona, M.; Zhernov, A. P.; Inyushkin, A. V.; Taldenkov, A.; Ozhogin, V. I.; Itoh, K. M.; and Haller, E. E.; “Thermal Conductivity of Germanium Crystals with Different Isotopic Compositions”, *Phys. Rev. B* Vol. 56, pp. 9431 – 9446, 1997.

7. Calaway, J.; “Model for Lattice Thermal Conductivity at Low Temperature”, *Phys. Rev.* Vol. 113, pp. 1046 – 1051, 1959.

8. Brockhouse, B. N.; and Iyengar, P. K.; “Normal Vibrations of Germanium by Neutron Spectrometry”, *Phys. Rev.* Vol. 108, pp. 894 – 895, 1957.

9. Touloukian, Y. S.; *Thermophysical properties of matter*. New York: IFI/Plenum, Vol. 2, 1970.

10. Tighe, T. S.; Worlock, J. M.; and Roukes, M. L.; “Direct Thermal Conductance Measurements on Suspended Monocrystalline Nanostructures”, *Appl. Phys. Lett.* Vol. 70, pp. 2687 – 2689, 1997.

11. Khitun, A.; Balandin, A.; and Wang, K. L.; “Modification of the Lattice Thermal Conductivity in Silicon Quantum Wires due to Spatial Confinement of Acoustic Phonons”, *Superlatt. Microstruct.* Vol. 26, pp. 181 – 193, 1999.

12. Zou, J.; and Balandin, A.; “Phonon Heat Conduction in a Semiconductor Nanowires”, *J. Appl. Phys.* Vol. 89, pp. 2932 – 2938, 2001.

13. Volz, S. G.; and Chen, G.; “Molecular Dynamics Simulation of Thermal Conductivity of Silicon Nanowires”, *Appl. Phys. Lett.* Vol. 8, pp. 389 – 408, 1999.

14. Angelescu, D. E.; Cross, M. C.; and Roukes, M. L.; “Heat Transport in Mesoscopic Systems”, *Superlatt. Microstruct.* Vol. 23, pp. 673 – 689, 1998.

15. Rego, L. G. C.; and Kirczenow, G.; “Quantized Thermal Conductance of Dielectric Quantum Wires”, *Phys. Rev. Lett.* Vol. 81, pp. 232 – 235, 1998.

16. Schwab, K.; Henriksen, E. A.; Worlock, J. M.; and Roukes, M. L.; "Measurement of the Quantum of Thermal Conductance", *Nature* Vol. 404, pp. 974 – 977, 2000.

17. Yu, C. H.; Shi, L.; Yao, Z,; Li, D.; and Majumdar, A.; "Thermal Conductance and Thermopower of an Individual Single-Wall Carbon Nanotube", *Nano Lett.* Vol. 5 (9), pp. 1842 – 1846, 2005.

18. Fujii, M.; Zhang, X.; Xie, H. Q.; Ago, H.; Takahashi, K.; Ikuta, T.; Abe, H.; and Shimizu, T.; "Measuring the Thermal Conductivity of a Single Carbon Nanotube", *Phys. Rev. Lett.* Vol. 95, 065502, 2005.

19. Prasher, R. S.; Hu, X. J.; Chalopin, Y.; Mingo, N.; Lofgreen, K.; Volz, S.; Cleri, F.; and Keblinski, P.; "Turning Carbon Nanotubes from Exceptional Heat Conductors into Insulators", *Phys. Rev. Lett.* Vol. 102, 105901, 2009.

20. Mingo, N.; and Broido, D. A.; "Carbon Nanotube Ballistic Thermal Conductance and Its Limits", *Phys. Rev. Lett.* Vol. 95, 096105, 2005.

21. Chang, C. W.; Okawa, D.; Garcia, H.; Majumdar, A.; and Zettl, A.; "Breakdown of Fourier's Law in Nanotube Thermal Conductors", *Phys. Rev. Lett.* Vol. 101, 075903, 2008.

22. Shi, L., Li, D., Yu, C., Jang, W., Kim, D., Yao, Z., Kim, P., Majumdar, A., "Measuring Thermal and Thermoelectric Properties of One-Dimensional Nanostructures Using a Microfabricated Device", *J. Heat Trans.* Vol. 125, pp. 881 – 888, 2003.

23. Volz, S.; Lemonnier, D.; and Saulnier, J.; "Clamped Nanowire Thermal Conductivity Based on Phonon Transport Equation", *Microscale Thermophys. Eng.* Vol. 5, pp. 191 – 207, 2001.

24. Chen, Y.; Li, D.; Lukes, J. R.; and Majumdar, A.; "Monte Carlo Simulation of Silicon Nanowire Thermal Conductivity", *J. Heat Trans.* Vol. 127, pp. 1129 – 1137, 2005.

25. Li, D.; Wu, Y.; Kim, P.; Shi, L.; Yang, P.; and Majumdar, A.; "Thermal Conductivity of Individual Silicon Nanowires", *Appl. Phys. Lett.* Vol. 83, pp. 2934 – 2936, 2003.

26. Wu, Y.; Yan, H.; Huang, M.; Messer, B.; Song, J. H.; and Yang, P.; "Inorganic Semiconductor Nanowires: Rational Growth, Assemblies and Novel Properties", *Chem. Eur. J.* Vol. 8, pp. 1260 – 1268, 2002.

27. Mingo, N.; Yang, L.; Li, D.; and Majumdar, A.; "Predicting the Thermal Conductivity of Si and Ge Nanowires", *Nano Lett.* Vol. 3, pp. 1713 – 1716, 2003.

28. Mingo, N.; "Calculation of Si Nanowire Thermal Conductivity Using Complete Phonon Dispersion Relations", *Phys. Rev. B* Vol. 68, 113308, 2003.

29. Shi, L.; Hao, Q.; Yu, C. H.; Mingo, N.; Kong, X. Y.; and Wang, Z. L.; "Thermal Conductivities of Individual Tin Dioxide Nanobelts", *Appl. Phys. Lett.* Vol. 84, pp. 2638 – 2640, 2004.

30. Zhou, J.; Jin, C.; Seol, J. H.; Li, X. G.; and Shi, L.; “Thermoelectric Properties of Individual Electrodeposited Bismuth Telluride Nanowires”, *Appl. Phys. Lett.* Vol. 87, 133109, 2005.

31. Moore, A. L.; Saha, S. K.; Prasher, R. S.; and Shi, L.; “Phonon Backscattering and Thermal Conductivity Suppression in Sawtooth Nanowires”, *Appl. Phys. Lett.* Vol. 93, 083112, 2008.

32. Zhukov, A. V.; Yang, S.; and Cao, J.; “Low-Temperature Thermal Transport in Nanowires”, *Jetp Lett.* Vol. 81, pp. 190 – 194, 2005.

33. Chen, R.; Hochbaum, A. I.; Murphy, P.; Moore, J.; Yang, P.; and Majumdar, A.; “Thermal Conductance of Thin Silicon Nanowires”, *Phys. Rev. Lett.* Vol. 101, 105501, 2008.

34. Murphy, P. G.; and Moore, J. E.; “Coherent Phonon Scattering Effects on Thermal Transport in Thin Semiconductor Nanowires”, *Phys. Rev. B* Vol. 76, 155313, 2007.

Chapter 3: Micro-Electro-Thermal System (METS) Device Fabrication and Experimental Setup

3.1. Introduction

There are several possible ways to measure thermal conductivity, each of them suitable for a limited range of materials, depending on the thermal properties and the medium temperature. Most thermal conductivity measurement techniques for bulk materials are based on creating a temperature gradient along the sample and monitoring the temperature by thermocouples situated at different locations. In 1961, Drabble and Goldsmid [1] measured the thermal conductivity of bulk materials using this technique. By measuring either total dc power or total ac power applied at one end, the thermal conductivity can be determined. Another way is to place the sample between standard materials with known thermal conductivities so that by comparing the temperature gradient, the sample thermal conductivity can be derived. Various techniques developed to measure thin-film thermal conductivities have been reviewed by Mirmira and Fletcher [2]. To measure thin-film thermal conductivity, a temperature gradient is created within the thin film by either Joule heating of a thin metal line or laser heating, and the corresponding temperature changes at different locations are measured by resistance thermometers. Recently, Cahill [3] used the time-domain thermo-reflectance method to analyze heat flow in layered structures of thin films. The idea behind this technique is that once a thin film is heated up, the change in the reflectance of the surface can be utilized to derive the thermal properties. The reflectivity is measured with respect to time, and the data received can be matched to a model which contains coefficients that correspond to the thermal properties (thermal

conductivity of thin films as well as thermal conductance of their interfaces).

These conventional techniques for bulk or thin film thermal property measurement cannot be readily used for individual nanotubes, nanowires (NWs) or nanobelts due to the small sample size. One of the most widely used techniques to measure thermal capacity and thermal conductivity of one-dimensional structures is the 3-ω method [4], which was first used by Cahill [5] to measure thermal conductivity of bulk and film materials. In this method, the specimen itself serves as a heater and at the same time a temperature sensor if it is electrically conductive with a temperature-dependent electric resistance. Otherwise, a metal strip is artificially deposited on its surface to serve both as heater and sensor. A sinusoidal ac electric current $I_0 \sin \omega t$ is passed through the specimen or the metal strip to create a temperature fluctuation along it at a frequency of 2ω, and accordingly a resistance fluctuation at 2ω. This further leads to a voltage fluctuation at 3ω across the sample. By solving the 1-D heat conduction equation, the 3ω signal of the voltage across the sample can be expressed in the form:

$$V_{3\omega} \approx \frac{4I^3 LRR'}{\pi^4 \kappa S \sqrt{1+(2\omega\gamma)^2}} \tag{3.1}$$

where κ, R, R', γ, L, and S are the thermal conductivity, electric resistance, differential temperature coefficient of resistance ($R' = dR/dT$), thermal time constant, length, and cross section of the sample, respectively. This 3ω signal can be extracted using digital lock-in amplifiers. When the specimen is extremely thin and long (NWs), the measurement has to be performed at the low frequency limit $\omega\gamma \rightarrow 0$. In this case, $V_{3\omega}$ is nearly frequency independent:

$$V_{3\omega} \approx \frac{4I^3 LRR'}{\pi^4 \kappa S} \tag{3.2}$$

By fitting the experimental data to this formula, the thermal conductivity κ of the sample can be obtained. One disadvantage of this method is the requirement of conductive samples, and is thus not suitable for un-doped semiconductor or non-conductive NWs.

In 2003, Shi *et al*. [6] developed a method to measure the thermal and thermoelectric properties of one-dimensional nanostructures using a microfabricated device. Their device (Fig. 3.1) is a suspended structure consisting of two adjacent 14 μm × 25 μm low stress silicon nitride (SiN_x) islands suspended with five 0.5 μm thick, 420 μm long and 2 μm wide silicon nitride beams. One 30nm thick and 300 nm wide platinum resistance thermometer (PRT) coil is designed on each island. The PRT is connected to 500 μm × 500 μm Pt bonding pads on the substrate via 1.2 μm wide Pt leads on the long SiN_x beams. An addition 1.2 μm wide Pt electrode is designed on each island facing each other, providing electrical contact to the sample. In their device, the etched pit in the Si substrate is usually about 100 – 200 μm deep, and hence the suspended structure does not adhere to the substrate following wet processes to release the MEMS structure. Nanowires, nanotubes or nanobelts are placed onto the microdevice between two electrodes by either using a nano-manipulator or a drop-cast method.

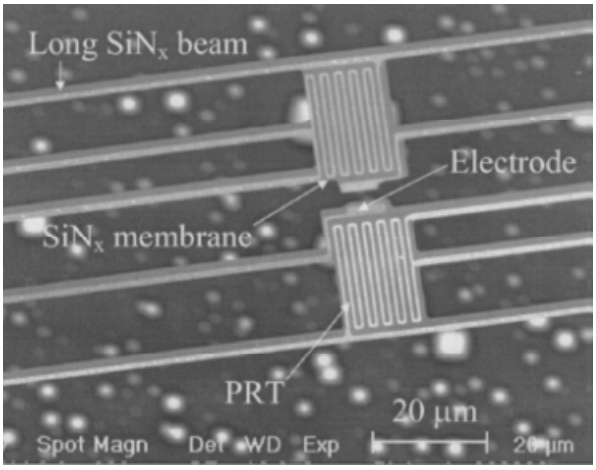

Figure 3.1: SEM image of a microdevice for thermal property measurements of nanostructures (Shi *et al*. [6]).

Some disadvantages of Shi's micro-fabricated device are as follows. Firstly the device has only two electrodes to provide contact points for electrical measurement of the NWs, hence the electrical resistance of the contacts need to be taken into consideration, which is not easily determined. Secondly the investigation of microstructure of samples using transmission electron microscopy (TEM) must be performed separately. Recently, Hippalgaonkar *et al*. [7] had developed micro-devices with backside opened which allowed them to investigate sample in TEM. However, the Si NWs studied in their work were top-down etched and integrated into the devices. This work made improvements to the design of the suspended micro electro-thermal system (METS) by providing four electrodes for four-point electrical measurements, and a through hole under the suspended islands.

In this chapter, we describe the design and fabrication process of METS devices consisting of suspended micro-heaters and thermometers. This is followed by a description of the measurement setup and measurement schemes. We also present a new technique using electron beam probing along a NW to provide a spatially-

resolved measurement of its thermal resistance. This technique also allows us to measure the thermal resistance of the contacts between the nanostructure and the underlying platinum electrodes.

3.2. Suspended micro-electro-thermal system (METS) fabrication

Figure 3.2 shows a schematic and a scanning electron micrograph of the METS device. The device is a suspended structure consisting of two adjacent 16 μm × 27 μm low stress silicon nitride (SiN_x) islands suspended by six 300nm thick, 400μm long and 2 μm wide silicon nitride beams. Each island comprises a platinum (Pt) loop (with metal line width of 300 nm and pitch of 300 nm) as a resistance thermometer connected to 0.8 mm × 1.0 mm Au bond pads (1 μm thick) via 30 nm or 60 nm thick, 1.8 μm wide Pt metal strips on top of nitride beams. Two 1.8 μm wide Pt electrodes are designed on each island to provide electrical contact to ends of the sample. The long and thin nitride beams are critical for thermal isolation from the bulk substrate.

Figure 3.3 shows the layout and actual dimensions of a METS device[1]. Each die is 7.4 mm long, 5.2 mm wide and 0.725 mm thick, and was diced from a completed wafer. The main island was designed to be suspended above a through hole to allow observation of the sample in a transmission electron microscope (TEM). Twelve 1 μm thick Au pads are placed at the periphery of the die which can be used for external wire bonding or as probing points. There are several additional suspended islands with smaller Au bonding pads designed over the METS device which can be used as test structures.

[1] The process flow and devices were designed in collaboration with the Institute of Microelectronics (IME), Singapore, and fabricated by IME.

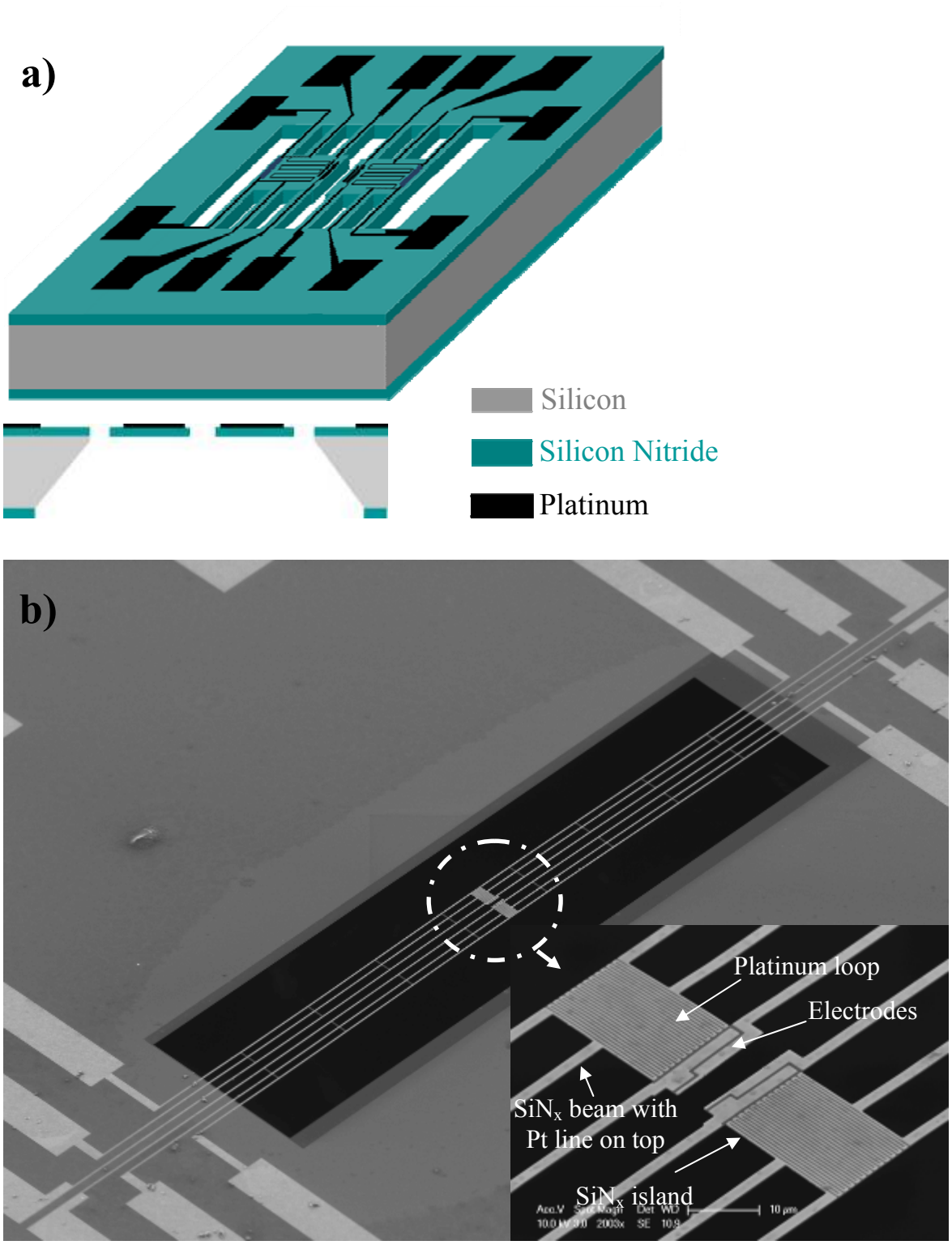

Figure 3.2: a) Schematic of suspended micro-electro-thermal system (METS) device and b) a scanning electron micrograph (SEM) of METS device.

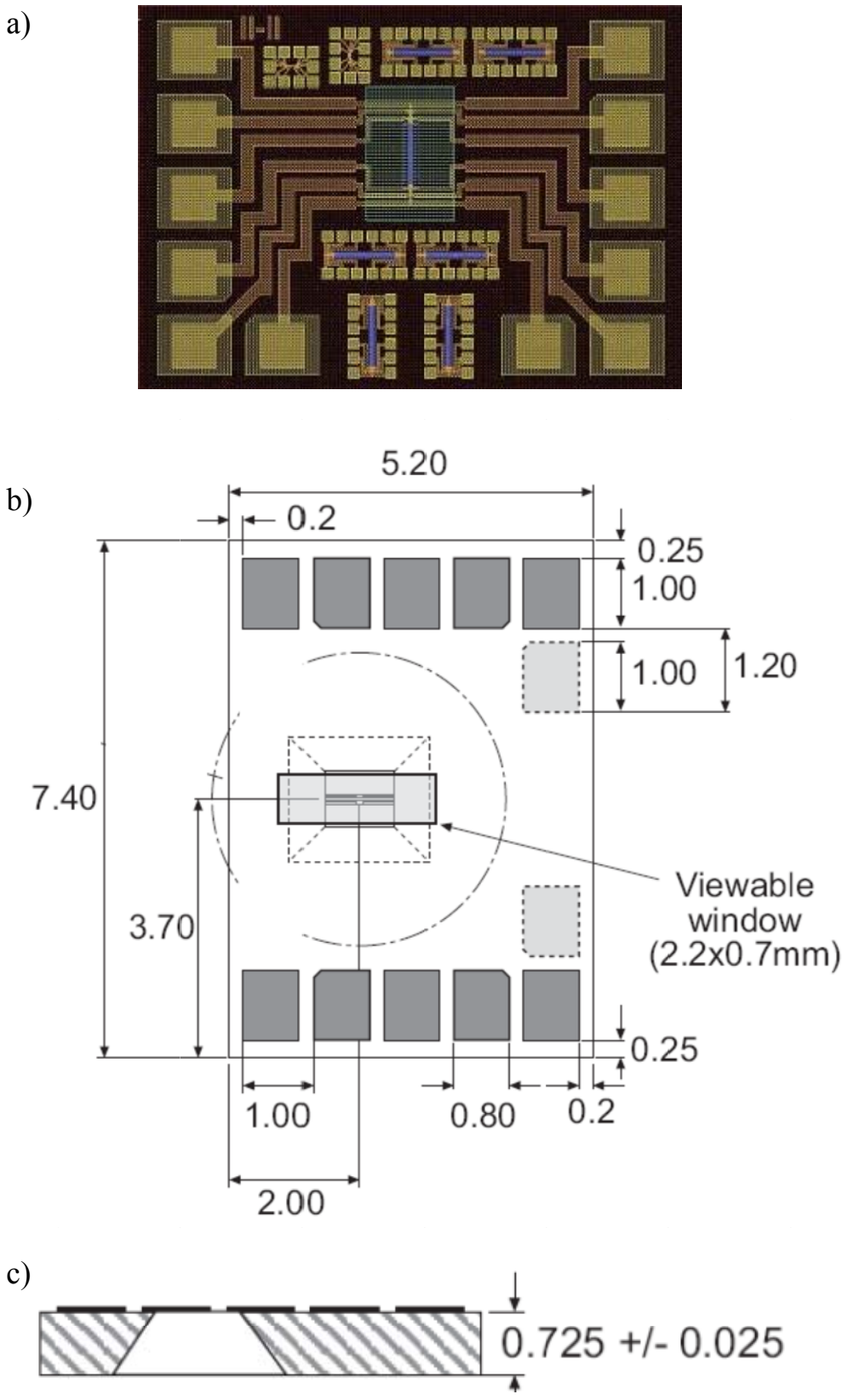

Figure 3.3: a) Actual design of METS device; b) and c) dimensions and thickness of METS device.

The 300 nm thick low-stress (50-100 MPa, tensile) nitride films were deposited on both sides of an 8-inch (100) Si wafers (725 μm thick) and were used as the starting substrates for batch fabrication of METS devices using fabrication process shown in Figure 3.4. The wafer was first cleaned using deionized (DI) water with quick dump rinse (QDR) and spin drying process (Figure 3.4a). 0.55 μm thick deep ultraviolet (DUV) positive photoresist was spun on the front-side surface and patterned using DUV lithography (248 nm) process with an optical mask (Figure 3.4b). The photoresist pattern was then transferred to the nitride film using reactive ion etching (RIE) (CH_2F_2 plasma) and the photoresist removed (Figure 3.4c). After cleaning, another 0.55 μm thick positive photoresist was coated and exposed using a high-resolution mask with very good alignment in the stepper, such that the Pt metal pattern evaporated later on could be registered accurately to the underlying nitride island pattern. 30 nm or 60 nm thick Pt on 5 nm or 10 nm thick Cr (as an adhesion layer), respectively, was then evaporated followed by an ultrasonic lift-off. Pt coils (PTC) on the islands and Pt leads connecting the coils to the bond pads are well aligned on nitride islands with misalignment of less than 0.1 μm (Figure 3.4d). The high resolution mask (with resolution of 300nm) is used to define the Pt coils with 300nm width and 300nm pitch. Each coil has a resistance of around 19 kΩ or 6 kΩ corresponding to 30 nm and 60nm thick Pt layers. 7 μm negative photoresist was then coated on the metalized wafer followed by patterning. Photolithography and Au metallization steps were then employed. Figure 3.4e shows the wafer with 1 μm thick Au bond pads created by evaporation and lift-off processes.

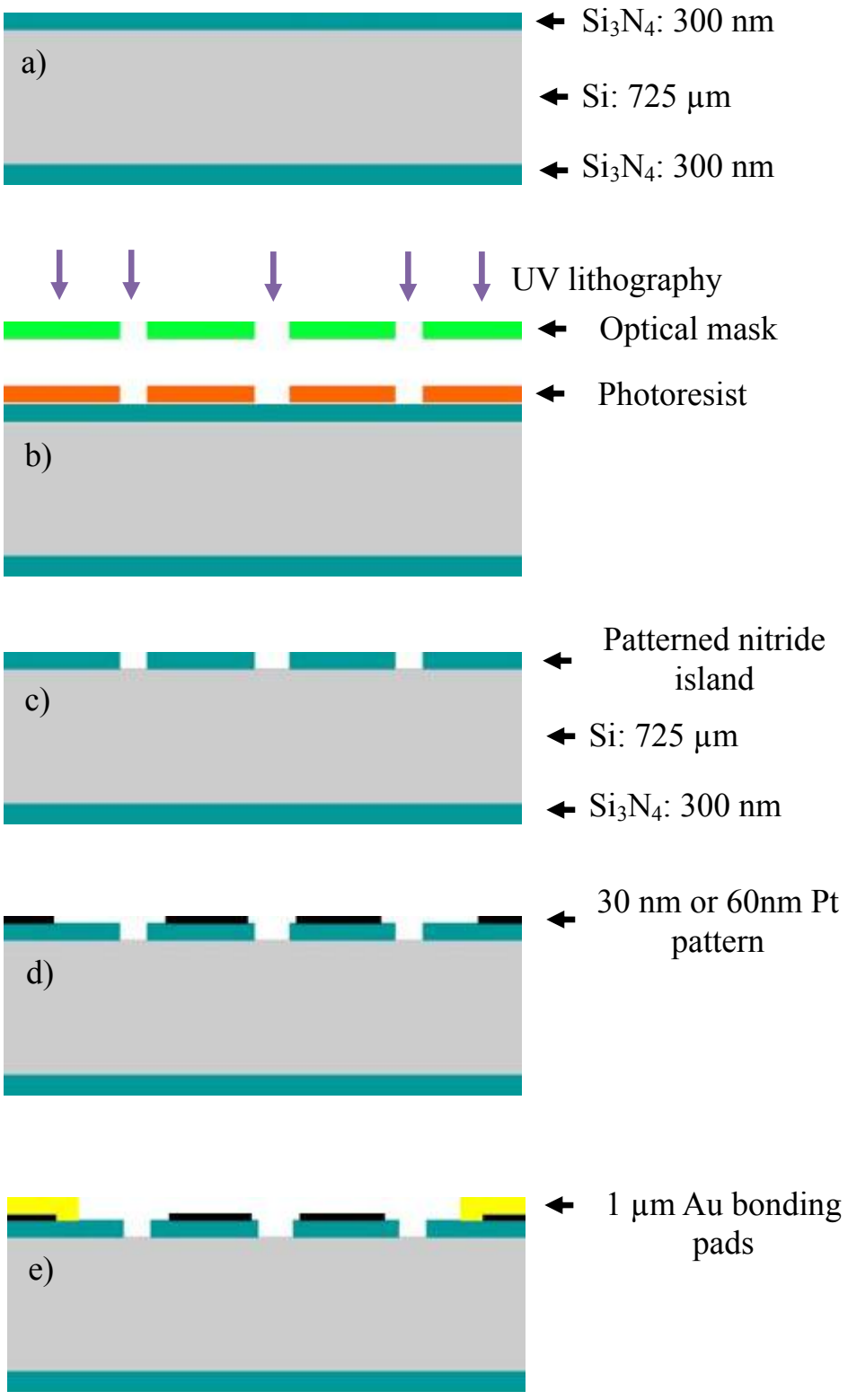
a)
Si_3N_4: 300 nm
Si: 725 µm
Si_3N_4: 300 nm
UV lithography
Optical mask
Photoresist
b)
Patterned nitride island
c)
Si: 725 µm
Si_3N_4: 300 nm
30 nm or 60nm Pt pattern
d)
1 µm Au bonding pads
e)

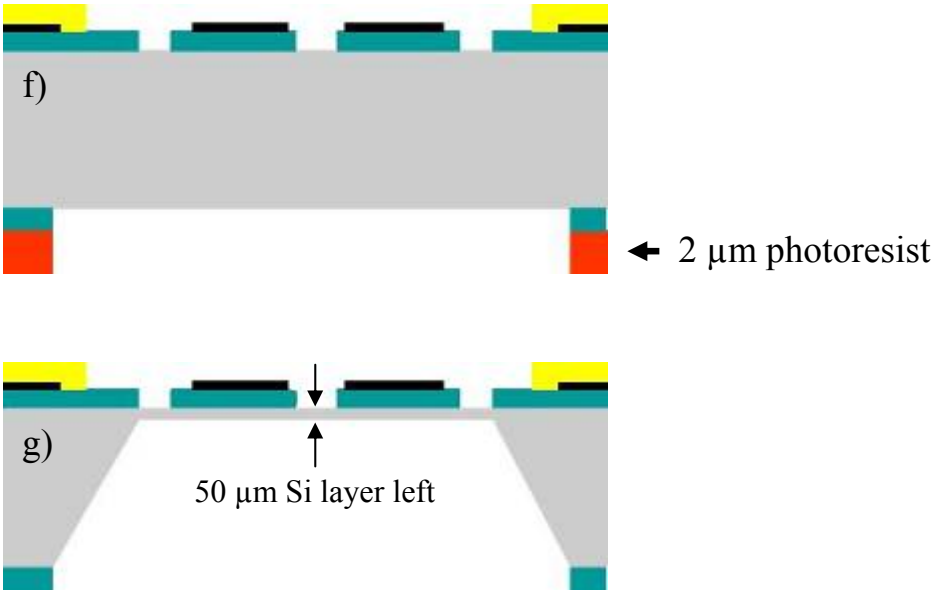

Figure 3.4: Fabrication process of METS device. (a) Starting nitride-coated wafer; (b) lithography photoresist patterning; (c) patterned nitride island; (d) Pt pattern on nitride island; (e) Au bonding pads pattern; (f) backside nitride window opening; and (g) wafer after KOH etching.

In order to open the backside of device, a 2 µm thick positive photoresist is spun on backside of the wafer. The patterned photoresist was then transferred to backside nitride layer via reactive ion etching (RIE) (Figure 3.4f). After RIE, the photoresist was stripped off. KOH solution with concentration of 40% was used to anisotropically etch silicon substrate from the backside at a temperature of 75°C. Under these conditions, the etching rate is around 55 µm per hour. The backside etching was precisely timed such that a 50 µm Si layer remains under the nitride island in order to support the structure during the dicing process (Figure 3.4g). Using this whole-wafer fabrication technique, about 600 densely-packed METS devices could be made on an 8 inch diameter wafer. The fabricated wafer was then diced into individual METS devices. Because of the 50 µm supporting Si layer, all suspended structures survived after dicing. The device was then released and fully suspended by removing 50 µm remaining Si layer under the nitride island using 40% KOH etching

at 80°C followed by a gentle blow dry. METS devices with different configuration were designed and fabricated in one wafer for different purposes.

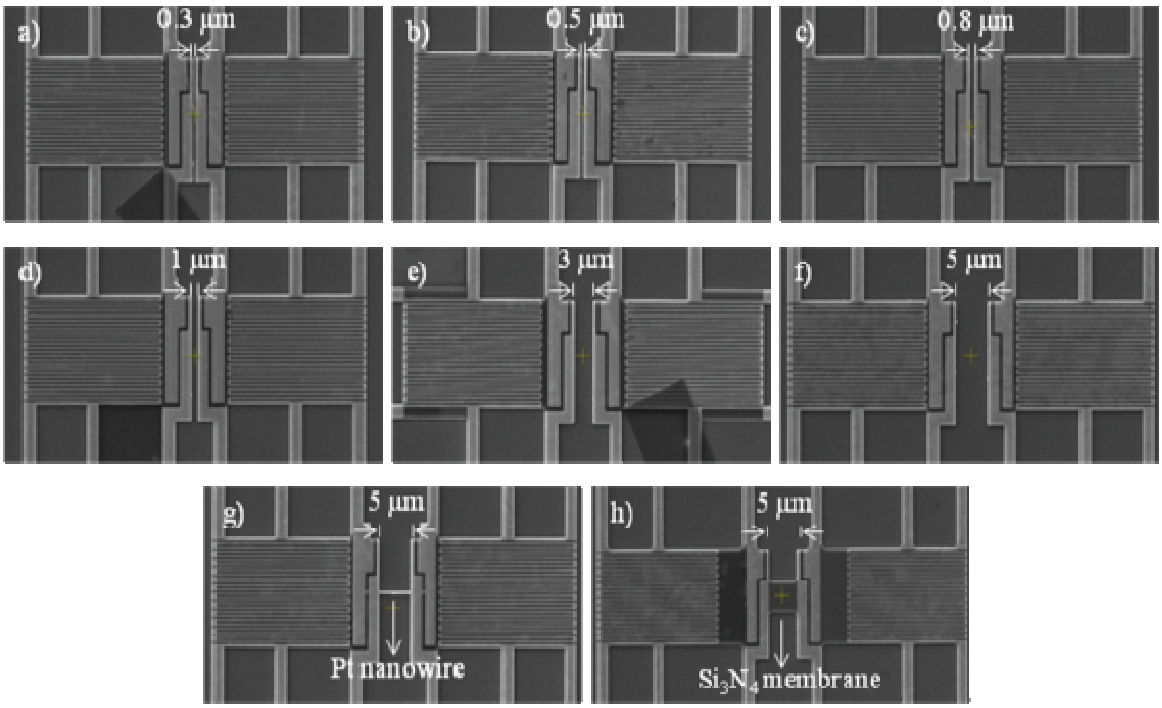

Figure 3.5: METS device with different gaps between two adjacent islands (a) 0.3 µm; (b) 0.5 µm; (c) 0.8 µm; (d) 1 µm; (e) 3 µm; (f) 5 µm, and integrated METS device (g) with 300 nm wide, 30 nm or 60 nm thick, 5 µm long Pt NW on 300 nm wide, 300 nm thick, 5 µm long nitride beam bridging the gap; and (h) with 5 µm wide, 300 nm thick, 5 µm long nitride film between two suspended islands as support layer .

There are devices with 0.3 µm, 0.5 µm, 0.8 µm, 1 µm, 3 µm and 5 µm gaps between two adjacent suspended islands which can be used for measurement of NWs or thin films of different length (Figure 3.5a, b, c, d, e, f). Figure 3.5g shows a device with integrated 300 nm wide, 30 nm or 60 nm thick, 5 µm long Pt NW on 300 nm wide, 300 nm thick, 5 µm long nitride beam bridging the gap for calibration purposes. A device with 5 µm wide, 300 nm thick, and 5 µm long nitride film integrated

between two suspended islands as supporting layer is shown in Figure 3.5h. Thin films or graphene can be placed on this supporting structure for thermal and electrical properties measurement.

One important feature of our METS device is that we can directly investigate the micro-structure of the same NW to determine its diameter, surface roughness and presence of contamination, and crystalline orientation and defects. This is possible because the METS devices were micro-machined with a through-substrate hole and can be mounted onto a custom-built TEM holder (Nanofactory SA2000, see Figure 3.6a) for microstructure analysis in a JEOL 2010F TEM. An *in situ* measurement can also be performed in TEM with electrical feedthroughs connected to source-measurement unit (SMU). During TEM imaging, the TEM die is mounted on the "Die base". Once the "Die base" has been clamped onto the holder's head, the socket pins will contact the Au bonding pads on the METS device. The socket pins are connected to measurement equipment outside via electrical feedthroughs. Figure 3.6b shows a low-magnification TEM image of a METS device with an individual NW.

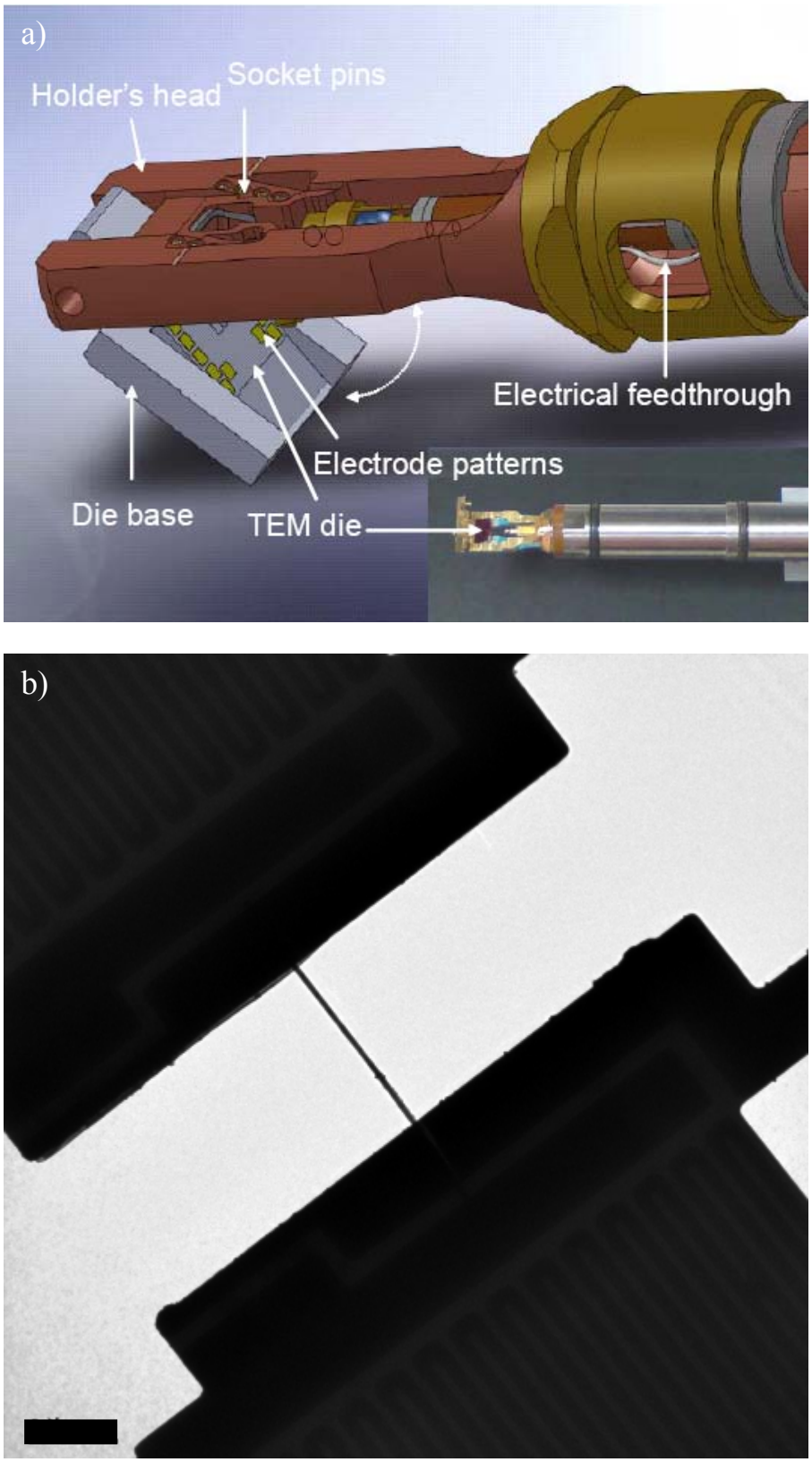

Figure 3.6: (a) Schematic of custom-made TEM holder (inset: actual image of TEM holder), and (b) low-magnification TEM image of a METS device with an individual NW (scale bar: 2 μm).

3.3. Sample preparation and characterization

To measure thermal and thermoelectric properties of nanostructures such as nanowires, nanotubes, or nanobelts, we first need to place them across four electrodes between the two suspended nitride islands. There are several methods to place the nanostructures, as follows.

3.3.1. Drop-cast method

In the first approach, nanostructure samples are first dispersed in ethanol or isopropanol by sonication, and then drop-casted onto suspended-island devices. After drying the solvent, an individual nanowire or nanotube may bridge the two islands. In a previous study, the probability of successful bridging was found to be very low, typically from 5% to 10% depending on the solution concentration. Because of low success rate, we seldom adopted this method to prepare NW samples on our devices.

3.3.2. Nano-manipulation method

In this approach, a sharp probe is used to pick up the sample, and then manipulated using a nano-manipulator (Kleindiek MM3A-EM) to place the sample between the two islands of the METS device. This process is performed in the vacuum chamber of a high-resolution scanning electron microscope (SEM - Philips XL30 FEG). Figure 3.7 shows SEM images of the procedure for Si NWs, showing sample pick-up, transfer, and placement.

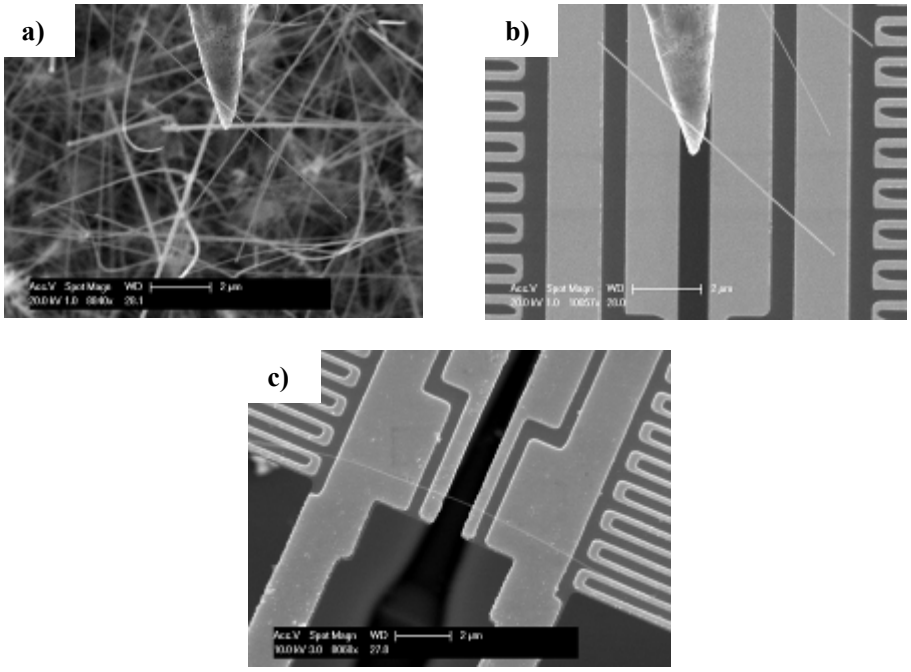

Figure 3.7: SEM images of nano-manipulation procedure for Si NWs: a) pick up the sample, b) transfer the sample to islands, and c) place the sample on the two islands.

In this thesis project, we used the nano-manipulation method to pick up and place various one-dimensional nanostructures onto the METS device for study, including Si NWs, VO_2 NWs, and ZnO NWs (Figure 3.8). In spite of the tedious process, we found that the nano-manipulation approach gives a high success rate and samples that are free of debris. After bridging nanostructures onto METS device, we can then proceed with measurements of thermal conductance, electrical conductance, and thermo-voltages.

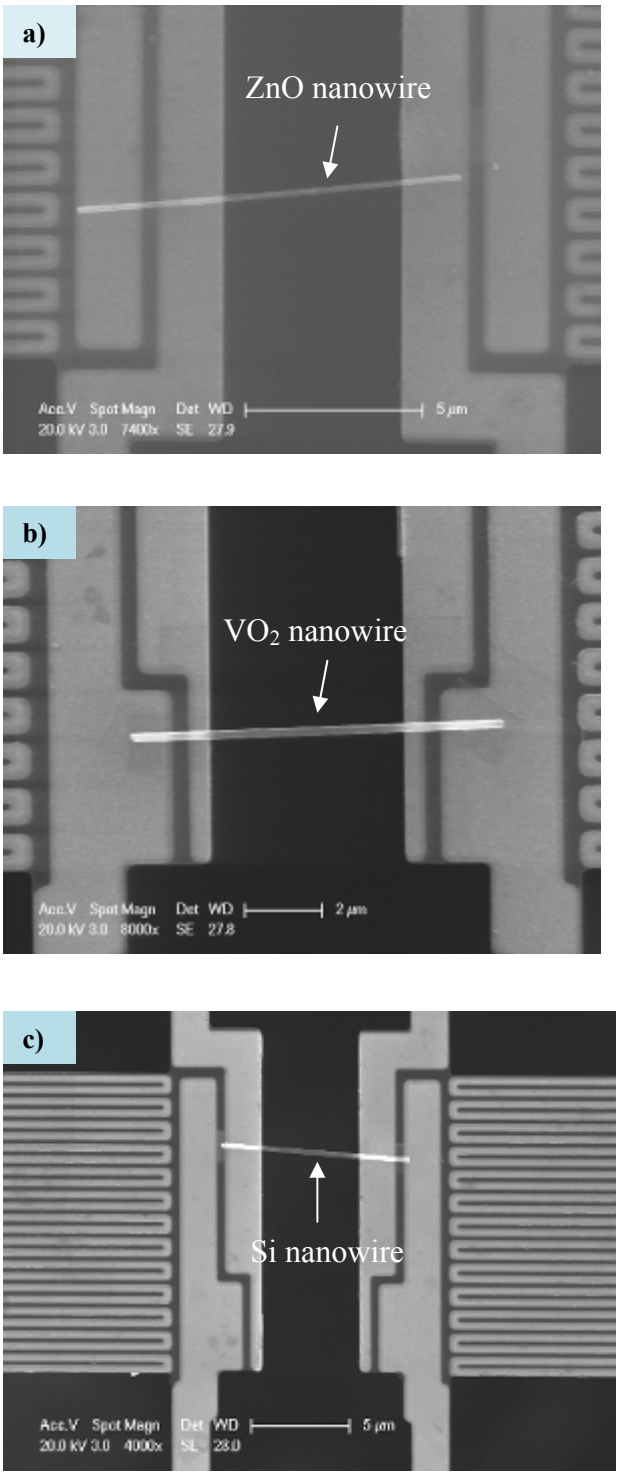

Figure 3.8: SEM images of (a) a ZnO NW, (b) a VO_2 NW, and (c) a Si NW placed between the two islands by nano-manipulation method.

3.3.3. Enhancement of thermal and electrical contacts

One problem arising is contact thermal resistance. The prepared NWs between the two islands only make line contacts, at best, with the underlying substrate with a line contact width of *b* as shown schematically in Figure 3.9, which could result in a large contact thermal resistance. For NWs, the heat transport through the wire is proportional to the square of the diameter, whereas the contact conductance is only linearly proportional to the line contact width, hence the diameter of NW. Consequently, the contact thermal resistance may dominate the total thermal resistance and result in an apparently low NW thermal conductivity.

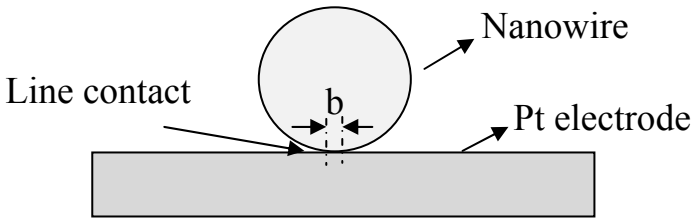

Figure 3.9: Schematic of prepared NW on the suspended islands showing that there is only a line contact between the NW and the Pt electrodes with a line contact width of *b*.

To improve the thermal contact between the sample and the islands, amorphous carbon films can be deposited on top of the sample-electrode contact areas. To do this, the SEM electron beam is focused on the contact region at a high magnification. Because of hydrocarbons in the SEM chamber, the electron beam induces the deposition of a carbonaceous film on the focused region. However, this method is only applicable to thin NWs with diameter less than 50 nm because of the relative thinness of the deposited carbonaceous film.

Alternatively, both ends of the NWs can also be bonded onto the Pt electrodes by Pt-C composite material using either electron-beam induced deposition (EBID) or focused ion beam induced deposition (FIBID) in a dual-beam FIB (FEI Quanta 200-3D). In EBID, a focused electron beam with acceleration voltage of 30 kV and high current was used. The incident beam induces secondary electron emission from the underlying material's surface which decomposes a metal-organic Pt precursor and deposits Pt metal on the contact areas. Unlike FIBID, EBID of Pt does not damage the underlying material, and hence it was adopted for NW samples with diameter in 50 – 210 nm range for thermal transport property characterization described in following chapters. Meanwhile, FIBID which uses a focused ion beam (30 kV, 10 pA) to induce Pt deposition enhances not only thermal contact but also electrical contact because of the surface cleaning effect through sputtering by the ion beam. For thermal and electrical property characterization of NWs, FIBID was selected to make the contacts. However, care was taken not to expose the suspended part of NW to the focused ion beam for any significant period of time to avoid NW damage. The carbonaceous or Pt/C composite deposits not only greatly enlarge the contact area between the sample and the Pt electrodes, but also mechanically anchor the sample to the islands. Figure 3.10 shows SEM images of the NW samples on islands with carbonaceous and Pt/C composite deposits.

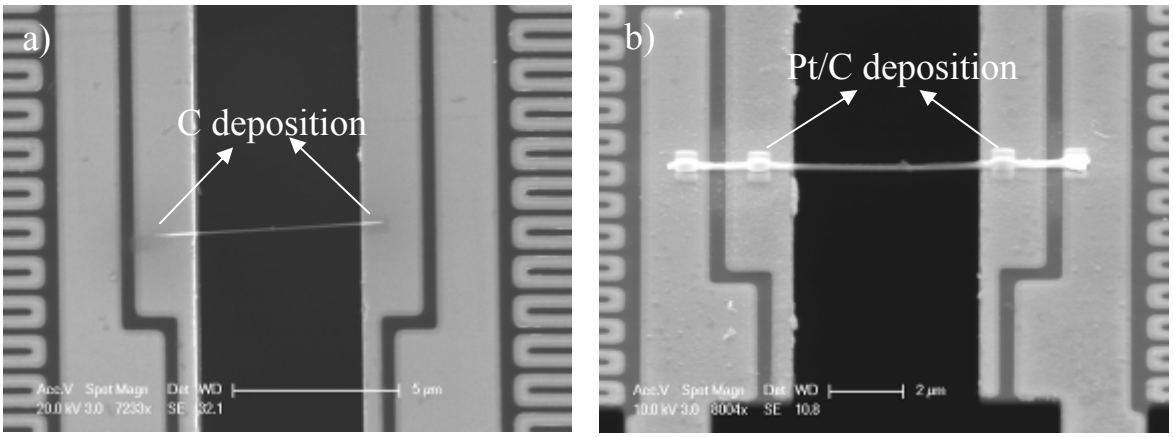

Figure 3.10: SEM images of mounted NW samples with (a) carbonaceous deposits, and (b) Pt/C composite deposits.

During the beam-induced deposition process, the suspended part of the sample should not be exposed to electron irradiation. However, some deposition always occurs within one to two microns away from the directly-exposed region. This unavoidable deposition on the surface of the sample is due to low intensity secondary electron emission created by backscattered electrons [8]. For this reason, in the following chapters all NW samples were prepared on METS devices with wide gaps of 5 μm to minimize the effect of undesired deposited contamination.

3.3.4. Surface contamination cleaning

In the pick-and-place process, an amorphous carbonaceous (a-C) layer would inevitably coat on the surface of the NWs by EBID of hydrocarbon residues from the SEM chamber. Figure 3.11 is the TEM image of a NW after the nano-manipulation process, showing that an a-C shell of 20 nm thickness has been formed on the surface of the sample. To remove this surface contamination, the NWs were cleaned using an Evactron RF plasma cleaner attached to the SEM chamber operated at a power of 14

W in 0.4 mbar of air for 2 hours. Repeated experiments showed that 2h-cleaning is enough to totally remove the contamination. After the Pt/C bonding process, the NW samples were cleaned for 2h again. Figure 3.12 shows the SEM images of a ZnO NW before and after plasma cleaning for 2h.

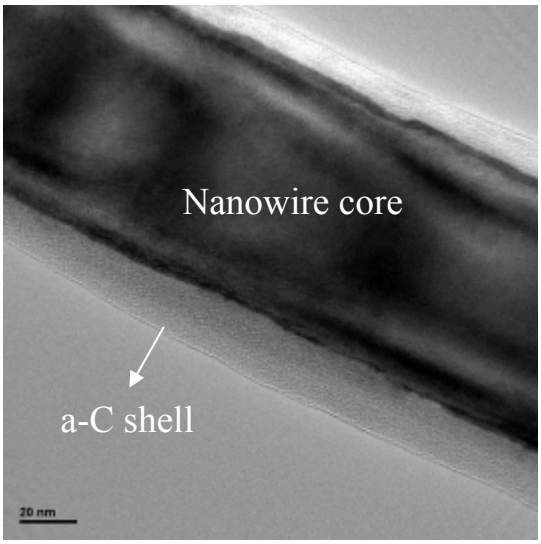

Figure 3.11: TEM image of a NW coated with a-C shell after nano-manipulation process.

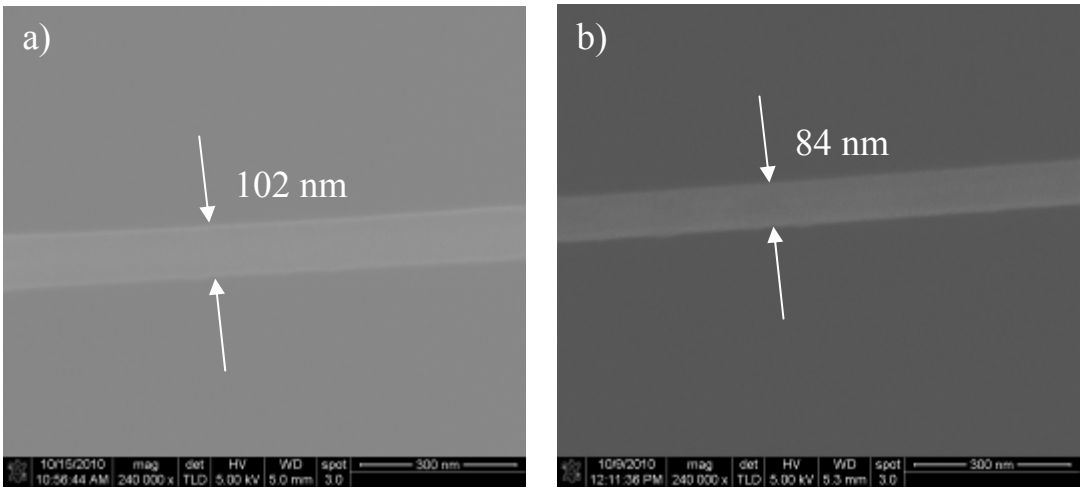

Figure 3.12: SEM image of NW (a) before plasma clean, and (b) after plasma clean.

3.4. Measurement setup and measurement mechanism

After sample placement, the METS device is placed on a cryogenic stage in a vacuum chamber with a base pressure better than 2×10^{-6} mbar. The cold stage was cooled by liquid nitrogen, and stabilized at various temperature set points by a temperature-controlled heater. The temperature using the liquid nitrogen cold-stage can be varied from 77 K to 500 K which gives a wide temperature range to investigate transport properties. The experiment was setup to measure the thermal conductance & thermoelectric properties of NWs as shown in Figure 3.13. Three lock-in amplifiers (SR380) and two ac & dc current sources (Keithley 6221), which are connected to the device inside the vacuum chamber via vacuum electrical feed-throughs, are employed for measurement.

For thermal conductance measurement, a temperature gradient could be created between two ends of the NW sample by heating up one membrane-island and measuring temperature changes in both islands. Figure 3.14 describes the connection of the measurement equipments to the METS device. To raise the temperature of the left hand side membrane-island, so-called heater island, a DC current (I) is passed through the Pt coil on that island using a current source (Keithley 6221) (from A to L). To measure the temperature rises of both islands, an ac current (i_{ac}) coupled with DC current (I) is passed through the Pt coil on the heater island (from A to L) and the same ac current (i_{ac}) was passed through the Pt coils on the other island, so-called sensor island, from (F to G) using current sources (Keithley 6221). The electrical resistances of the Pt coils were determined by measuring the voltage drop (v_{ac}) across the coils between B and M, and between E and H, respectively, by lock-in amplifiers (SR830, Stanford Research System). Consequently, the temperature changes at the heater and sensor islands were extracted from the resistance changes based on the

temperature coefficient of resistance of the Pt coils. The heating side can be switched by passing DC current to the other Pt coil from F to G and measuring resistance changes in both Pt coils.

An electrical conductance measurement could be carried out using four electrodes (C, D, I and K). A current is passed through NW between outer electrodes (from C to D) and the voltage drop is measured between inner electrodes (I and K) using a lock-in amplifier (SR830, Stanford Research System). The current is created from the output voltage of lock-in amplifier via a series resistance of 10 MΩ.

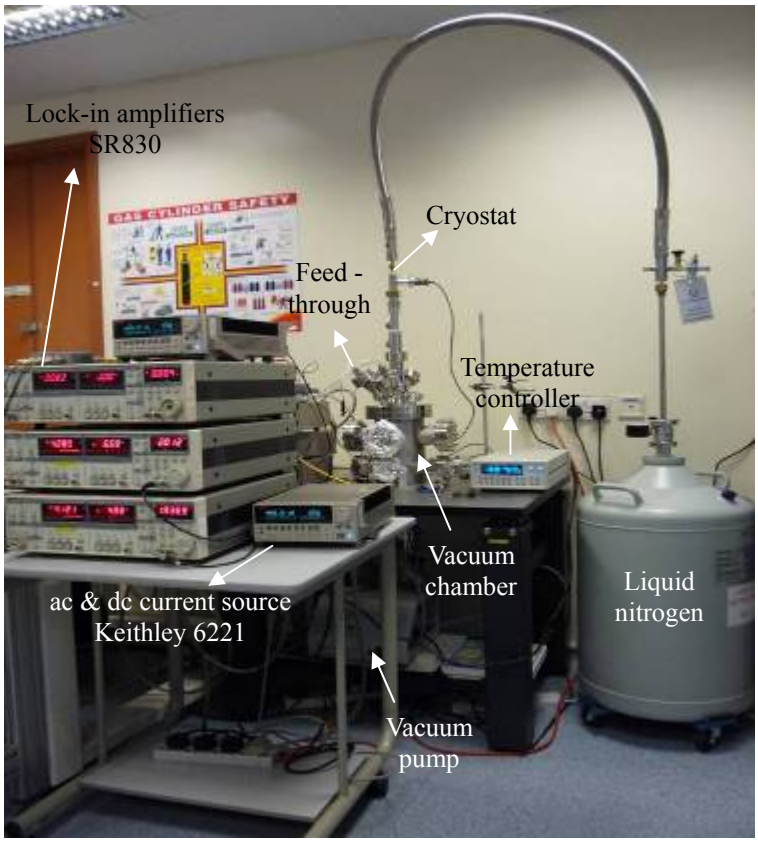

Figure 3.13: Experiment setup for nanostructure thermal conductivity and thermoelectric properties measurement.

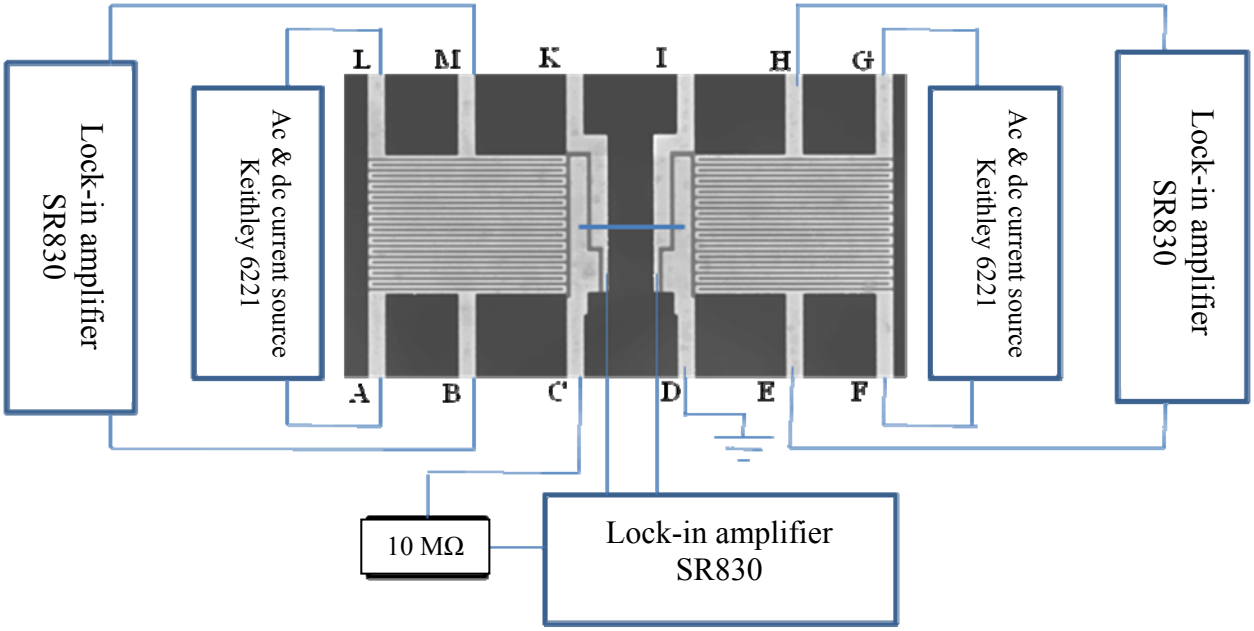

Figure 3.14: Schematic of the connection of the measurement equipment to the microdevice.

Lock-in amplifiers were chosen for our thermal and electrical measurements to minimize the effects of environmental noise through the choice of a working frequency that does not synchronize with the 50 Hz line frequency.

3.4.1. Thermal conductance measurement

The approach for measuring the thermal conductance of NWs is shown in Figure 3.15. The two suspended parts are denoted as the heater and sensor islands. A DC current (I) coupled with a small AC current with proper frequency (i_{ac}) passes through one of the heating platinum coil (PTC). An AC current is used to measure the resistance of the heater PTC and is much smaller than the DC current such that its contribution to Joule heating is negligible. After a certain time t, system will reach thermal steady state. Without changing the calculation results, we can normalize the

time by setting $t = 1$. A Joule heat $Q_h = I^2R_h$ is generated in this heater PTC, where R_h is the resistance of the PTC. A lock-in amplifier is used to measure the first harmonic component (v_{ac}) of the voltage drop across the PTC, yielding the resistance of the PTC $R_h = v_{ac}/i_{ac}$. A Joule heat of $2Q_L = 2I^2R_L$ is dissipated in the two Pt beams that supply the dc current to the heater PTC. The total Joule heat is therefore $Q_{tot} = Q_h + 2Q_L = I^2(R_h + 2R_L)$. At first, we assume that the temperature of the heater island is raised to a uniform temperature T_h. This assumption is appropriate because the internal thermal resistance of the small island is much smaller than that of long narrow beams connecting the island to the Si substrate anchor. A certain amount of the heat Q_2 is conducted through the NW sample from the heater island to the sensor island, raising the temperature of the sensor island to T_s. In vacuum and with a small ΔT_h ($T_h - T_0 < 10$K), the heat transfer between the two islands by air conduction and radiation is negligible compared to Q_2. Heat flow of Q_2 is then conducted to the environment through the six beams supporting the sensor island, as shown in the equivalent thermal resistance circuit diagram in Figure 3.15. The rest of the heat $Q_1 = Q_{tot} - Q_2$, is conducted to the environment through the other six beams supporting the heater island.

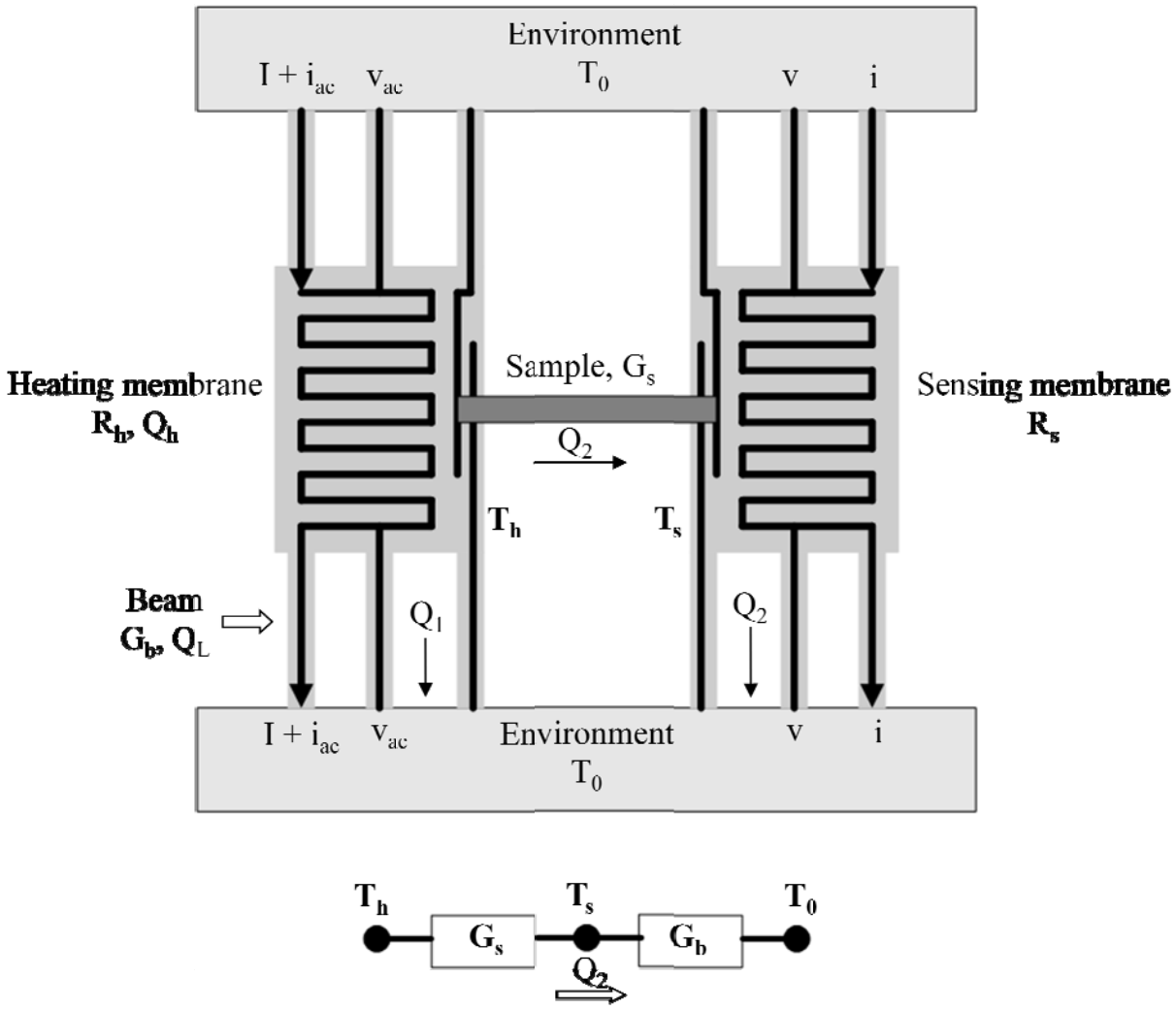

Figure 3.15: Schematic and thermal resistance circuit of the measurement scheme.

The six beams supporting each island are designed to be identical. Below 500K, the radiation heat loss from the island and six supporting beams to the environment are negligible compared to conduction heat transfer through the six beams. Thus, the total thermal conductance of the six beams can be defined as $G_b = 6k_bA/L$, where k_b, A, and L are the thermal conductivity, cross sectional area, and length of each beam, respectively. From the thermal resistance equivalent circuit, the heat transfer through the sensor island is:

$$Q_2 = G_{samp}(T_h - T_s) = G_b(T_s - T_0) \tag{3.3}$$

Likewise, heat transfer through the heater island is:

$$Q_1 = G_b(T_h - T_0) \tag{3.4}$$

where G_{samp} is the thermal conductance of the sample, consisting of the intrinsic thermal resistance of the NW and the contact thermal resistance between sample and two islands,

$$G_{samp} = \frac{1}{R_s} = \frac{1}{R_i + R_c} = (G_i^{-1} + G_c^{-1})^{-1} \tag{3.5}$$

where $G_i = \frac{k_i A_i}{L_i}$ is the intrinsic thermal conductance of NW sample, and k_i, L_i and A_i are thermal conductivity, length, and cross-sectional area of the NW sample segment between the two islands, respectively. G_c is the contact thermal conductance between the sample and two islands.

From Eq. (3.3) and Eq. (3.4), the total heat is:

$$Q_{tot} = Q_1 + Q_2 = G_b(\Delta T_h + \Delta T_s) \tag{3.5}$$

in which $\Delta T_s \equiv T_s - T_0$

Hence,

$$G_b = \frac{Q_{tot}}{\Delta T_h + \Delta T_s} = \frac{Q_h + Q_L}{\Delta T_h + \Delta T_s} \tag{3.6}$$

From Eq. (3.3) we have:

$$G_{samp} = \frac{\Delta T_s}{\Delta T_h - \Delta T_s} G_b \tag{3.7}$$

Q_h and Q_L can be calculated readily from the measured current and voltage drops across the heating PTC and the Pt leads. ΔT_h and ΔT_s are calculated from the measured resistance of the two PTCs and their temperature coefficient of resistance

($TCR \equiv \frac{dR/dT}{R}$). The four-point electrical resistance of the sensing PTC, R_s, is measured using a SR 830 lock-in amplifier with a sinusoidal excitation current at a proper frequency. The amplitude of sinusoidal current was chosen between 200 nA and 500 nA depending on NW sample, while the frequency was chosen at 2017.37 Hz. The reason for using such a frequency, which is explained in detail in following section, is to avoid noise signal from environment. The temperature rise ΔT_s of the sensor island depends on the dc current through the heater PTC, and is related to R_s by

$$\Delta T_s(I) = \frac{\Delta R_s(I)}{R_s(I) \times TCR}; \qquad \Delta R_s(I) \equiv R_s(I) - R_s(0) \tag{3.8}$$

Similarly, the temperature rises ΔT_h of the heater island can be calculated by

$$\Delta T_h(I) = \frac{\Delta R_h(I)}{R_h(I) \times TCR}; \qquad \Delta R_h(I) \equiv R_h(I) - R_h(0) \tag{3.9}$$

Using this ac – dc current coupling method, it is shown that the temperature rise in the heating island is frequency dependent [6]. Interestingly, in the low and high frequency limits, the temperature rise is expressed as:

$$\Delta T_h(I) = \frac{\Delta R_h(I)}{3 \times R_h(I) \times TCR}, \quad \text{for } f \ll \frac{1}{2\pi\tau} \tag{3.10}$$

$$\Delta T_h(I) = \frac{\Delta R_h(I)}{R_h(I) \times TCR}, \quad \text{for } f \gg \frac{1}{2\pi\tau} \tag{3.11}$$

where τ is the thermal time constant of the suspended device, $R_h = v_{ac}/i_{ac}$ is the calculated resistance of the heating PTC, i_{ac} is the same as sinusoidal current passing through sensor PTC, and v_{ac} is the measured first harmonic component of the voltage drop across the heater PTC. The difference in the temperature rise for different frequency ranges are caused by a first harmonic modulated heating term, $i_{ac}IR_h$. At a frequency that is very low compared to $1/(2\pi\tau)$, the $i_{ac}IR_h$ modulated heating yields a non-trivial first harmonic component in T_h. This further causes a non-trivial first

harmonic oscillation in R_h. Meanwhile, at a frequency that is very high compared to $1/(2\pi\tau)$, the $i_{ac}IR_h$ modulated heating yields a trivial first harmonic component in T_h, and hence, a trivial first harmonic oscillation in R_h.

In order to understand the dependence of temperature rise of the heater island on the frequency of ac sinusoidal current (i_{ac}) coupled with much larger dc current (I), we use ac-dc current source (Keithley 6221) to pass a 500 nA sinusoidal ac current with a frequency f ranging from 100 Hz to 2500 Hz coupled with 20 μA dc current through the heater PTC. A SR 830 lock-in amplifier is used to measure the first harmonic component (v_{ac}) of the voltage drop across the heater PTC, and then the temperature rise (ΔT_h) of the heater island is calculated.

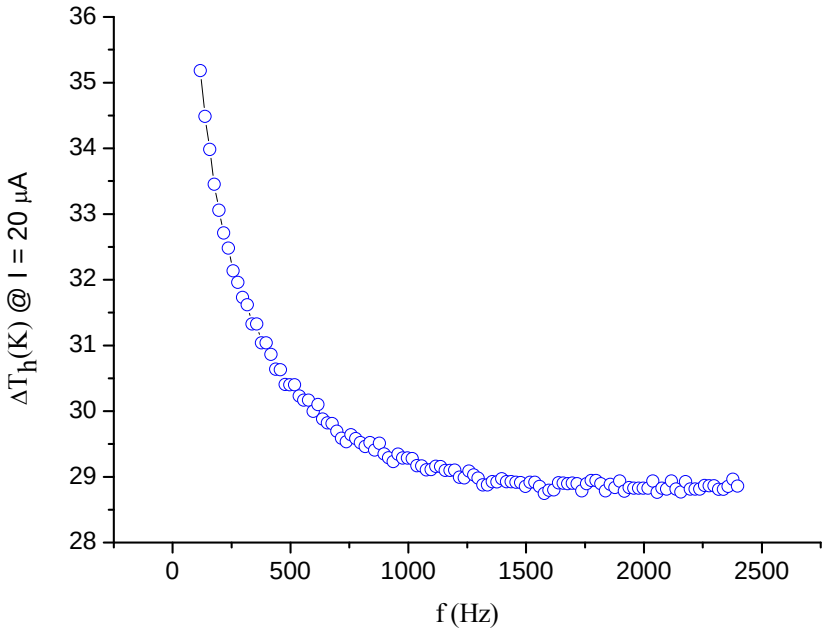

Figure 3.16: Frequency dependence of temperature rise in heater island with 500 nA sinusoidal ac current coupled with 20 μA dc current passed through heater PTC.

The dependence of temperature rise of the heater island on frequency of sinusoidal ac current (i_{ac}) passing through heater PTC is shown in Figure 3.16. As the frequency increases, the temperature rise (ΔT_h) decreases and reaches an asymptotic value in the frequency range from 1500 Hz to 2500 Hz. The lack of variation in this frequency region is necessary to obtain a precise measurement of temperature change, and consequently, give accurate results of the thermal conductance of the NW sample. Choosing a working frequency between 1500 Hz and 2500 Hz, which does not synchronize with 50 Hz to minimize the noise, is essential for accuracy of the measurement. For all the measurements described in following section, we will use a frequency of 2017.37 Hz for the heater side and a frequency of 1917.37 Hz for the sensor side.

Figure 3.17 shows the temperature rise of the heater and sensor islands of a reference METS device with a pre-fabricated Pt NW bridging the two islands. In this experiment, the dc current was ramped up from 0 μA to 10 μA in steps of 1 μA. The coupled ac sinusoidal current was kept the at the same magnitude of 500 nA at a frequency of 2017.37 Hz for the heater side and 1917.37 Hz for the sensor side. The temperature changes in the two islands versus heating current are shown in Figure 3.17b. Figure 3.17c shows that the temperature change increases linearly with I^2, which is proportional to total input heating power. This result is expected because the resistance changes should increase linearly with the applied power.

The temperature coefficient of resistance (TCR) of both the heater and sensor PTCs is extracted from the measured resistance of the PTCs at different temperatures. For each NW sample, the dependence of resistance of PTCs on temperature is measured, and the TCR is then extracted by curve fitting using polynomials. Figure

3.18 shows the temperature dependence of resistance of typical heater and sensor PTCs from 77 K to 300 K. The extracted TCRs of PTCs as function of temperature are shown in Figure 3.18b.

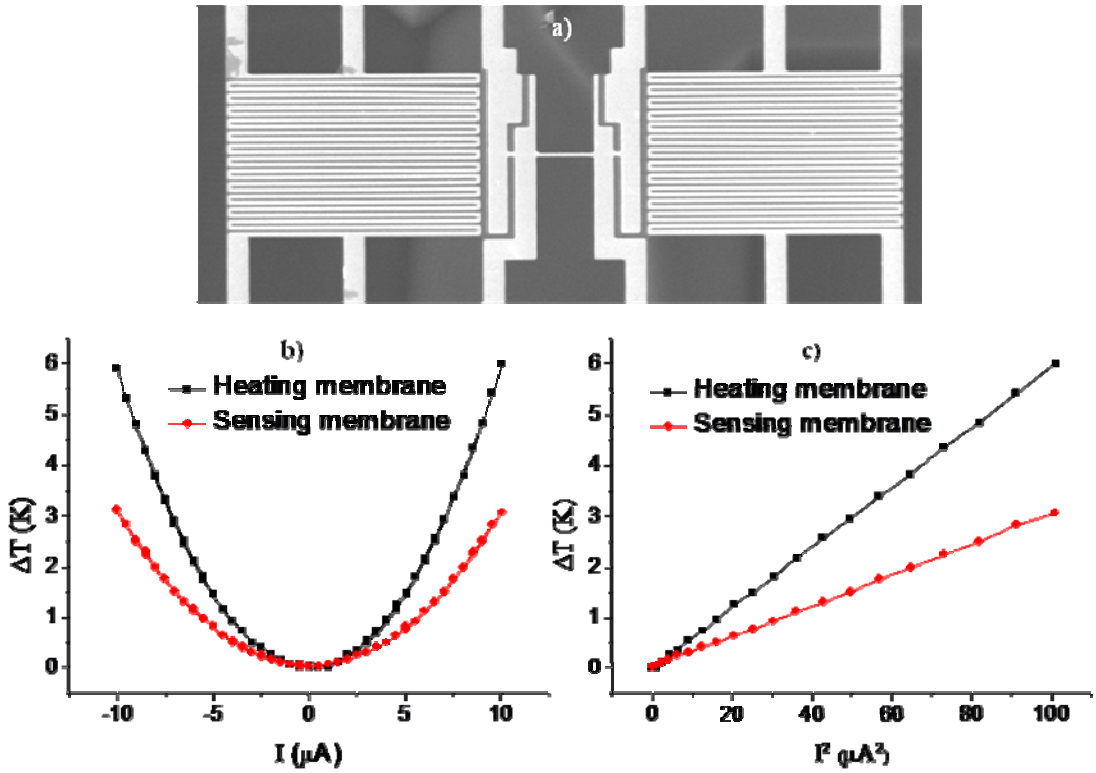

Figure 3.17: (a) SEM image of test MEST device with integrated Pt NW bridging the two islands; (b) Temperature changes in heater and sensor islands when the dc current ramped up from 0 μA to 10 μA; and (c) Temperature changes in heater and sensor island versus I^2 (proportional to total heating power).

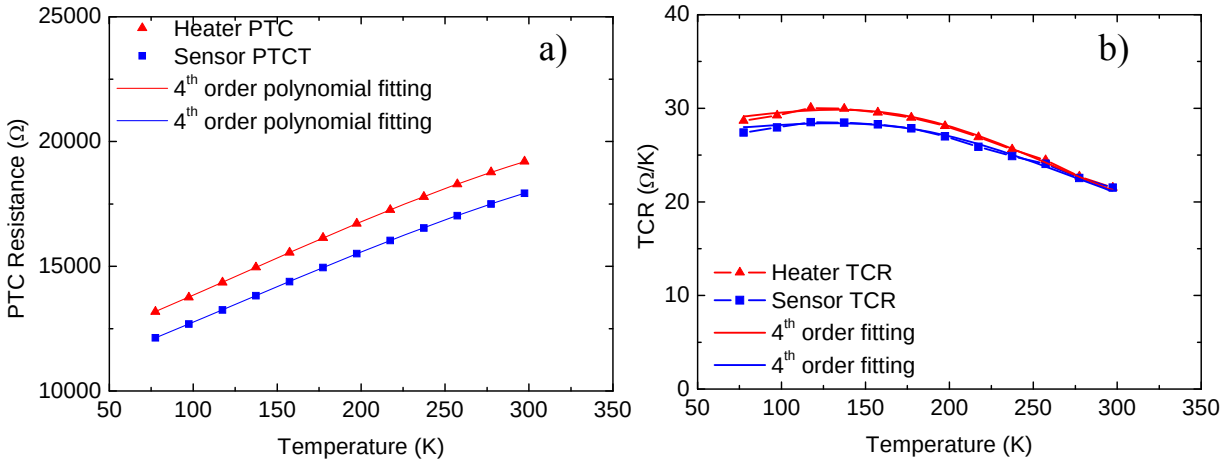

Figure 3.18: (a) Resistance versus temperature curve of a typical heater and sensor PTCs, and (b) Extracted TCR of heater and sensor PTCs as function of temperature (solid lines are 4th order polynomial fitting of experimental data).

3.4.2. Electrical conductance measurement

In this study, the electrical conductance of the sample is measured by using the four Pt electrodes (C, D, I, and K in Figure 3.14), which provides four-point probe measurement. Passing a current I_{CD} through two ends of the sample via two outer electrodes, and then measuring the voltage at two inner electrodes V_{IK}, the electrical conductance of the sample can be calculated:

$$G_e = \frac{1}{R_s} = \frac{I_{CD}}{V_{IK}} \tag{3.12}$$

Using this four-point measurement, we can avoid the effect of the contact resistance. Hence, an accurate value of electrical conductance of the sample can be obtained.

To improve the electrical contact and minimize the contact electrical resistance, an FIB can be used to deposit Pt-C metal pads on top of the sample-electrode contacts. The FIB deposition can also break through the amorphous carbonaceous layer caused by contamination or oxide layer of a semiconductor NW to

reduce the contact resistance.

3.4.3. Seebeck coefficient measurement

By passing current through the Pt heating loop, we can heat up one island so that a temperature gradient $\Delta T = T_h - T_s$ between the two ends of the sample is established, where T_h, T_s is the temperature of the heater and sensor islands, respectively. This temperature difference yields a thermoelectric voltage that is measured using a SR830 lock-in amplifier between the two inner Pt electrodes and expressed by the following formula:

$$V_{TE} = (S_s - S_{Pt})(T_h - T_s) \tag{3.13}$$

The Seebeck coefficient of the Pt electrode (S_{Pt}) is calibrated separately. By measuring T_h, T_s, and V_{TE}, the Seebeck coefficient of the sample (S_s) can be obtained.

3.5. Spatially resolved electron-beam probing technique for thermal resistance measurement

Beyond normal usage of the SEM for sample imaging, Leamy [9] employed the electron beam in the Electron Beam Induced Conductivity (EBIC) method to study and characterize semiconductor materials. In this technique, the electron beam creates charge carriers inside the semiconductor material which are collected by an electric field within the material and sensed as a current in an external circuit. The carrier life-time and diffusion length can be determined using this technique. Thermal properties of materials had been studied using various techniques. Among them, using

laser beam in photoacoustic piezoelectric technique [10 – 13] or electron beam in scanning electron-acoustic microscopy (SEAM) [14] to heat up samples were used to determined thermal diffusivity. The SEAM uses the dependence of the electron-acoustic signal on the modulation frequency of the electron beam to characterize the thermal diffusivity based on thermoelastic theory. However, the SEAM technique was only applicable for bulk plate samples. Exploiting an electron beam in the SEM to study and characterize thermal transport in nanostructures has not been carried out so far.

In this chapter, we describe a technique that uses the electron beam of SEM to locally heat up a point on NW sample on METS device. The heat then spreads to both ends of the NW, raising the temperature of both suspended membrane-islands. By measuring the temperature change in both islands as the electron beam moves along NW, we can extract the spatial distribution of thermal resistance of the NW. This technique, so-called spatially resolved electron-beam probing (SREP) technique, is presented in details in following sections. The same method can be used to measure the contact thermal resistance and interfacial thermal resistance.

3.5.1. Principles and methodology of the technique

Figure 3.19 shows the schematic diagram of the method, in which we assume that the temperature of the substrate (environment) always kept at room temperature (T_0). The temperature of the left island and the right island are denoted as T_L and T_R, respectively. In order to position the electron beam along the NW sample, the reduced-area mode of the SEM, with the line-scan direction perpendicular to the NW axis, was used with slow scanning speed in the frame direction. We use the reduced-

area mode instead of spot mode to receive continuous output signals during electron beam scanning.

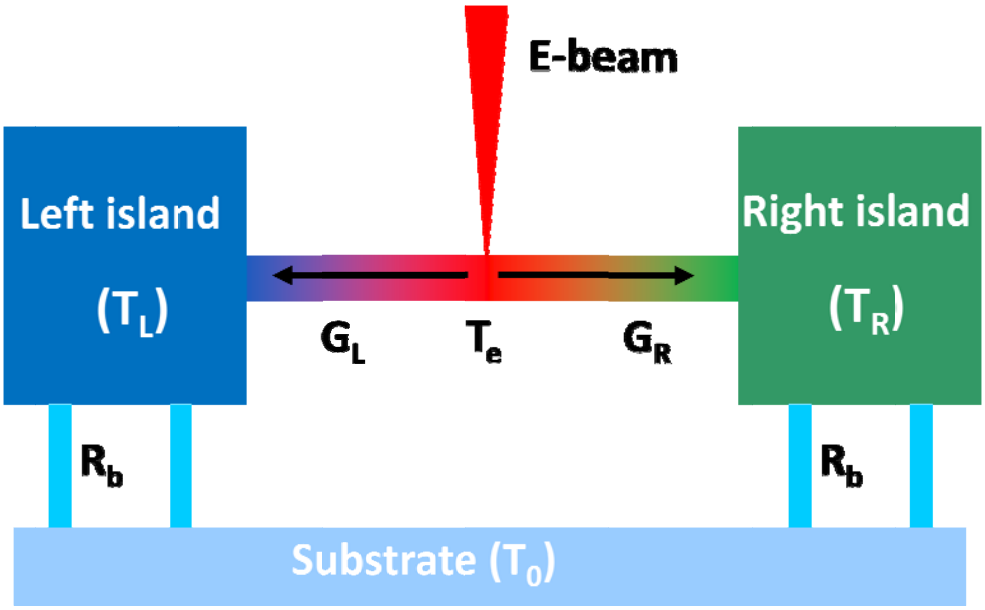

Figure 3.19: Schematic diagram of spatially resolved electron-beam probing technique (SREP) for thermal resistance measurement.

a) Equivalent thermal resistance circuit

The schematic of a NW sample on the METS device and equivalent thermal resistance circuit are shown in Figure 3.20. The thermal resistance of six beams connecting each suspended island to the substrate is denoted as R_b (from B_1 to A and from D_1 to A in the equivalent circuit). The thermal resistance of the contacts between NW sample and two islands are R_{c1} and R_{c2}. Because of the same conditions to make contacts, we can assume that $R_{c1} = R_{c2} = R_c$. Thermal resistance of each membrane-island and thermal resistance of NW sample are denoted as R_m and R_s, respectively.

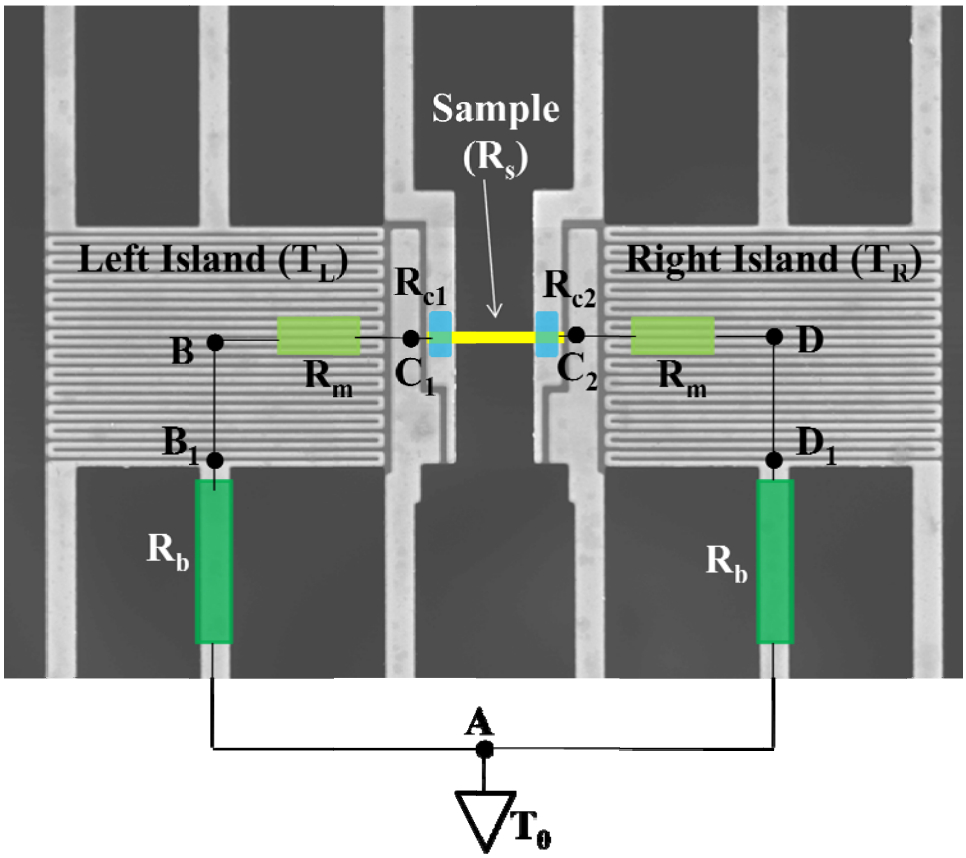

Figure 3.20: Schematic of NW sample on the METS device and equivalent thermal resistance circuit. In which, R_b is the thermal resistance of six beams connecting the membrane-island to the substrate, R_m is the thermal resistance of membrane-island, R_{c1} and R_{c2} are the thermal resistance of the two contacts between NW sample and the membrane-island, and R_s is the thermal resistance of NW sample. The left hand side and the right hand side suspended membranes are supposed to be identical.

b) Measurement mechanism

Firstly, we will derive the thermal equilibrium equation when the electron beam spots on the NW at a position S_i. The equivalent thermal resistance circuit is shown in Figure 3.21a.

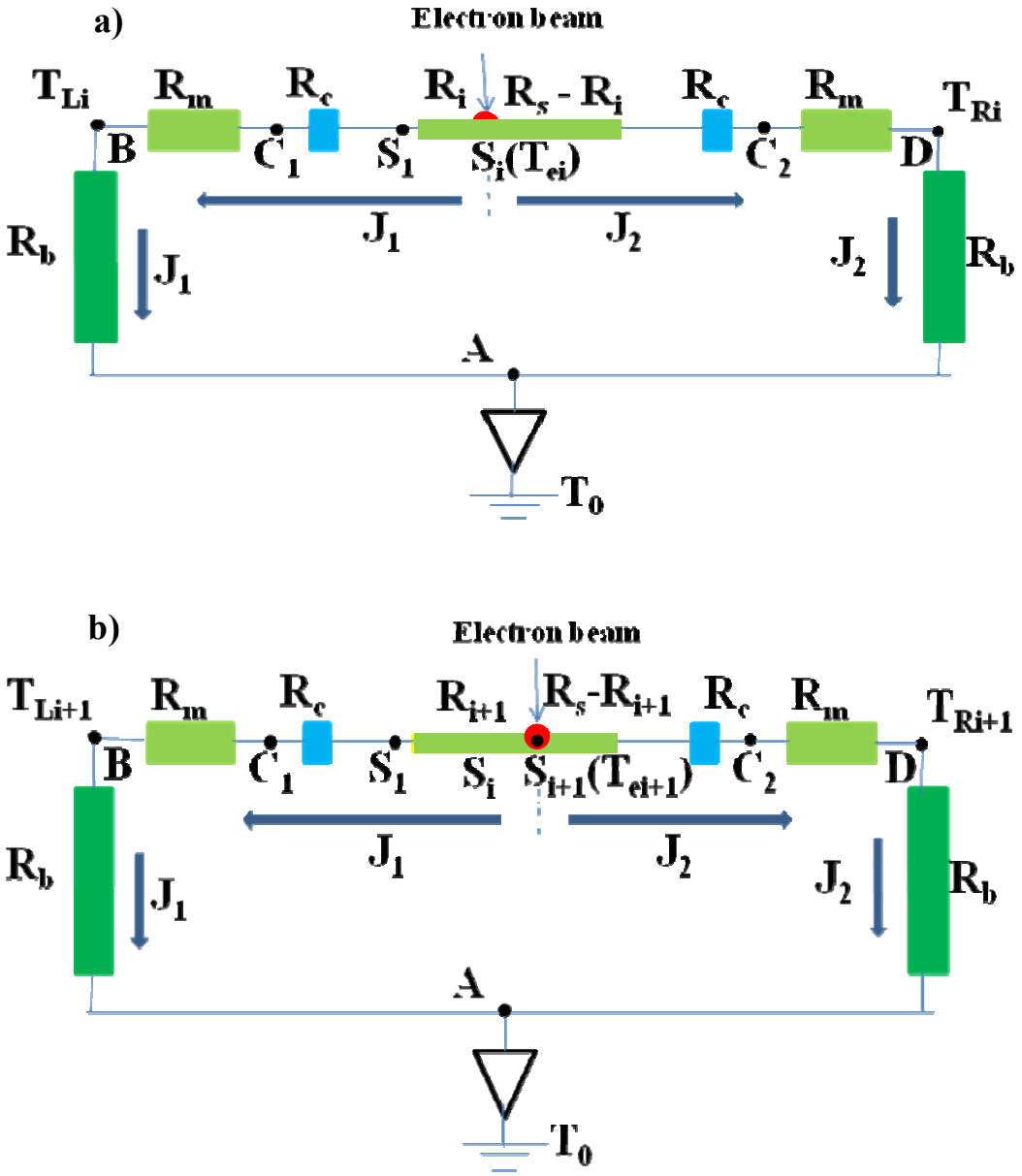

Figure 3.21: Equivalent thermal resistance circuit when the electron beam spots on (a) position S_i, and (b) position S_{i+1} on the NW sample.

When the electron beam is positioned on the NW at the point S_i, the temperature at that point is raised to T_{ei} which depends on the absorption of electron beam energy. Because of a temperature gradient, heat will conduct through the both sides of NW via the left- and right-island and sink into the substrate with the heat current of J_1 and J_2, respectively. At steady-state, which can be archived reasonably quickly, the

temperature in the left- and right-islands rises to T_{Li} and T_{Ri}, respectively, which can be precisely determined by measuring the electrical resistance change in the PTCs. Similar to an electrical resistance circuit, at the steady-state the temperature T_{ei} can be expressed as:

$$T_{ei} = T_0 + J_1(R_b + R_m + R_c + R_i) \tag{3.14}$$

in which, R_i is the thermal resistance of a part from irradiated spot to the left hand side end of the NW. The heat current J_1 can be determined by

$$J_1 = \frac{T_{Li} - T_0}{R_b} = \frac{\Delta T_{Li}}{R_b} \tag{3.15}$$

On the other hand, T_{ei} can also be expressed as

$$T_{ei} = T_0 + J_2(R_b + R_m + R_c + R_s - R_i) \tag{3.16}$$

In which, R_s - R_i is the thermal resistance of a part from irradiated spot to the right hand side end of the NW. The heat current J_2 can be determined by

$$J_2 = \frac{T_{Ri} - T_0}{R_b} = \frac{\Delta T_{Ri}}{R_b} \tag{3.17}$$

ΔT_{Li} and ΔT_{Ri} are the temperature rises in the left- and right-island, respectively.

Substituting J_1 and J_2 from Eq. (3.15) and Eq. (3.17) into Eq. (3.14) and Eq. (3.16) we obtain

$$T_{ei} - T_0 = \frac{\Delta T_{Li}}{R_b}(R_b + R_m + R_c + R_i) = \frac{\Delta T_{Ri}}{R_b}(R_b + R_m + R_c + R_s - R_i) \tag{3.18}$$

By setting a ratio $\alpha_i = \frac{\Delta T_{Li}}{\Delta T_{Ri}}$, Eq. (3.18) can be rewritten as

$$\alpha_i + \frac{\alpha_i}{R_b}(R_m + R_c + R_i) = 1 + \frac{1}{R_b}(R_m + R_c + R_s - R_i) \tag{3.19}$$

Similarly, when the electron beam is positioned at point S_{i+1} (Figure 3.21b), the following equation can be derived

$$\alpha_{i+1} + \frac{\alpha_{i+1}}{R_b}(R_m + R_c + R_{i+1}) = 1 + \frac{1}{R_b}(R_m + R_c + R_s - R_{i+1}) \tag{3.20}$$

where $\alpha_{i+1} = \frac{\Delta T_{Li+1}}{\Delta T_{Ri+1}}$ is the ratio of the temperature rise in the left-island over the temperature rise in the right-island when position S_{i+1} is heated up by electron beam. The ratios α_i and α_{i+1} are well defined by measuring the temperature changes in both islands.

In order to find the relation between R_i and R_{i+1}, we need to determine the relation between the thermal resistance of the membrane-island (R_m), the contact (R_c) and the NW sample (R_s). To do this, the electron beam is positioned on the left-island (point B) raising the temperature of that island to T_{L0}. Some heat will conduct through the NW sample and heat the right-island up to temperature T_{R0}. The equivalent thermal resistance circuit for this case is shown in Figure 3.22.

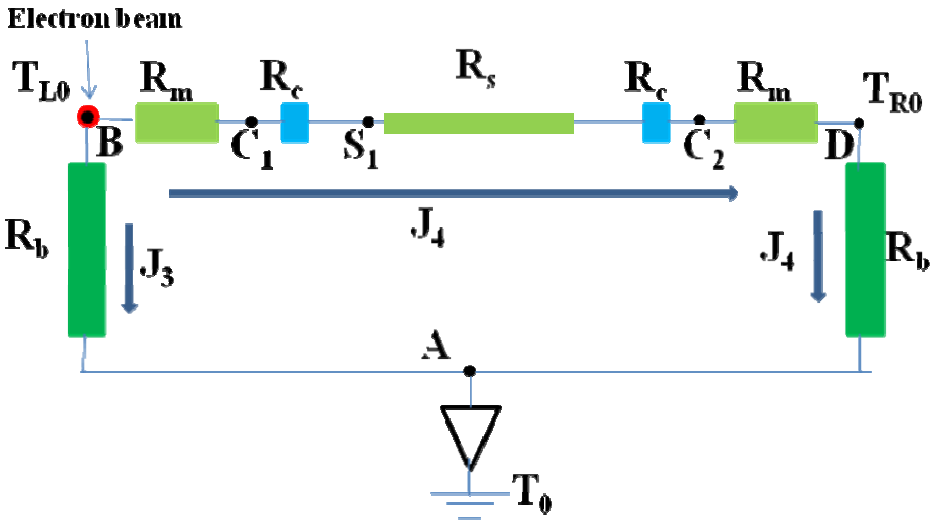

Figure 3.22: Equivalent thermal resistance circuit when the electron beam spots on the left-island (point B).

At the steady-state, the temperature T_{L0} can be expressed as

$$T_{L0} = T_0 + J_4(2R_m + 2R_b + R_s + R_b) \tag{3.21}$$

where J_4 is the heat current passing from the left-island to the substrate via the NW sample and the right-island and can be determined by

$$J_4 = \frac{T_{R0} - T_0}{R_b} = \frac{\Delta T_{R0}}{R_b} \tag{3.22}$$

Substituting Eq. (3.22) into Eq. (3.21) and denoting $\alpha_0 = \frac{T_{L0} - T_0}{T_{R0} - T_0} = \frac{\Delta T_{L0}}{\Delta T_{R0}}$ we obtain

$$\alpha_0 = 1 + \frac{1}{R_b}(2R_m + 2R_c + R_s) \tag{3.23}$$

Combining Eq. (3.23) with Eq. (3.19) and Eq. (3.23) with Eq. (3.20), we can obtain the relation between R_i and R_{i+1}

$$R_m + R_c + R_i = \frac{\alpha_0 - \alpha_i}{\alpha_i + 1} R_b \tag{3.24}$$

and $$R_m + R_c + R_{i+1} = \frac{\alpha_0 - \alpha_{i+1}}{\alpha_{i+1} + 1} R_b \tag{3.25}$$

Hence,

$$\Delta R_i = R_{i+1} - R_i = \frac{(\alpha_i - \alpha_{i+1})(1 + \alpha_0)}{(1 + \alpha_{i+1})(1 + \alpha_i)} R_b \tag{3.26}$$

We can clearly see from Eq. (3.26) that the temperature rise at the heating point by electron beam (T_e) does not play a role. The ratios α_0, α_i and α_{i+1} are the only parameters used to derive the spatial distribution of thermal resistance of the NW (ΔR_i) and are defined by measuring the temperature changes in both membrane-islands corresponding with each irradiated point. The advantage of this technique is that the exact heating power of the electron beam, hence T_e, need not be determined; however, the power should be sufficient to effect a temperature change in both islands in a detectable range (normally > 0.5K).

Instead of using the spot mode (i.e., stationary beam) of the SEM to irradiate individual positions on the NW, which we found susceptible to image drift as a result of contamination build-up and charging effects, we employed the reduced-area mode of the SEM, which is aligned along the NW sample (white dash-dotted line in Figure 3.23), with slow scanning speed in the frame direction. At each position on the NW which is irradiated when the electron beam impinges on the sample, the relative thermal resistance $R_i^{'} = R_i + R_m + R_c$ of a part from irradiated point to left-island of the NW is calculated from Eq. (3.24). By accumulating the relative thermal resistance of a part of the NW when the electron beam scans from one end to the other end of the

reduced area, we can draw a thermal resistance profile along the NW. Figure 3.23 show thermal resistance profile of 70 nm thick, 300 nm wide, 5 µm long Pt NW on a 300 nm thick, 300 nm wide, 5 µm long SiN_x bridge between the two islands. The difference in relative thermal resistance between A and B gives the thermal resistance of the bridging sample, which is $R_s = 1.35 \times 10^6$ (K/W) in this case.

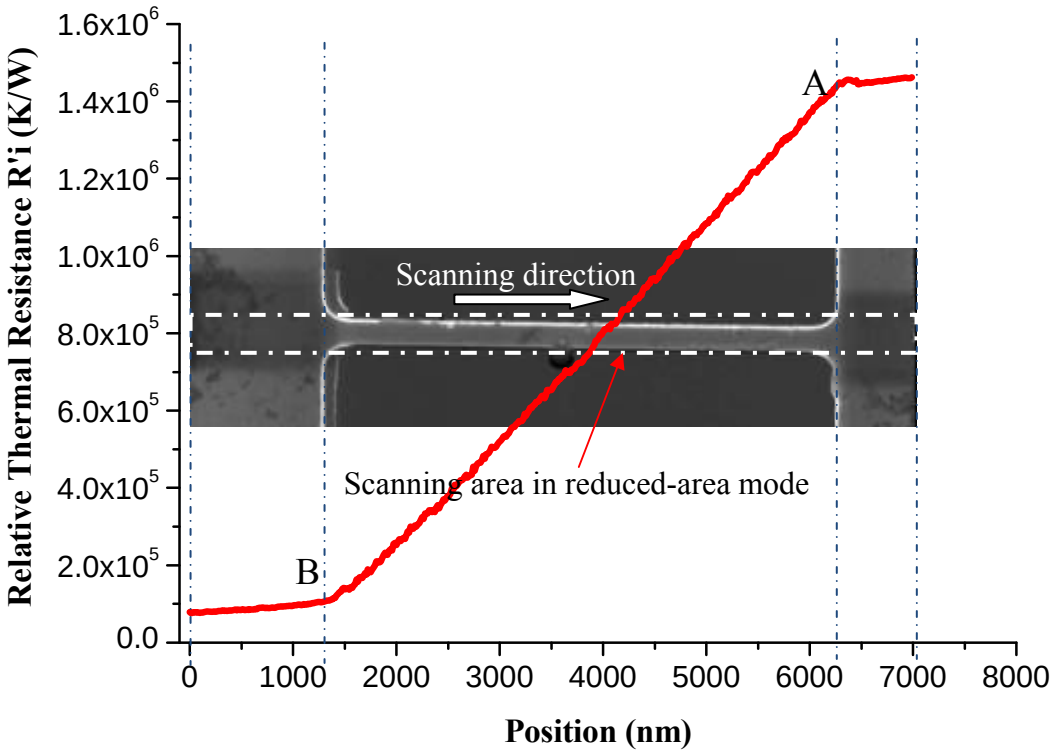

Figure 3.23: Thermal resistance profile of 70 nm thick, 300 nm wide, 5 µm long Pt NW on 300 nm thick, 300 nm wide, 5 µm long SiN_x bridging two islands.

c) Determination of α_0

In order to carry out the thermal resistance profile, the value of α_0 needs to be pre-determined by positioning electron beam on the left-island and measuring temperature changes in both islands. However, because of inhomogeneous temperature distribution in the island when it is locally heated up by the electron beam, the

measured temperature ΔT_{L0}, hence the value of α_0, varies with different irradiated positions. The dependence of the ratio $\Delta T_L/\Delta T_R$ on the position of the heating electron beam irradiating on the left-island is shown in Figure 3.24a, in which the scanning area is presented by white dash-dotted lines and the scanning direction is from the left hand side to the right hand side. To determine the proper value of α_0 used in Eq.(3.24) we need to match the ratio of the temperature change in the left-island and in the right-island ($\Delta T_L/\Delta T_R$) when heating up the left-island by either the electron beam or by resistive heating. The thermal conductance of the sample (including contacts) is calculated from (Section 3.4.1)

$$G_s = G_b \frac{1}{\frac{\Delta T_L}{\Delta T_R} - 1} = G_b \frac{1}{\alpha - 1} \tag{3.27}$$

To give the same value of thermal conductance, the ratio $\alpha = \Delta T_L/\Delta T_R$ should be the same irrespective of the heating method.

The temperature rise in the left-island (ΔT_L) versus temperature rise in the right-island (ΔT_R) using resistive heating is shown in Figure 3.24b. The slope of the curve corresponding to the ratio $\alpha = \Delta T_L/\Delta T_R$ is around 1.883. By comparing with the ratio $\Delta T_L/\Delta T_R$ determined by electron beam heating method (red dash-dotted line in Figure 3.24a), we deduced that the ratio α_0 should be pre-determined by irradiating electron beam at a point near the centre of the left-island.

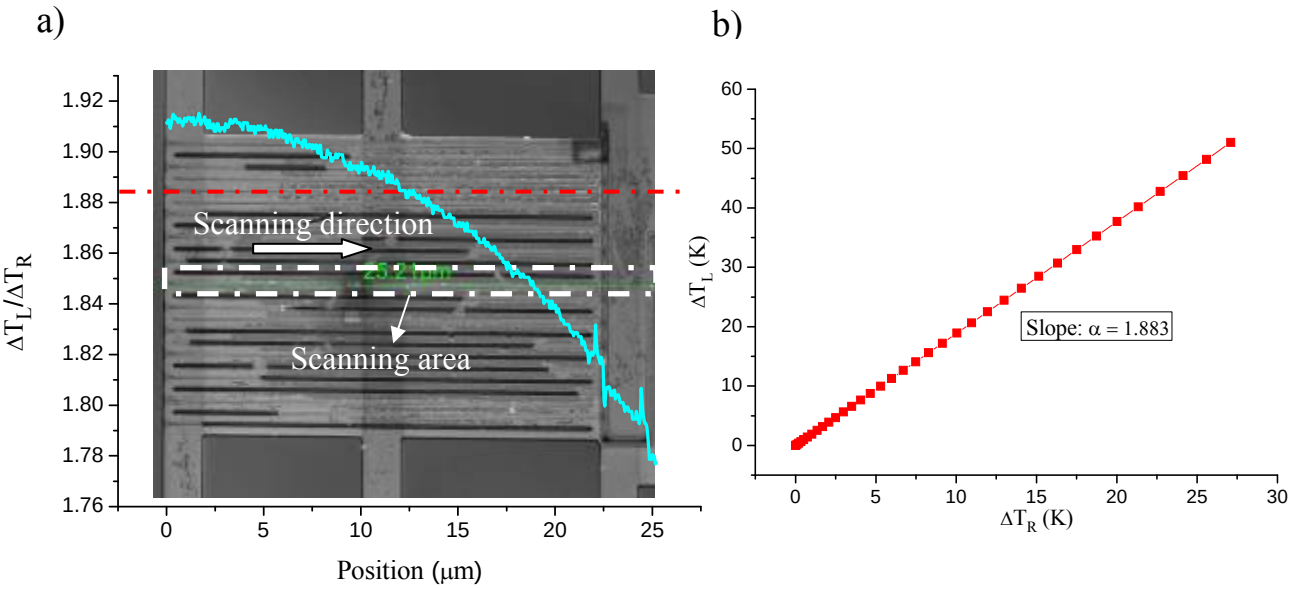

Figure 3.24: (a) The dependence of $\Delta T_L/\Delta T_R$ on the position of the heating electron beam irradiating on the left-island. (b) The temperature rise in the left-island (ΔT_L) versus the temperature rise in the right-island in dc current heating method.

3.5.2. Experimental setup

The METS device with NW sample can be mounted and wire-bonded on a dual in-line package (DIP). The DIP sample is placed in the SEM chamber (Nova SEM 230) using a custom designed holder. The two PTCs on both membrane-islands are connected to two lock-in amplifiers (SR 830) and two current sources (Keithley 6221) via vacuum feed-through for four-point measurement of electrical resistance of both PTCs (Figure 3.25). The temperature changes in both islands are inferred from electrical resistances change in the two PTCs. A cooling & heating stage can also be used to control the temperature of the sample over a range of 77K to 400K during measurement.

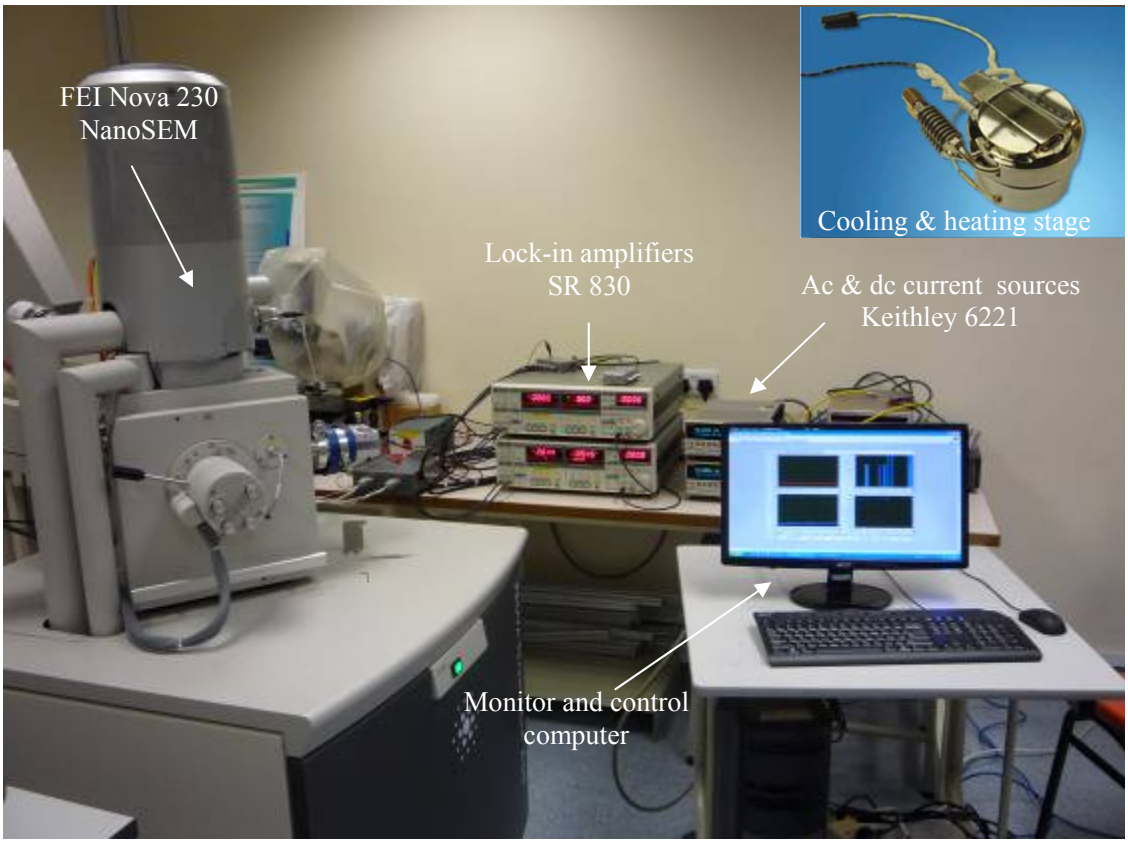

Figure 3.25: Experiment setup of spatially resolved electron-beam probing technique for thermal resistance measurement of NWs as well as contacts and interfaces.

As mentioned above, the amount of absorbed power from the electron beam, which is proportional to total temperature change in both islands, should be sufficiently large to achieve sufficient high signal-to-noise ratio in the measurement. For experiments conducted in an FEI Nova 230 NanoSEM (immersion lens mode), a typical operating condition is 2 keV beam-landing energy with a beam current of 0.11 nA for NW samples. Under these conditions, the total temperature rise in both islands in the order of several tens of Kelvin. For thick samples with strong electron beam absorption, the beam current can be smaller. On the other hand, if the sample is very thin and relatively transparent to the electron beam we need to increase the beam current. The operating conditions should be optimized for each type of sample.

3.6. Summary

In this chapter, we described the design and fabrication process of METS devices consisting of suspended micro-heaters and thermometers. Our suspended devices provide four electrodes for four-point electrical resistance measurement and through holes beneath the suspended membranes for TEM characterization of the sample being studied. We also present a new technique using electron beam scanning along NWs, so-called spatially-resolved electron beam probing technique, to measure the spatial distribution of thermal resistance along NW samples. This technique also allows us to measure thermal resistance of the contacts between the sample and the platinum electrodes on the islands.

References

1. Drabble, J. R.; and Goldsmid, H. J.; *Thermal Conduction in Semiconductors*, Pergamon Press, New York, 1961.

2. Mirmira, S. R.; and Fletcher, L. S.; "Review of the Thermal Conductivity of Thin Films", *J. Thermophysics Heat Trans.* Vol. 12, pp. 121 – 131, 1998.

3. Cahill, D. G.; "Analysis of Heat Flow in Layered Structures for Time-Domain Thermoreflectance", *Rev. Sci. Instrum*. Vol. 75, pp. 5119 – 5122, 2004.

4. Lu, L.; Yi, W.; and Zhang, D. L.; "3ω Method for Specific Heat and Thermal Conductivity Measurements", *Rev. Sci. Instrum*. Vol. 72, pp. 2996 – 3003, 2001.

5. Cahill, D. G.; "Thermal Conductivity Measurement from 30 to 750 K: The 3ω Method", *Rev. Sci. Instrum.* Vol. 61, pp. 802 – 808, 1990.

6. Shi, L.; Li, D.; Yu, C.; Jang, W.; Kim, D.; Yao, Z.; Kim, P.; and Majumdar, A.; "Measuring Thermal and Thermoelectric Properties of One-Dimensional Nanostructures Using a Microfabricated Device", *J. Heat Trans.* Vol. 125, pp. 881 – 888, 2003.

7. Hippalgaonkar, K.; Huang, B.; Chen, R.; Sawyer, K.; Ercius, P.; and Majumdar, A.; "Fabrication of Microdevices with Integrated Nanowires for Investigating Low-Dimensional Phonon Transport", *Nano Lett.* Vol. 10, pp. 4341 – 4348, 2010.

8. Volkel, B.; Golzhauser, A.; Muller, H. U.; David, C.; and Grunze, M.; "Influence of Secondary Electrons in Proximal Probe Lithography", *J. Vac. Sci. Technol. B* Vol. 15(6), pp. 2877 – 2881, 1997.

9. Leamy, H. J.; "Charge Collection Scanning Electron Microscopy", *J. Appl. Phys*. Vol. 53 (6), pp. R51 – R80, 1982.

10. Eichler, H.; Salje, G.; and Stahl, H.; "Thermal Diffusion Measurements Using Spatially Periodic Temperature Distributions Induced by Laser Light", *J. Appl. Phys*. Vol. 44, pp. 5383 – 5388, 1973.

11. Xu, X. D.; Zhang, S. Y.; and Kuo, P. K.; "Application of an Optical Birefringence Interferometer to Photothermal Detection for Characterizing Thermal Diffusivities", *Rev. Sci. Instrum.* Vol. 74, pp. 639 – 641, 2003.

12. Blonskij. I. V.; Tkhoryk, V. A.; and Sendeleva, M. L.; "Thermal Diffusivity of Solids Determination by Photoacoustic Piezoelectric Technique", *J. Appl. Phys.* Vol. 79 (7), pp. 3512 – 3516, 1996.

13. Sun, L.; Zhang, S. Y.; Zhao, Y. Z.; Li, Z. Q.; and Cheng, L.P.; "Thermal Diffusivity of Composites Determined by Photoacoustic Piezoelectric Technique", *Rev. Sci. Instrum.* Vol. 74, pp. 834 – 836, 2003.

14. Gao, C. M.; Zhang, S. Y.; Zhang, Z. N.; Shui, X. J.; and Jiang, T.; “Thermal Properties of Materials Characterized by Scanning Electron-Acoustic Microscopy”, *Chin. Phys. Lett.* Vol. 22, pp.2309 – 2312, 2005.

Chapter 4: Temperature and Diameter Dependence of Thermal Transport Properties in Single Crystalline ZnO nanowires

4.1. Introduction

Zinc oxide (ZnO) is a wide and direct band gap (3.5 eV at room temperature) oxide semiconductor [1]. It has attracted a lot of research interest because of its optoelectronic and electronic properties [2, 3]. In particular, ZnO nanowires (NWs) with optical and electrical properties sometimes unattainable in bulk material have shown promise for various applications. Devices constructed from such NWs include piezoelectric power generators [4, 5], field effect transistors [6, 7], ultraviolet photodetectors [8], Shottky diodes [9], switches [10], piezoelectric sensors [11], and logic circuits [12]. Knowledge about the thermal properties of the ZnO NWs in these devices is valuable but not experimentally available so far. The thermal conductivity of ZnO NWs has been theoretically predicted to be one order of magnitude lower than corresponding bulk values due to surface scattering of phonons [13, 14]. However, there has been no reported experimental work on thermal measurements carried out on ZnO NWs.

In this chapter, we present experimental results of the thermal transport properties for individual single crystal ZnO NWs obtained using our METS device. Measurements of NWs with diameter in the range from 50 nm to 210 nm were performed from 77 K to 400 K. Callaway's model [15] is exploited to analyse and explain the temperature dependence of thermal conductivity of ZnO NWs. The effects of a coating of amorphous carbon on the NW and defects induced by Ga ion beam

irradiation on the thermal transport were also investigated.

4.2. ZnO NWs synthesis and characterization

The ZnO NWs used in this study were synthesized via a vapor phase transport (VPT) process (Appendix A). As-grown ZnO NWs were transferred to a copper (Cu) grid by drop-cast method for structural characterization in TEM. The NWs were dispersed in ethanol by sonication and a small amount of the mixture was dropped on to a Cu grid followed by blow drying. The low magnification TEM image of several grown NWs is shown in Figure 4.1a. The NW diameters range from 50 nm to several hundred nanometers. The TEM images also show that the diameter of an individual NW is uniform and does not vary significantly along the wire's length. Calibration of NW diameters observed in the SEM against those determined from TEM images show that measured values are similar, with deviations of typically ± 2.5 nm.

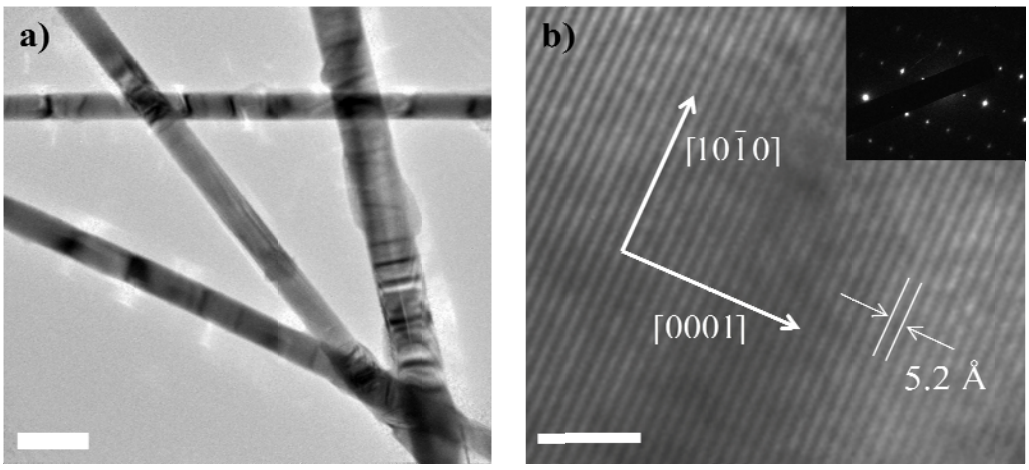

Figure 4.1: (a) TEM image of several VPT-grown ZnO NWs (scale bar: 200 nm), and (b) High resolution TEM (HRTEM) image of NW and the selected-area electron diffraction (SAED) pattern (inset) (scale bar: 2 nm).

The high resolution TEM (HRTEM) image in Figure 4.1b clearly reveals a well-resolved lattice with a measured inter-plane spacing of ≈ 0.52 nm. Moreover, the NW growth direction, determined from both the HRTEM image and the selective-area electron diffraction (SAED) pattern (inset), is along the [0001] direction, which is the fastest growth direction for ZnO crystals. The results show that our ZnO NWs have a single-crystalline wurtzite structure with *c*-axis orientation.

4.3. Temperature and Diameter dependence of thermal transport in single-crystalline ZnO NWs

For thermal conductance measurement, individual as-grown ZnO NWs were picked up and placed onto the METS devices followed by deposition of Pt-C composite films at two ends of the NWs for thermal contact enhancement (Figure 4.2a). The NWs then underwent a surface a-C contamination cleaning process, as previously described in Section 3.3. The cleaned samples with diameter of 51 nm, 120 nm and 209 nm are shown Figure 4.2b.

One important feature of our measurement approach is that we can directly examine the micro-structure of the same NW under study to determine its diameter, surface roughness and contamination, crystalline orientation, and defects. Figure 4.2c shows a low-magnification TEM image of a METS device with an individual ZnO NW. The surface of the NW is seen to be free from an amorphous layer and is naturally rough with root mean square (rms) value of ~1.0 nm (Figure 4.2d). Some of the NWs had broken just before TEM observation after the thermal measurement and for these samples the diameters were determined from earlier SEM images (FEI Nova NanoSEM 230) with an uncertainty of ± 2.5 nm, as discussed above.

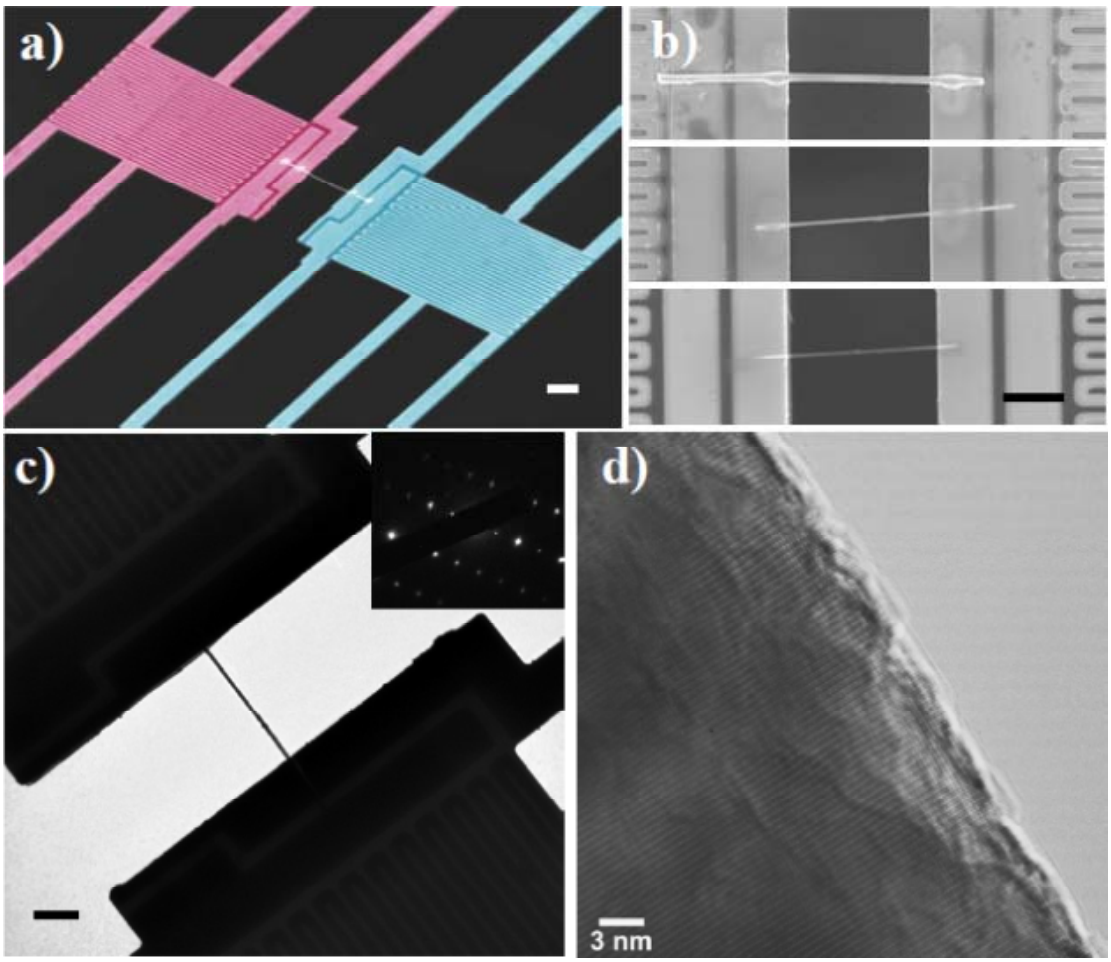

Figure 4.2: (a) SEM image a METS device with an individual ZnO NW bonded onto the heater (red) and the sensor (blue). (b) SEM images of three ZnO NWs with different diameters measured in this study. (c) Low-magnification TEM image of a METS device with an individual ZnO NW (Inset: its SAED pattern). (d) High resolution TEM image of the ZnO NW on METS device. The scale bars shown in (a-c) are 2 μm.

A second important feature of our measurement approach is that we have used a non-contact spatially-resolved electron beam probing technique in combination with the METS device to measure the contact thermal resistance. As described in Chapter 3, a focused electron beam of the SEM was used to induce localized heating along the sample. By scanning the electron beam from the heater to the NW, and recording the corresponding temperature rises of both membrane-islands, the cumulative thermal resistance R_i from the electron beam heating position to the heater can be spatially

resolved. Figure 4.3 shows R_i as a function of position. As the electron beam scans from the contact area to the NW, the value of R_i increases very slowly across the contact, indicating a very low thermal contact resistance. It then increases linearly with a much steeper slope when the e-beam scans along the fully suspended part of the NW. The linear dependence of thermal resistance with length suggests that thermal transport in ZnO NW is purely diffusive, in contrast to ballistic or super-diffusive transport. From the slope of the corresponding part of the profile, the intrinsic thermal resistance of the NW can be calculated. Measurements of the thermal contact resistance of many samples bonded with Pt-C composite show that the thermal contact resistance is negligible compared to the total measured thermal resistance.

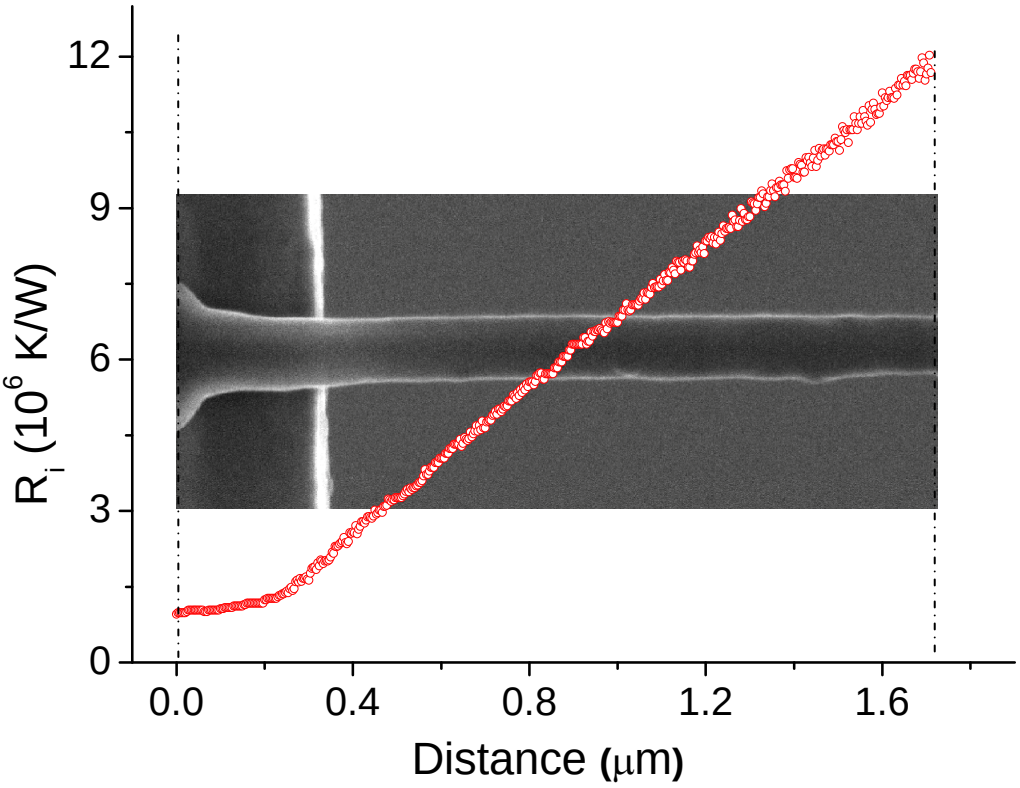

Figure 4.3: Thermal resistance profile scanned along NW crossing the contact. R_i is the cumulative thermal resistance from the heater to the electron beam spot.

However, an intercept of ~1x10^6 W/K is observed at the starting point of the resistance profile. This intercept represents the distributed internal thermal resistance from the heater to the contact point due to the finite thermal conductance of the SiN_x membrane substrate. For further understanding of the internal thermal resistance in the heater and sensor, we employed finite element modeling to simulate the temperature distribution in the sensor. Figure 4.4a shows the simulated temperature distribution on the sensor platform (25 μm × 15 μm) for a 10 K temperature rise on the left-hand-side electrode. The dimensions of the six supporting beams of the actual device are 400 μm long, 2 μm wide, and 300nm thick. However, in the model, the beam length was scaled down to 8 μm with the thermal resistance of the beam kept the same by rescaling the thermal conductivity of the beams. The temperature profile along the dash-dotted line is shown in Figure 4.4b. The temperature change at the electrodes in contact with the sample was determined to be ~3.5% higher for the sensing membrane or 2.0 to 4.0% lower for the heating membrane, depending on the sample thermal conductance, than that measured by the sensor (heater) resistance thermometers. This systematic error in T_h and T_s was compensated in all subsequent calculations. The value of the distributed internal thermal resistance is relatively small and has been neglected previously, but it can introduce significant measurement error, especially for short/thick NWs with low thermal resistance. For example, the intrinsic thermal resistance of a 1-μm segment of the ZnO NW shown in Figure 4.3 is ~7 x 10^6 K/W. Taking into account the distributed internal thermal resistances of both the heater and the sensor, the measured value of the 1-μm ZnO NW (~9 x 10^6 K/W) would give rise to an overestimation of ~22%, which is a significant error if not accounted for. We have made all the samples sufficiently long (~5.0 μm) so that the intrinsic thermal resistance is dominant in the measured value (> 90%). Moreover, the

internal thermal resistances of the heater and the sensor have been compensated for the measured temperature changes in the subsequent thermal conductance calculations, further improving the accuracy of the measured data. The formula for thermal conductance of the sample taking into account the un-uniformed temperature distribution in heating and sensing membrane-islands is given by

$$G_{samp} = \frac{\Delta T_s^{'}}{\Delta T_h^{'} - \Delta T_s^{'}} G_b \tag{4.1}$$

where $\Delta T_h' = \Delta T_h - 0.03\Delta T_h$ and $\Delta T_s' = \Delta T_s + 0.03\Delta T_s$ are the temperature changes in the heating and the sensing membrane-islands after compensation, respectively.

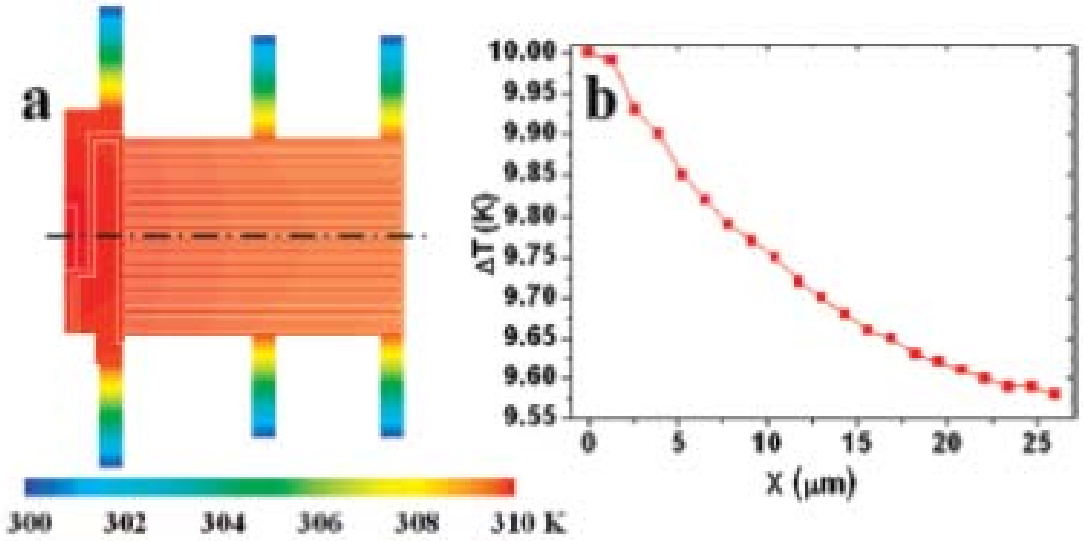

Figure 4.4: (a) Finite element simulation of the temperature distribution on the sensor platform for a 10 K temperature rise on the left-hand-side electrode. The sensor membrane is 25 μm × 15 μm. Each of the six supporting beams of the actual device is 400 μm long and 2 μm wide. In the model, the beam length was scaled down to 8 μm with the thermal resistance of the beam kept the same by rescaling the thermal conductivity of the beams. (b) Temperature profile along the dash-dotted line in (a).

In order to study the temperature and size dependence of thermal conductivity of ZnO NWs, five samples with different diameter and length were prepared on 5 μm gap METS devices. The diameter and length of each NW sample (Table 4.1) were determined by SEM after the wires had been placed on the METS devices. For thermal conductivity calculation, the length of NWs is determined between two contact points on the heating side and sensing side electrodes. As mentioned above, the diameter measured by SEM is only less than ± 2.5 nm different from that measured by TEM. The error is less than 4% for the smallest NW with diameter of 70 nm, which gives reasonably accurate results for the calculated thermal conductivity.

Table 4.1: Dimensions of ZnO NW samples in this study

Sample #	Diameter (nm)	Length (μm)
1	70	4.94
2	84	5.12
3	120	5.07
4	166	5.10
5	209	5.00

The thermal conductivity was measured from 77 K to 400 K (Figure 4.5). For all the samples, as the temperature increases, the thermal conductivity first increases to a maximum then decreases. Compared to the thermal conductivity of bulk single-crystalline ZnO (inset of Figure 4.5a), there are two important features that are common to all the NWs we measured:

(i) The measured thermal conductivities are dramatically lower by more than one

order of magnitude compared to that of bulk ZnO (~100 W/m.K at 300 K) [16]. Moreover, with decreasing diameter, the thermal conductivity is correspondingly smaller over the entire measured temperature range. This clearly indicates that enhanced phonon boundary scattering exerts a strong suppression effect on phonon transport in ZnO NWs. In normal bulk crystal, boundary scattering is important only at very low temperatures (typically below ~30 K) due to the scattering of long wavelength phonons. In contrast, the reduction of thermal conductivity was observed for the NWs over the entire experimental temperature range, suggesting that boundary scattering is also significant even at high temperatures.

(ii) All the NWs show a maximum of thermal conductivity between 120 K and 150 K, which is much higher than the corresponding temperature for bulk ZnO (30-35 K) [16]. The shift of the peak suggests that boundary scattering is dominant until 120 K, and Umklapp scattering, which reduces the thermal conductivity with temperature, becomes important and comes to dominate over the boundary scattering at the higher temperatures (> 150 K).

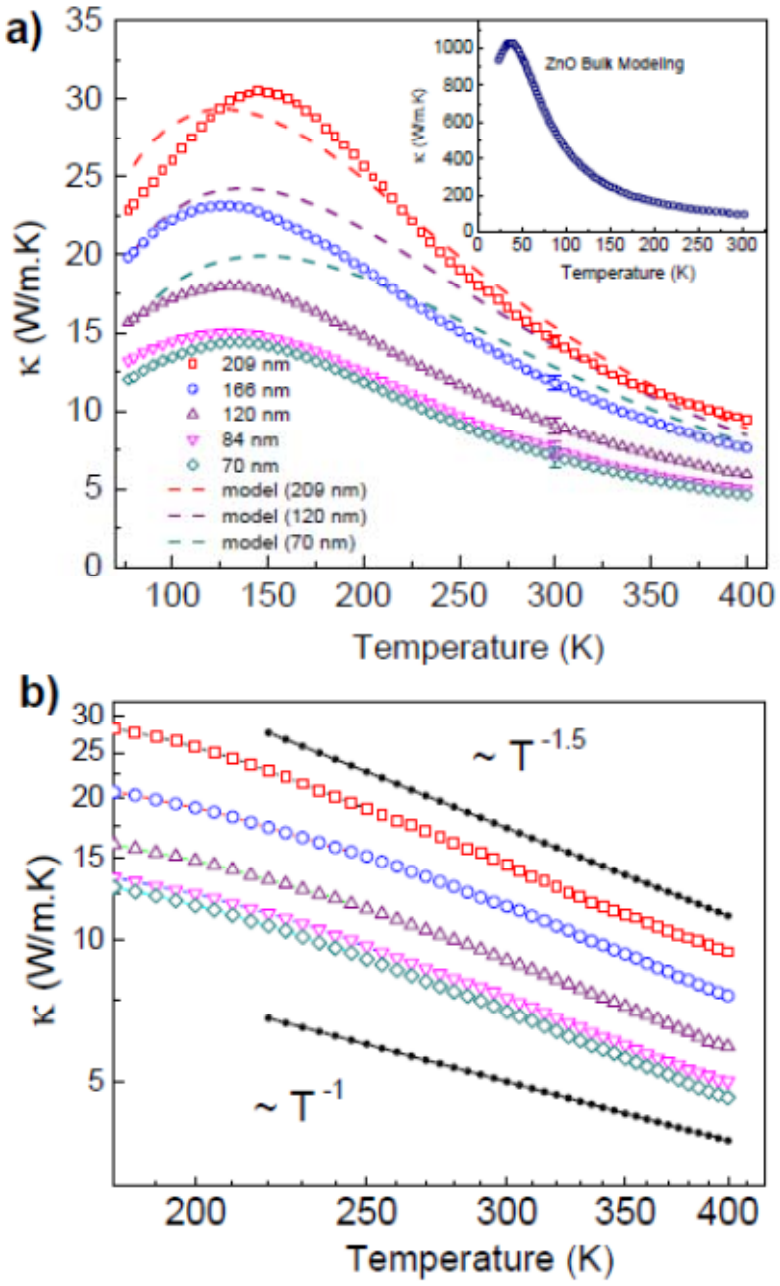

Figure 4.5: (a) Temperature dependence of thermal conductivity of the ZnO NWs with different diameters. Inset shows the thermal conductivity of bulk ZnO from modeling [16]. (b) Log-log scale in temperature range from 160K to 400K, showing $\kappa \sim T^{-\alpha}$ with α in the range of 1.42 – 1.49; the two curves $\sim T^{-1.5}$ and $\sim T^{-1}$ are shown to guide the eyes.

The dramatic reduction in thermal conductivity with increase of diameter and the shift of the peak to higher temperature have also been observed for Si NWs [17-19]. However, the thermal conductivity of ZnO NWs decreases very rapidly beyond

the peak with temperature as $T^{-\alpha}$ (α is in the range of 1.42 to 1.49) (Figure 4.5b). This is in sharp contrast to the temperature dependence observed for Si NWs of similar diameters which shows only a slight decline in thermal conductivity beyond the peak [17-19]. For bulk pure single crystal, the thermal conductivity varies with temperature as T^{-1} where the main scattering mechanism is Umklapp scattering. The falloff sharper than T^{-1} suggests that, besides the boundary scattering and Umklapp scattering, some other scattering mechanisms must also play important roles. From TEM observation, the NWs are single crystalline without observable bulk defects, grain boundaries, or dislocations. Thus phonon scattering by such defects is unlikely. In addition, four-point electrical measurements were also conducted on some samples, which showed that the electrical resistances of the NWs are typically larger than 1 MΩ, which allows us to neglect charge-carrier contributions to thermal transport.

The micro-photoluminescence (MicroPL) spectrum of an individual ZnO NW shows a broad visible emission band centred at 540 nm due to deep-level recombination, indicating intrinsic point defects (oxygen vacancies or Zn interstitials) are present in the ZnO NWs (see Figure 4.6). Furthermore, for ZnO, the natural abundance Zn comprises three isotopes (48.6% ^{64}Zn, 27.9% ^{66}Zn and 18.8% ^{68}Zn, mass variance: 5.68×10^{-4}), and natural abundance O is 99.8% ^{16}O. The large isotopic disorder can affect the thermal conductivity dramatically [20].

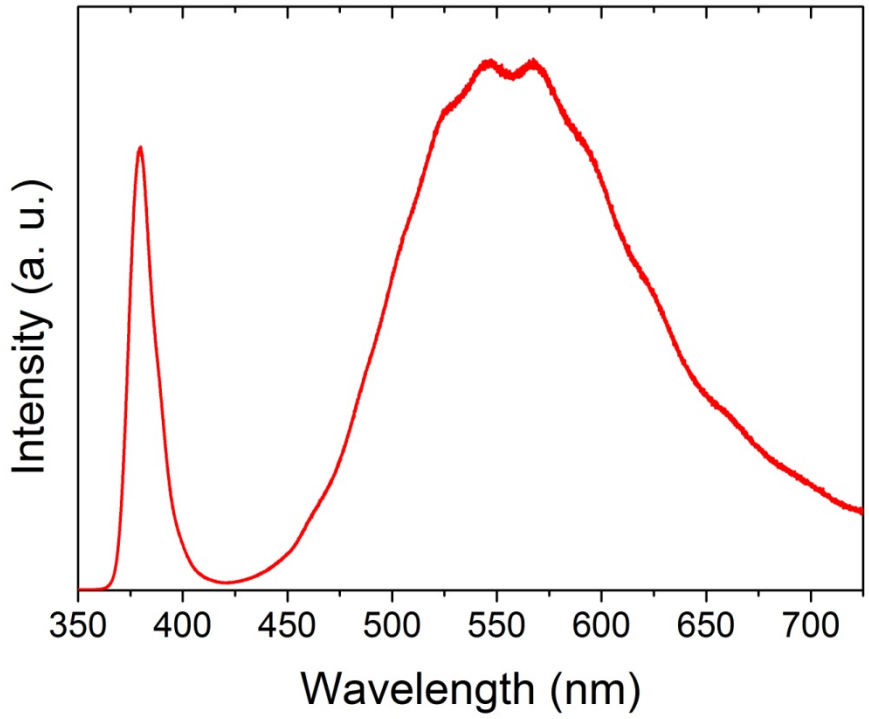

Figure 4.6: Micro-Photoluminescence (MicroPL) spectrum of an individual ZnO NW lying on a SiO_2/Si substrate after dispersion in ethanol and drop-casting. The spectrum was obtained with a Renishaw inVia Raman Microscope. The excitation source is a He-Cd UV laser at 325 nm with a power of 20 mW, and it was focused by a 40X UV lens to a spot size of 2 μm. The excitation spot is chosen at the middle section along the length of the NW. It can be seen that the ZnO NW exhibits UV emission at ~385 nm due to near-band-edge recombination, and a broad band centered at ~540 nm in the visible region. In general, it is believed that the visible emission originates from the transition in the defect states associated with impurities or point defects such as oxygen vacancies and Zn interstitials.

In contrast, Si (92.23% ^{28}Si, 4.67% ^{29}Si, and 3.1% ^{30}Si) has much less isotopic disorder (mass variance: 2.02×10^{-4}). The significantly larger isotopic disorder together with the presence of point defects (oxygen vacancies or Zn interstitials) might be the major reasons for the sharper falloff of the thermal conductivity at intermediate and high temperatures. Interestingly, Callaway had predicted that beyond the peak the thermal conductivity in the presence of isotope scattering is proportional to $T^{-1.5}$ [15].

Our measurement data are similar to Callaway's prediction.

To achieve a more quantitative understanding of the temperature and size dependent thermal transport of ZnO NWs, we used a conventional Callaway model to analyze the experimental data. The thermal conductivity of the lattice structures taking account into the effect of phonon boundary scattering is shown as follows [14]:

$$\kappa = \frac{k_B}{2\pi^2 v}\left(\frac{k_B T}{\hbar}\right)^3 \int_0^{\theta_D} \frac{x^4 e^x (e^x - 1)^{-2}}{AT^4 + (B_1 + B_2)T^5 x^2 + v/L}\, dx \qquad (4.2)$$

where T is absolute temperature, θ_D is Debye temperature (399.5 K for ZnO) [16], v is the average sound velocity of phonon (3845 m/s in bulk ZnO), L is the characteristic length of material, ω is circular frequency, k_B is the Boltzmann constant and $\hbar$ is the reduced Planck constant. In this equation, three scattering process are considered as expressed by three terms in the denominator: (i) impurity scattering, including isotope scattering, in which relaxation time is proportional to ω^{-4}, which is independent of temperature, (ii) three-phonon normal scattering and Umklapp scattering, in which relaxation time is proportional to $(\omega^2 T^3)^{-1}$, and (iii) boundary scattering, described by a constant relaxation time L/v based on the Casimir model [21]. In the present study, L would be represented by the diameter (d) of the NWs. We used the thermal conductivity of the NW with largest diameter (L = 209 nm) to adjust the phonon scattering parameters, and A and B_1+B_2 were numerically optimized as 83.93 $K^{-4}s^{-1}$ and 0.235 $K^{-5}s^{-1}$, respectively. Then L was varied based on the measured values, while the other parameters were fixed. It can be seen from Figure 4.5a (dashed lines) that the fitting results obtained from varying L do not match the thermal conductivities for different diameters. Attempts were also made to use different forms of Umklapp scattering, which also yielded results that do not agree well with the experimental data. The largest discrepancy between experimental data and the conventional phonon

transport model is that the measured thermal conductivity decreases much more rapidly with diameter than the conventional model, especially at high temperature. This suggests that the conventional phonon boundary scattering model based on the Casimir limit [21], which assumes that boundary scattering is frequency independent and temperature independent, cannot account well for the diameter dependent thermal transport properties of ZnO NWs. Large discrepancies between experimental data and the conventional phonon transport model have also been observed for Si NWs [18, 19]. In the light of the systematic experimental data for Si NWs, several theoretical approaches have been proposed [19, 22]. For example, Chen *et al*. have suggested that phonon-boundary scattering is highly frequency dependent, and ranges from nearly ballistic to completely diffusive, which can explain the temperature dependence observed for thin Si NWs [19]. Mingo has put forward a "complete phonon dispersions" approach to account for both temperature dependence and diameter dependence of Si NWs [22]. However, currently there is no exact theoretical model for ZnO NWs below 400 K. The thermal conductivity as a function of d^2 is plotted in Figure 4.7. Strikingly, it can be seen that the thermal conductivity scales approximately linearly with the cross-sectional area ($\sim d^2$) of the NWs in the measured diameter range at both low temperature (80 K) and room temperature (300 K). Moreover, the thermal conductivity increases more rapidly with diameter at 80 K than at 300 K. This can be understood because phonon-boundary scattering in limiting phonon mean free path is much more dominant at lower temperatures due to longer phonon mean free path.

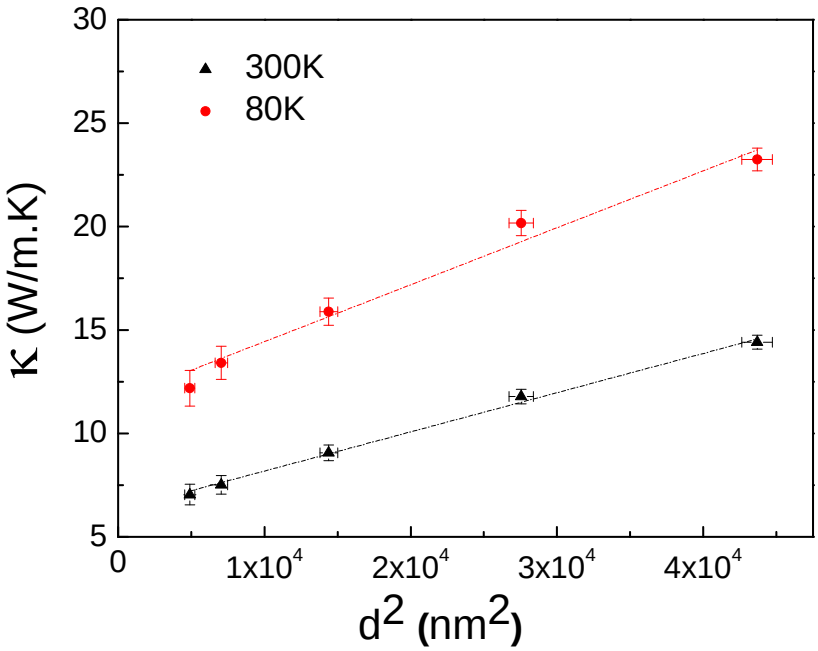

Figure 4.7: Diameter dependence of thermal conductivity of the ZnO NWs at 80 K and 300 K. The thermal conductivity approximately increases linearly with cross-section area ($\sim d^2$) in the measured diameter range. The dash-dot lines are shown to guide the eyes.

4.4. Effect of surface coating by thin amorphous carbon

As previously mentioned, during the pick-and-place and bonding processes, a-C layers were inevitably coated on the surface of the ZnO NWs by EBID of hydrocarbon residues from the SEM chamber forming core/shell structured NWs. Recently, the effects of a-C shells on the electrical characteristics of ZnO/a-C core/shell structured NWs were reported [23]. The ZnO/a-C core/shell structured NWs synthesized by coating a-C shells on the ZnO NW cores using the plasma-enhanced chemical vapor deposition (PECVD) were used as field effect transistor (FET) channels for comprehensive studies of electrical transport properties. The electrical properties of the ten ZnO NWs FETs with and without an a-C shell were investigated. In most case, the carrier mobility of the ZnO/a-C core/shell structured

NW FETs (25 – 200 $cm^2 V^{-1} s^{-1}$) was better than that of ZnO NW FETs without an a-C shell (9 – 70 $cm^2 V^{-1} s^{-1}$). The effects of a-C on thermal transport properties of core/shell structured NWs also have recently attracted much attention. Theoretical simulations have shown that the presence of a thin layer of amorphous coating can strongly modify the thermal properties of the NW cores which are usually very small (few nanometers in diameter) [24 – 27]. However, the NWs in practical applications normally have diameters from a few tens of nanometers to a few hundred nanometers for which the effect of surface coating on thermal transport properties is still unclear.

In order to elucidate the effect of surface coating on the thermal transport properties of ZnO NWs, we have intentionally coated an a-C layer onto the NW surface using EBID after the thermal conductance measurement on the pristine NWs. The ZnO NWs were intentionally exposed to electron-beam for a prolonged period (~5-10 min). A thin layer of a-C shell was coated surrounding the surface of the NWs by EBID from hydrocarbon residues in the SEM chamber. The schematic of the coating process and a typical TEM image of a ZnO NW with a-C shell are shown in Figure 4.8a and Figure 4.8b. The thickness of a-C shell is typically ~5-10 nm for all samples, depending on the exposure time. Figure 4.8c shows the thermal conductance as a function of temperature for the ZnO NW before (d~84 nm) and after coating with an a-C shell (d~102 nm) (see SEM image in Figure 4.8c). After the a-C shell coating, the thermal conductance shows only a slight increase, while the shape of the curve follows the same trend as the one without the a-C shell. A repeat of the thermal conductance measurement was also carried out after the carbon contamination has been cleaned using RF plasma cleaning, which recovers the curve of the pristine NW. Based on the difference of the thermal conductance and the thickness of the shell measured in TEM, we extracted the thermal conductivity of a-C (< 0.8 W/m.K, inset

of Figure 4.8c), which is in good agreement with the values reported previously [28]. Similar results were obtained for all the other ZnO NWs with different diameters. These observations suggest that the a-C shell generally acts as an independent parallel thermal path alongside the ZnO NWs, and does not introduce detectable perturbation to the thermal transport of the NW cores. Thus for practical devices where the NWs are generally supported on amorphous dielectrics or polymers, the presence of the substrate should not adversely affect their thermal conductivity. However, when the NW diameter shrinks down to the range where phonon confinement occurs, the effect of the surface layer and substrate will become important, as predicted by theoretical atomistic simulations [24 – 27].

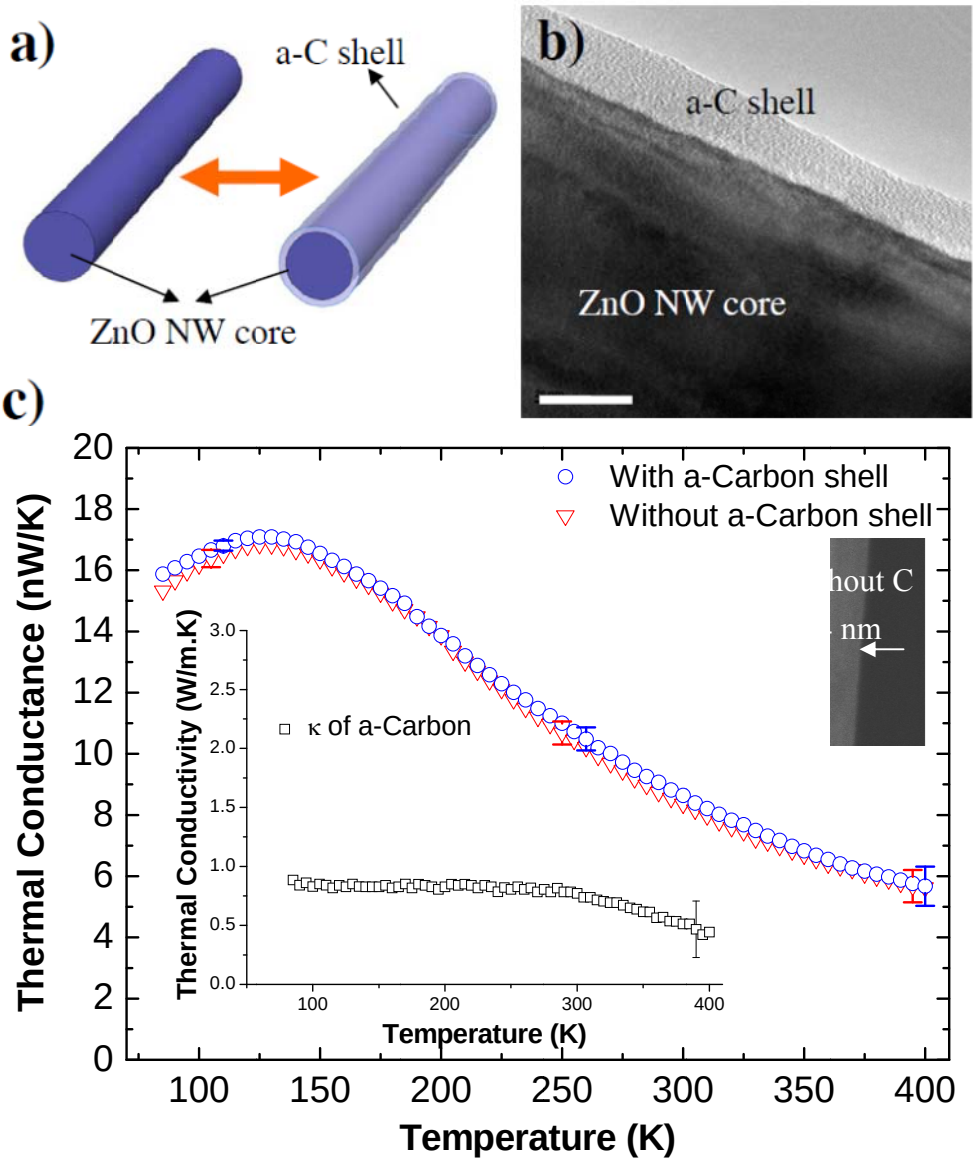

Figure 4.8: (a) Sketch of a ZnO NW coated with and without a-C shell. (b) TEM image of a ZnO NW core coated with a-C shell; scale bar: 20 nm. (c) Thermal conductance measurement of a ZnO NW with and without a-C shell. Inset 1 (top-right): SEM images of the ZnO NW with and without a-C shell; inset 2 (bottom-left): Extracted thermal conductivity of a-C.

4.5. Effect of defects induced by focused Ga ion beam irradiation

We have further studied the effect of ion-irradiation induced defects on the thermal transport of ZnO NWs. Another set of ZnO NW samples with diameters of 51 nm, 90 nm, and 126 nm were prepared on 5 μm gap METS devices (Table 4.2). In this experiment, both ends of NW sample were bonded to electrodes by small Pt strips using FIBID using a 30 keV Ga^+ ion beam and beam current of 10 pA.

Table 4.2: Details of ZnO NWs' dimension used in this experiment

Sample #	Diameter (nm)	Length (μm)
6	51	5.07
7	90	5.12
8	126	5.00

During inspection of the devices, the NWs were inevitably exposed to the ion irradiation. Precautions were taken to keep the ion dose on the suspended part of the NWs as low as possible ($< 10^{14}$ cm^{-2}). TEM images shows that even a slight exposure can cause significant damage to the ZnO lattice. As shown in the inset of Figure 4.9a and Figure 4.9b, after ion irradiation, the surface was significantly roughened, and the crystalline lattice of ZnO near the surface was partially transformed into an amorphous structure. Additional defects, such as vacancies, interstitials and Ga impurities, were also produced in the ZnO NW under ion irradiation. SAED patterns confirmed that the NW remains single crystalline (inset, Figure 4.9b). Note that a ~5 nm layer of a-C shell was pre-coated surrounding the NW during the bonding process. Compared with the non-irradiated samples of similar diameters, the thermal conductivities of the irradiated samples all show a notable reduction, especially in the

lower temperature range (Figure 4.9a). A key feature caused by ion irradiation is that the temperature dependence curves are substantially flattened and the peaks are shifted to higher temperatures. The reason can be attributed to enhanced defect scattering which comes to dominate at intermediate temperature, as the intermediate frequency phonons are most efficiently scattered by the defects. This phenomenon is most serious for the thinnest NW which shows an almost flat curve over a wide temperature range. As focused-ion beam is often used to deposit and create metallic contacts to nano-devices, precautions should be taken to keep the active region away from the ion exposure as it may result in significant degradation of its transport properties.

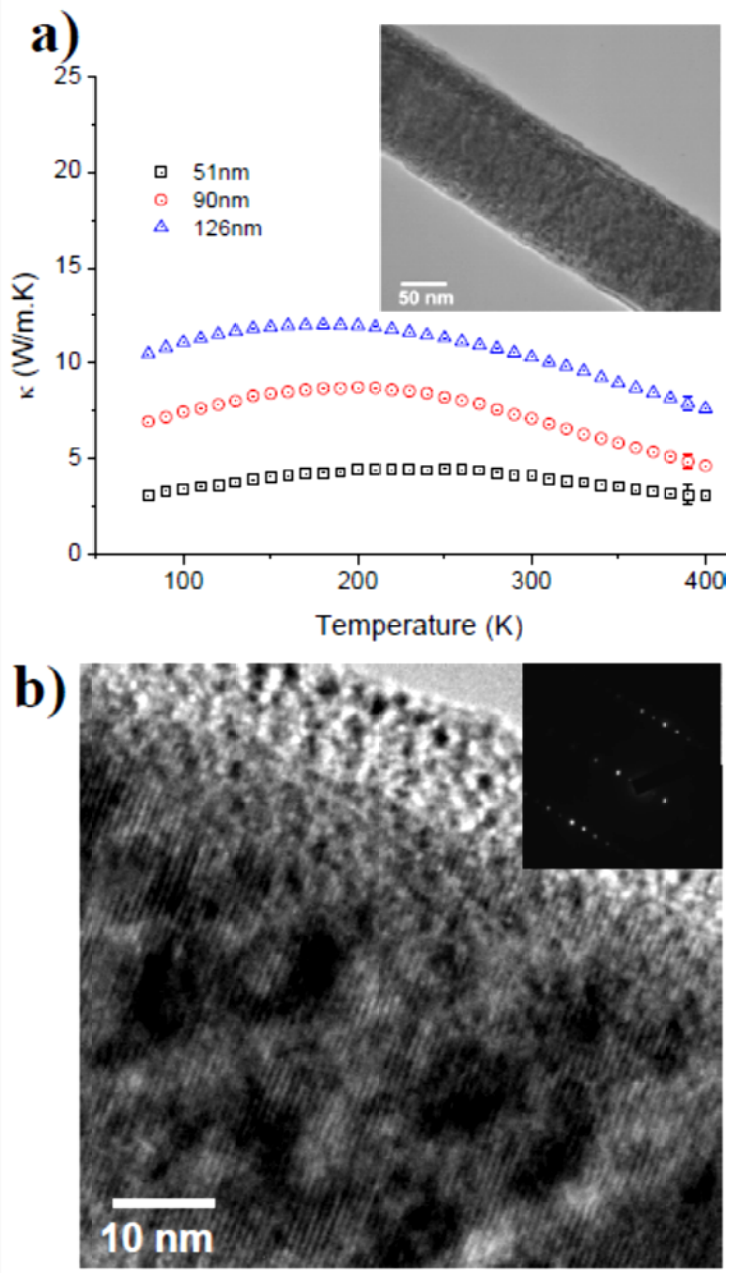

Figure 4.9: (a) Temperature dependence of thermal conductivity of ion-irradiated ZnO NWs with different diameters. Inset: Low-magnification TEM image of an ion-irradiated ZnO NW. (b) High-resolution TEM image of an ion-irradiated ZnO NW. Inset: its SAED pattern.

4.6. Summary

In this chapter we have systematically studied the diameter-dependent thermal conductivity of ZnO NWs in the temperature range from 77 K to 400 K using the METS devices. It is found that the thermal conductivity is significantly lower due to enhanced phonon boundary scattering, and the reduction is much stronger than predicted by the conventional phonon transport model based on the Casimir model. An empirical relationship for assessing diameter-dependent thermal properties is presented, which shows an approximately linear dependence of the thermal conductivity on the cross-section area ($\sim d^2$) of the NWs in the measured diameter range. Temperature dependent measurements show that beyond the low-temperature maximum, the thermal conductivity decreases with temperature as $T^{-\alpha}$ (α in the range of 1.42 – 1.49), indicating strong impurity scattering and Umklapp scattering at intermediate and high temperatures. Furthermore, the thermal transport properties of the ZnO NWs are found to be insensitive to the surface a-C contamination, while it can be greatly degraded by ion irradiation at even low dose.

References

1. Ozguz, U.; Alivov, Y. I.; Liu, C.; Teke, A.; Reshchikov, M. A.; Dogan, S.; Avrutin, V.; Cho, S. J.; and Morkoc, H.; "A Comprehensive Review of ZnO Materials and Device", *J. Appl. Phys.* Vol. 98, 041301, 2005.

2. Tang, Z. K.; Wong, G. K. L.; Yu, P.; Kawasaki, M.; Ohtomo, A.; Koinuma, H.; and Segawa, Y.; "Room-Temperature Ultraviolet Laser Emission from Self-Assembled ZnO Micro Crystallite Thin Films*", Appl. Phys. Lett.* Vol. 72, pp. 3270 – 3272, 1998.

3. Tsukazaki, A.; Ohtomo, A.; Onuma, T.; Ohtani, M.; Makino, T.; Sumiya, M.; Ohtani, K.; Chichibu, S. F.; Fuke, S.; Segawa, Y.; Ohno, H.; Koinuma, H.; and Kawasaki, M.; "Repeated Temperature Modulation Epitaxy for p-type Doping and Light-Emitting Diode Based on ZnO", *Nat. Mater.* Vol. 4, pp. 42 – 46, 2005.

4. Wang, Z. L.; and Song, J.; "Piezoelectric Nanogenerators Based on Zinc Oxide Nanowire Arrays", *Science* Vol. 312, pp. 242 – 246, 2006.

5. Wang, X.; Song, J.; and Wang, Z. L.; "Direct-Current Nanogenerator Driven by Ultrasonic Waves", *Science* Vol. 316, pp. 102 – 105, 2007.

6. Goldberger, J.; Sirbuly, D. J.; Law, M.; and Yang, P.; "ZnO Nanowire Transistors", *J. Phys. Chem. B* Vol. 109, pp. 9 – 14, 2005.

7. Wang, X.; Zhou, J.; Song, J.; Liu, J.; Xu, N.; and Wang, Z. L.; "Piezoelectric Field Effect Transistor and Nanoforce Sensor Based on a Single ZnO Nanowire", *Nano Lett.* Vol. 6, pp. 2768 – 2772, 2006.

8. Kind, H.; Yan, H.; Messer, B.; Law, M.; and Yang, P.; "Nanowire Ultraviolet Photodetectors and Optical Switches", *Adv. Mater.* Vol. 14, pp. 158 – 160, 2002.

9. Heo, Y. W.; Tien, L. C.; Norton, D. P.; Pearton, S. J.; Kang, B. S.; Ren, F.; and LaRoche, J. R.; "Pt/ZnO Nanowire Schottky Diodes", *Appl. Phys. Lett.* Vol. 85, pp. 3107 – 3109, 2004.

10. Zhou, J.; Fei, P.; Gu, Y.; Mai, W.; Gao, Y.; Yang, R.; Bao, G.; and Wang, Z. L.; "Piezoelectric-Potential-Controlled Polarity-Reversible Schottky Diodes and Swiches of ZnO Wires", *Nano Lett.* Vol. 8, pp. 3973 – 3977, 2008.

11. Zhou, J.; Gu, Y.; Fei, P.; Mai, W.; Gao, Y.; Yang, R.; Bao, G.; and Wang, Z. L.; "Flexible Piezotronic Strain Sensor", *Nano Lett.* Vol. 8, pp. 3035 – 3040, 2008.

12. Park, W. I.; Kim, J. S.; Yi, G. C.; and Lee, H. J.; "ZnO Nanorod Logic Circuits", *Adv. Mater.* Vol. 17, pp. 1393 – 1397, 2005.

13. Kulkarni, A. J.; and Zhou, M.; "Size-Dependent Thermal Conductivity of Zinc Oxide Nanobelts", *Appl. Phys. Lett*. Vol. 88, 141921, 2006.

14. Kulkarni, A. J.; and Zhou, M.; "Tunable Thermal Response of ZnO Nanowires", *Nanotechnology* Vol. 18, 435706, 2007.

15. Callaway, J.; “Model for Lattice Thermal Conductivity at Low Temperature”, *Phys. Rev.* Vol. 113, pp. 1046 – 1051, 1959.

16. Alvarez-Quintana, J.; Martínez, E.; Pérez-Tijerina,E.; Pérez-García, S. A.; and Rodríguez-Viejo, J.; “Temperature Dependent Thermal Conductivity of Polycrystalline ZnO Films”, *J. Appl. Phys.* Vol. 107, 063713, 2010.

17. Hochbaum, A.; Chen, R.; Delgado, R.; Liang, W.; Garnett, E.; Najarian, M.; Majumdar, A.; and Yang, P.; “Enhanced Thermoelectric Performance of Rough Silicon Nanowires”, *Nature* Vol. 451, pp. 163 – 167, 2008.

18. Li, D.; Wu, Y.; Kim, P.; Shi, L.; Yang, P.; and Majumdar, A.; “Thermal Conductivity of Individual Silicon Nanowires”, *App. Phys. Lett.* Vol. 83, pp. 2934 – 2936, 2003.

19. Chen, R.; Hochbaum, A.; Murphy, P.; Moore, J.; Yang, P.; and Majumdar, A.; “Thermal Conductance of Thin Silicon Nanowires”, *Phys. Rev. Lett.* Vol. 101, 105501, 2008.

20. Yang, N.; Zhang, G.; and Li, B.; “Ultralow Thermal Conductivity of Isotope-Doped Silicon Nanowires”, *Nano Lett.*, Vol. 8, pp. 276 – 280, 2008.

21. Casimir, H. B. G; “Note on The Conduction of Heat in Crystals”, *Physica* Vol. 5, 495, 1938.

22. Mingo, N.; “Calculation of Si Nanowire Thermal Conductivity Using Complete Phonon Dispersion Relations”, *Phys. Rev. B* Vol. 68, 113308, 2003.

23. Ra, H. W.; Choi, D. H.; Kim, S. H.; and Im, Y. H.; “Formation and Characterization of ZnO/a-C Core-Shell Nanowires”, *J. Phys. Chem. C* Vol. 113, pp. 3512 – 3516, 2009.

24. Mingo, N.; and Yang, L.; “Phonon Transport in Nanowires Coated with an Amorphous Material: An Atomistic Green's Function Approach”, *Phys. Rev. B* Vol. 68, 245406, 2003.

25. Donadio, D.; and Galli, G.; “Temperature Dependence of the Thermal Conductivity of Thin Silicon Nanowires”, *Nano Letters* Vol. 10, pp. 847 – 851, 2010.

26. Hu, M.; Giapis, K. P.; Goicochea, J. V.; Zhang, X.; and Poulikakos, D.; “Significant Reduction of Thermal Conductivity in Si/Ge Core-Shell Nanowires”, *Nano Lett.* Vol. 11, pp. 618 – 623, 2011.

27. Chen, J., Zhang, G.; Li, B.; “Reduce Thermal Conductivity by Engineering Phonon Coherent Resonance in Core-Shell Nanowires”, Submitted, 2011.

28. Bullen, A. J.; O'Hara, K. E.; Cahill, D.; Monteiro, O.; von Keudell, A.; “Thermal Conductivity of a-C Thin Films”, *J. Appl. Phys.* Vol. 88, pp. 6317 – 6320, 2000.

Chapter 5: Electrical and Thermal Properties of VO_2 Nanowires

5.1. Introduction

The phenomenon of metal – insulator phase transition in the oxides of transition elements has been attracting much attention in the scientific community because of their interesting electrical and optical properties around the transition point. Among them, the metal – insulator transition (MIT) in vanadium dioxide (VO_2) has been intensively studied for potential applications in Mott field-effect transistors [1, 2], high-speed electronic devices [3], ultrafast optical switches [4], and thermo-chromic devices [5, 6]. VO_2 is well known for its first order MIT from a low-temperature insulating phase to a high-temperature metallic phase near room temperature (340 K), which is accompanied by a structural transition that corresponds to the abrupt change in resistivity [7 – 10]. In a narrow temperature interval of a few degrees around MIT temperature, the electrical conductivity and optical constants of VO_2 change dramatically [11-13]. Recently, single crystalline MIT VO_2 nanowires (NWs) have been the subject of investigation with respect to the thermoelectric effect [14], strain engineering of phase transition [15], and photo-thermoelectric effects in localized photocurrent [16], which opens opportunities in exploiting VO_2 NWs for device and sensor applications. It has been shown that single-crystal VO_2 NWs clamped on a SiO_2 substrate exhibit periodic, alternating metallic-insulating (M-I) domain patterns near the transition temperature due to uniaxial strain imposed by elastic mismatch with the substrate [15, 17, 18]. A study of the resistance behavior of VO_2 NWs lying on SiO_2 substrate shows that many discrete resistance steps occur

over the heating and cooling half cycles instead of an abrupt change from insulating phase to metallic phase as observed in bulk single-crystal VO_2 [17]. On the other hand, suspended single-crystal VO_2 NWs with two ends clamped on fixed electrodes exhibited coexisting M-I phases separated by a single inter-phase wall [19]. The resistance behavior of suspended and end-clamped VO_2 NWs also exhibits some discrete steps during temperature cycling. Although a lot of studies have focused on the effects of strain/stress on phase transition in VO_2 nanostructures, the effects of defects such as oxygen vacancies or vanadium interstitials that may exist in VO_2 wires are unempirical. Furthermore, while many studies have been carried out on the electrical and optical properties of VO_2 NWs, the behavior of the thermal properties of suspended VO_2 NWs has received less attention.

In this chapter, we study the electrical and thermal properties of single-crystalline VO_2 NWs using METS devices. The specific features of our METS devices allow us to perform the thermal – electrical measurement and correlate the electrical and thermal properties of NWs. In particular, we found that the combination of stress and defects (oxygen vacancies and/or vanadium interstitials) induces a new phenomenon in VO_2 NWs.

5.2. Placement of VO_2 NW sample on METS devices

The VO_2 NWs in our study were synthesized using a catalyst-free chemical vapor deposition route (Appendix B). Characterization by SEM and X-ray diffraction (Appendix B) shows that the NWs have a rectangular cross-section with smooth and well faceted side walls. The NWs are highly single-crystalline and preferentially oriented along the [100] direction with monoclinic structure at room temperature. The typical lateral dimension of the VO_2 NWs is in the range of 80 – 500 nm, with lengths ranging from 5 to 30 μm.

To characterize the electrical and thermal properties, individual VO_2 NWs were transferred from the Si substrate on which they were grown to our METS devices using a nano-manipulator in a SEM. Two ends of the NW were bonded onto four Pt electrodes by deposition of Pt-C contact pads using a focused electron beam as discussed in Chapter 3. Figure 5.1 shows an SEM image of 210 nm wide VO_2 NW placed on a 5 μm-gap METS device. The inset of Figure 5.1 is a higher magnification SEM image showing four Pt contacts which allow us to simultaneously conduct four-probe electrical transport measurements alongside thermal transport measurements, based on the method described in chapter 3, thus directly correlating both thermal and electrical properties on the same sample. All the measurements were carried out in vacuum better than 10^{-5} mbar.

In this work, VO_2 NWs with different width were all prepared on 5 μm-gap METS devices. The width and length of each NW were measured from SEM images after the wires had been placed on the devices and cleaned (the cleaning process was discussed in chapter 3). The width of NWs investigated is in the range from 140 nm to 210 nm. Figure 5.2 shows the SEM images of some VO_2 NWs studied in this work.

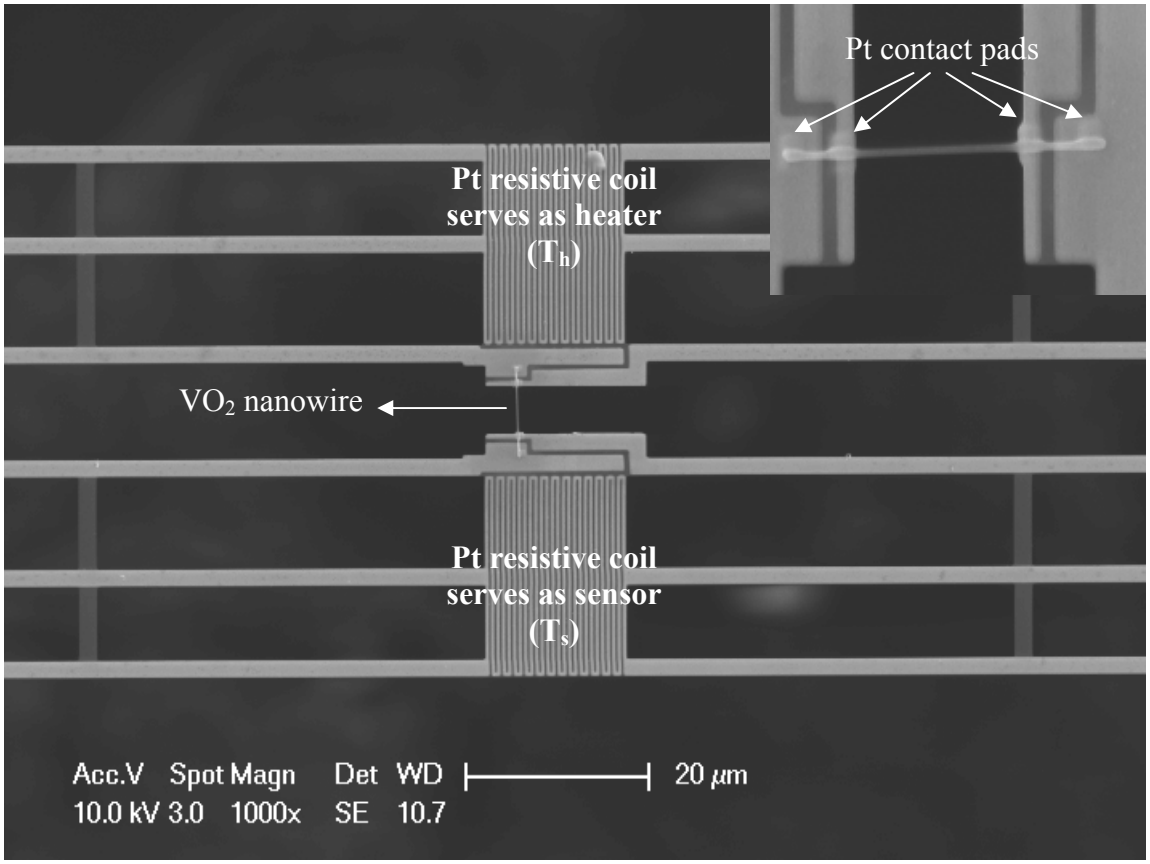

Figure 5.1: SEM image of 210 nm wide VO_2 NW integrated on 5 μm-gap METS device. Inset: A higher magnification SEM image showing four Pt-C contacts – the gap is 5 μm.

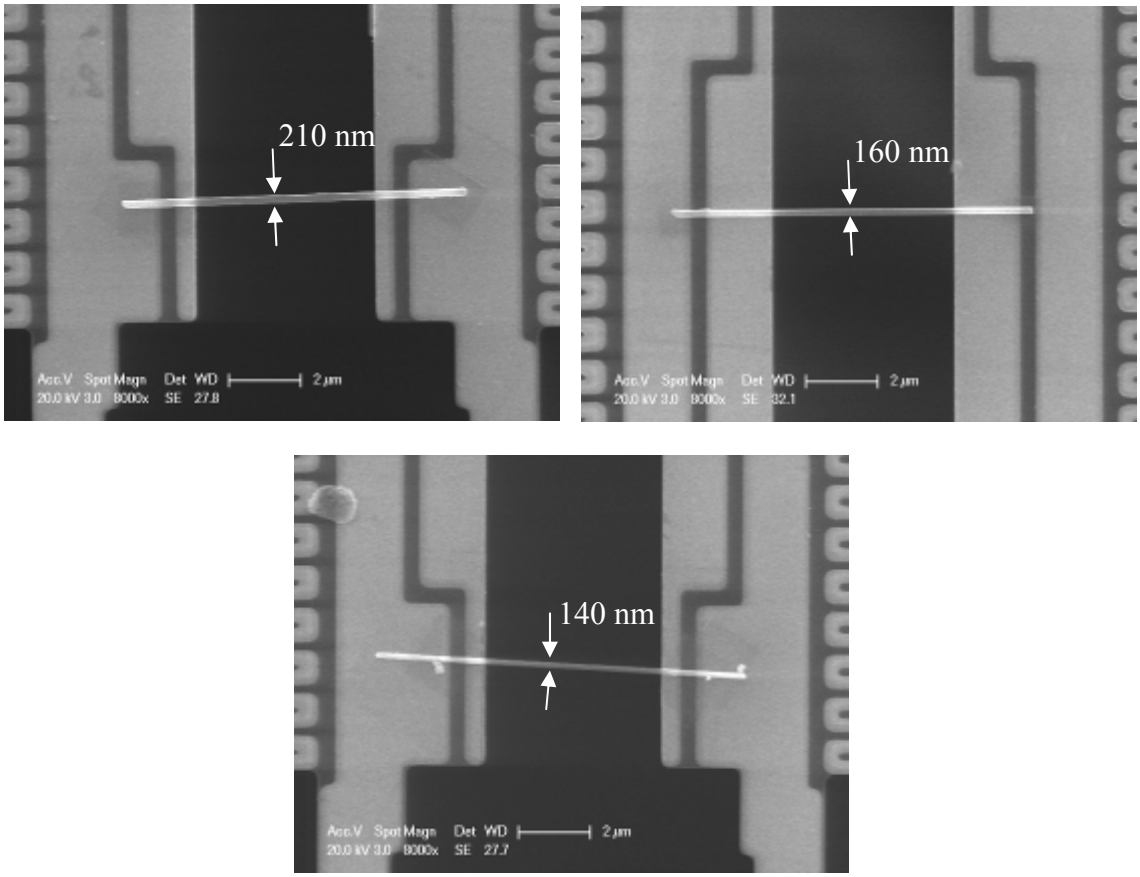

Figure 5.2: SEM images of three of VO_2 NWs on METS devices studied in this work with widths of 210 nm, 160 nm, and 140 nm.

5.3. Electrical properties

The electrical characteristics of the suspended VO_2 NWs in the vicinity of MIT were measured under two heating configurations. In the first configuration, both heater and sensor islands were heated through resistive heating such that their temperatures were the same, and single domain behavior was observed. With the second configuration DC current was only passed through the Pt resistive coil of the heater island (Figure 5.1, top), ramping its temperature (T_h). The temperature in the bottom membrane-island (T_s) was measured using the integrated Pt resistive coil, which serves as the sensor. In this configuration, we observed coexistent M-I domains.

5.3.1. Single domain behavior

The temperatures of both islands upon heating and cooling are shown in Figure 5.3. Since they are identical over the temperature range they are defined as a single global temperature T_{global}. The temperature range can be controlled by the range of DC current passing through Pt resistive coils. In this case, the temperature was swept from room temperature (300 K) up to 400 K and reversed. Figure 5.4 shows a plot of the four-probe resistance of a suspended VO_2 NW of 140nm width. Upon heating (red curve), the resistance gradually decreases typical of a semiconductor and abruptly changes by about four orders of magnitude at $T_{global} \sim 352$ K (from 3.07×10^6 Ω to 954 Ω). A hysteresis loop is clearly observed during the temperature cycling.

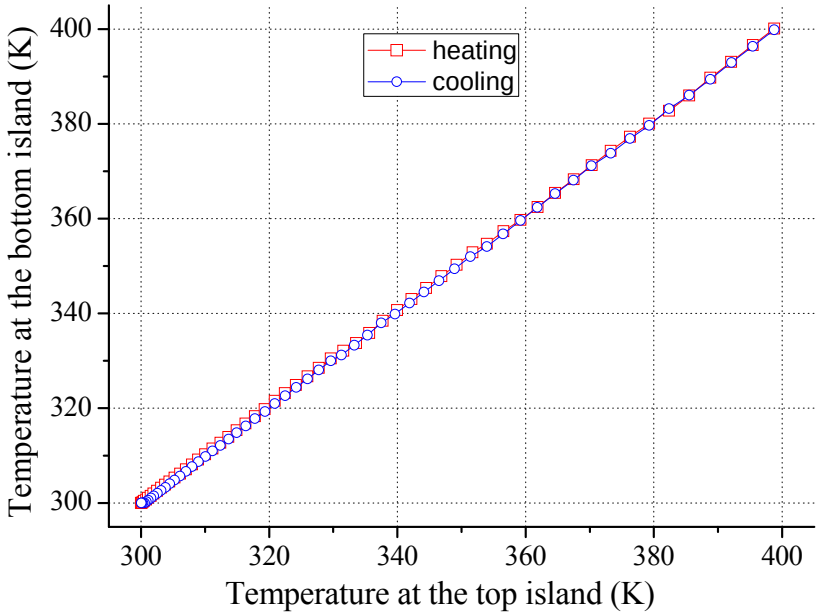

Figure 5.3: Temperature of both islands upon heating (red curve) and cooling (blue curve).

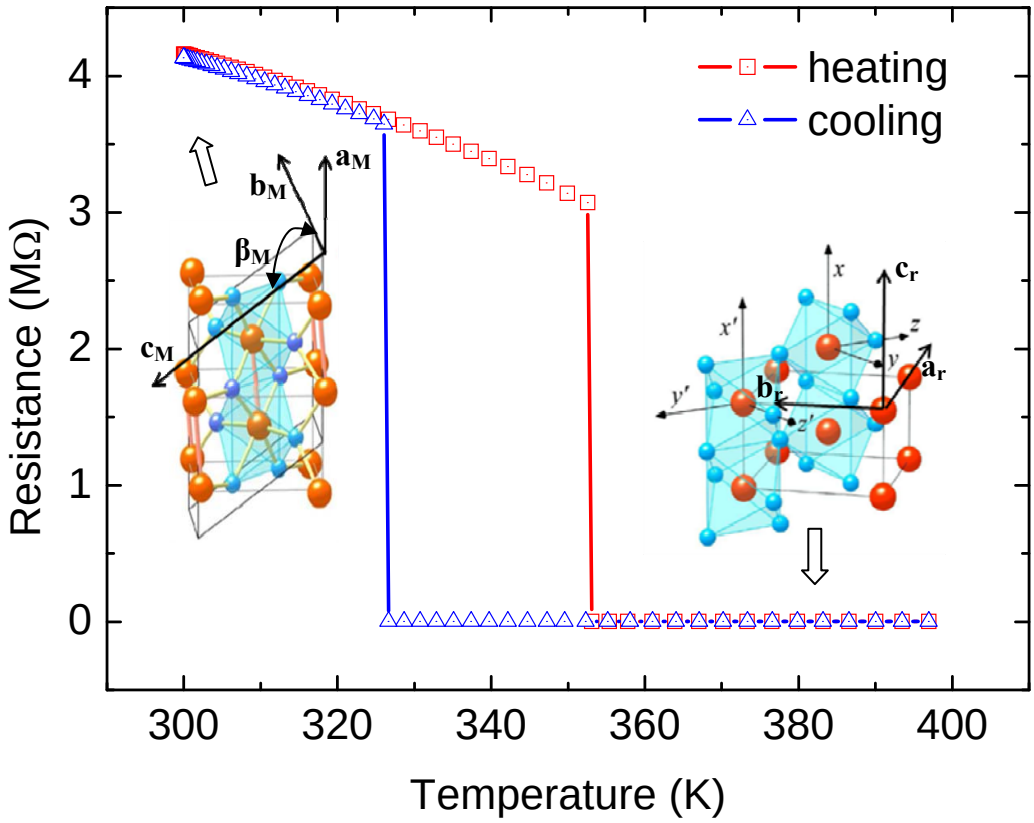

Figure 5.4: Four-probe resistance of 160 nm wide suspended VO_2 NW as a function of temperature. Red and blue curves are taken upon heating and cooling, respectively. Insets show the crystal structures of the low-temperature, monoclinic insulating phase (left), and the high-temperature, rutile metallic phase (right), the large spheres and the small spheres represent vanadium atoms and oxygen atoms, respectively [9].

During the cooling process (blue curve), the resistance remains low in the metallic phase until the temperature reaches ~327K. Below 327 K, the resistance sharply increases and returns to semiconductor behavior. These hysteretic loop and abrupt changes in the resistance curve are the signatures of a first-order MIT [8] and single domain behavior. The MIT is accompanied by a structural phase transition from the low-temperature monoclinic insulating phase to high-temperature rutile metallic phase [9]. In the high temperature region, the VO_2 NW remains in the metallic phase with a rutile crystal lattice structure (right inset of Figure 5.4). On the other hand, the VO_2 NW owns less symmetric monoclinic (M_1) structure at the low temperature range (left inset of Figure 5.4). When VO_2 goes through the transition from the high temperature rutile phase to the low temperature monoclinic phase the lattice structure changes in following ways. Vanadium atoms in the c-axis direction pair up and distort into dimerized zigzag chains. The distance between vanadium atoms alternates, meanwhile the corresponding oxygen octahedrons almost remain in their original position. Consequently, the two sub-lattices are still equivalent by symmetry as in the rutile phase [9, 20].

The measurement results from the VO_2 NWs studied show that all of them exhibit single domain behavior but the transition temperature and hysteresis varies from sample to sample. The transition from insulating to metallic phase upon heating occurs in a range of temperatures $T_{I\text{-}M} \sim 350 – 355$ K. The transition temperature from metallic to insulating phase ($T_{M\text{-}I}$) upon cooling covers a much wider range. As shown in Figure 5.5, when the temperature lowers, the NW remains in the metallic phase down to 305 K for the 210 nm-wide NW, which is much lower than that for the 140 nm-wide NW.

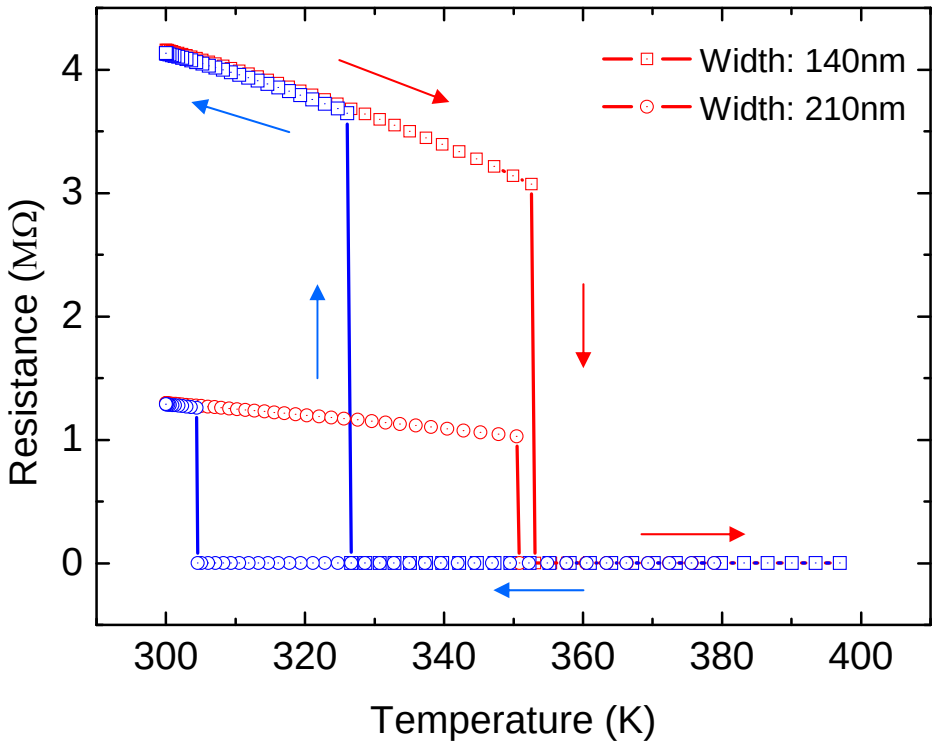

Figure 5.5: Four-probe electrical resistance of suspended VO_2 NWs of 140 nm and 210 nm widths. The arrows indicate the direction of temperature changes.

The large variation in the temperature T_{M-I}, at which the insulating phase suddenly appears, between NWs has also been observed by Wei *et al*. [19]. Imperfections or defects such as oxygen vacancies, and vanadium interstitials [21] are supposed to be factors that can delay the transition from metallic phase to insulating phase (lowering T_{M-I}). That delay widens the hysteresis loops as observed in Figure 5.5. The variation of T_{M-I} could reflect the different density of such defects in our NWs studied. The semiconducting behavior of the insulating phase can be expressed via the resistance – temperature function [22]:

$$R = R_0 e^{\frac{E_a}{k_B T}} \tag{5.1}$$

where R, T, E_a, and k_B are resistance, temperature, activation energy, and Boltzmann's constant, respectively.

By plotting the logarithmic resistance [ln(R)] versus reciprocal temperature ($1/T$), the thermal activation energy (E_a) of each NW can be calculated (Figure 5.6). The activation energies of the 140 nm and 210 nm wide VO_2 NWs are 0.074 and 0.056 eV, respectively. These activation energies are considerably lower than the 0.24 – 0.45 eV found in bulk samples [23, 24] and smaller than the 0.09 eV found in VO_2 nanobeam on a Si_3N_4/Si substrate [21]. The interface interaction between nanobeam and the substrate could impact the resistance behavior of their VO_2 nanobeams which makes the thermal activation energy higher. A summary of resistance at room temperature, $T_{I\text{-}M}$, $T_{M\text{-}I}$, and activation energy of the two NW samples mentioned above is shown in Table 5.1.

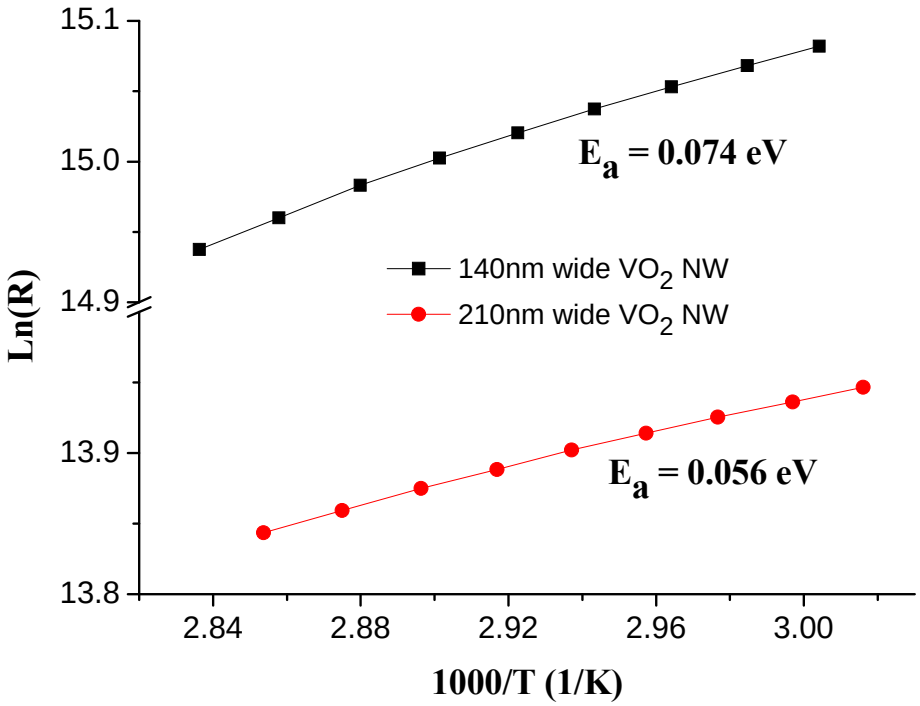

Figure 5.6: Plot of logarithmic resistance versus reciprocal temperature of 140 nm and 210 nm wide VO_2 NWs.

Table 5.1: Measurement result summary of 140 nm and 210 nm wide VO_2 NWs

Nanowire width (nm)	Resistance at room temperature (MΩ)	Transition temperature from insulating to metallic phase T_{I-M} (K)	Transition temperature from metallic to insulating phase T_{M-I} (K)	Thermal activation energy (eV)
140	4.16	353	327	0.074
210	1.30	350	305	0.056

5.3.2. Coexistent domain behavior and persistent metallic domain pinned in VO_2 NWs

Domain formation in VO_2 nanobeams upon sweeping temperature in the vicinity of the MIT has been studied intensively, in which multi-domain formation was observed in VO_2 nanobeams clamped on a substrate or by bending VO_2 NWs [15, 17, 19, 25]. Coexistent domain formation was also observed in VO_2 nanobeams hung between two electrodes on substrate [19]. However, the metallic domains were formed very randomly and lacked controllability. With the advantage of our METS devices, we can intentionally create a metallic domain at one end of VO_2 NW by heating up only one membrane-island (heating membrane). The resistance – heating temperature (T_h) behavior of the 210 nm wide VO_2 NW is shown in Figure 5.7. During heating, because of temperature gradient, some heat will flow to the other membrane-island via the NW and increase its temperature to T_s. T_s corresponding to each T_h value is also indicated in the top x-axis in Figure 5.7. Firstly, the resistance follows semiconductor behavior until T_h reaches the MIT temperature (T_h ~ 353 K, T_s ~ 317 K), at which point a metallic domain appears. Over this interval, the resistance of the whole wire decreases from 1.3 MΩ to 1.12 MΩ.

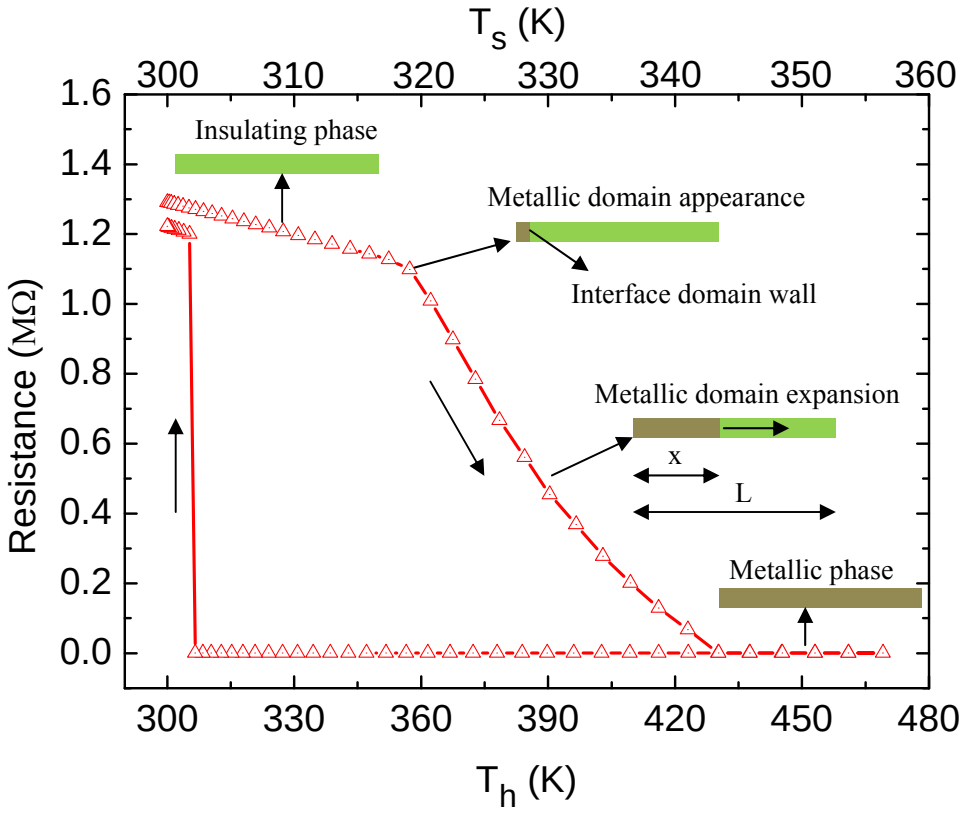

Figure 5.7: Resistance versus heating temperature behavior of 210 nm wide VO_2 NW.

As T_h increases, the resistance decreases as the metallic domain grows and expands to the other end until whole NW turns into metallic phase with a resistance of 381 Ω at T_h ~ 430 K (T_s ~ 343 K). Upon cooling, hysteresis is also observed. The NW remains in the metallic phase down to T_h ~ 306 K (T_s ~ 301 K), at which point the NW turns back into insulating phase. The schematic diagrams of the transition progress in NW are shown as insets in Figure 5.7. During the transition process, the interface domain wall moves from the heater side to the sensor side (left to right in the inset schematic diagram). To demonstrate the co-existence of metal and insulator (M – I) domains we used a laser beam to heat up one membrane-island while observing the image under an optical microscope (the experiment was carried out using confocal Raman microscopy). The power of laser beam should be high enough to heat up one end of

NW to a temperature beyond the MIT temperature. As a result, a temperature gradient is established between two ends of NW in a manner similar to the above experiment. The optical images of VO_2 NW with and without laser heating are shown in Figure 5.8. At room temperature without laser heating the suspended part of NW is in homogeneous insulating phase (Figure 5.8a). As observed in Figure 5.8b, a part of the NW near the membrane-island heated by laser beam turns to metallic phase. This co-existent M – I domain structure is stable with constant laser beam power. Increasing the power of laser beam would make metallic domain expand along the NW to the left hand side.

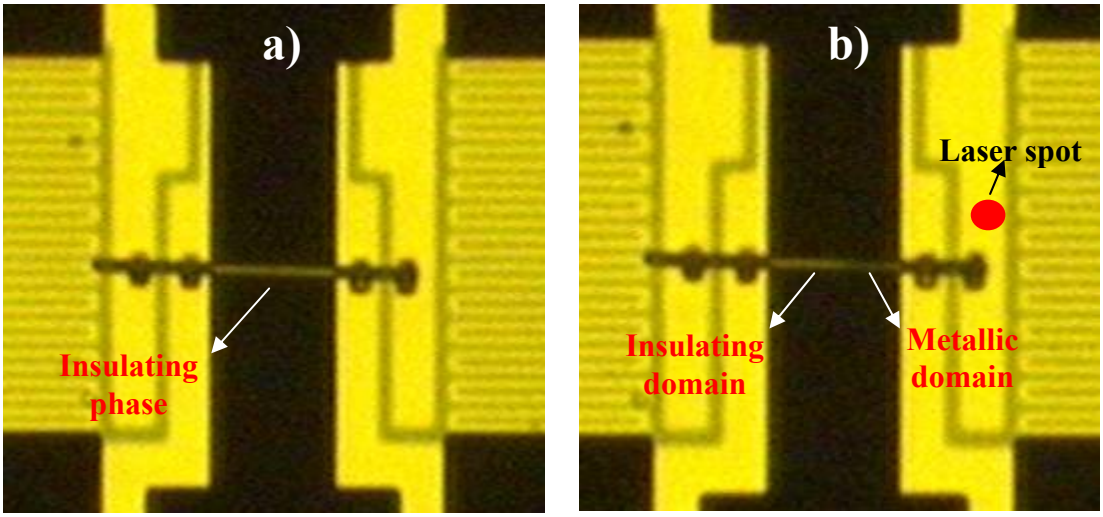

Figure 5.8: Optical image of VO_2 NW (a) without laser heating, and (b) with laser heating at right hand side membrane-island.

In the co-existence phase, the total resistance of NW is the sum of the contact resistance, the domain wall resistance, the resistance of metallic domain, and the resistance of the insulating domain:

$$R_{Tot} = R_C + R_{DW} + r\rho_m \frac{L}{A} + (1-r)\rho_i \frac{L}{A} \tag{5.2}$$

where ρ_m and ρ_i are the insulator and metal resistivities in co-existence phase, R_C and R_{DW} are the resistance of the contact and of the domain wall, and r is the ratio of metallic domain over entire NW ($r = x/L$), x is the length of metallic domain in the co-existence regime, A and L are the cross-sectional area and the length of NW, respectively. In our four-probe measurement, the resistance of the contact R_C can be neglected. In addition, we assume that the resistances of the metallic domain and of the interface domain wall R_{DW} are also negligible compared to that of insulating domain when the insulating phase is present. Therefore, prior to complete transformation to metallic phase, the total resistance of NW can be expressed as

$$R_{Tot} = (1-r)\rho_i \frac{L}{A} = (1-r)R_i \tag{5.3}$$

With the note that the resistivity of insulating domain in the co-existence phase is independent of temperature [19] and assuming that the resistance change by temperature of the insulating domain is much smaller than the change caused by the shrinking of that domain, we can plot the dependence of ratio r on the heating temperature (T_h) (Figure 5.9). It is worth highlighting here that, with our unique measurement configuration, we can manipulate the position of the interface domain wall in the co-existence phase by controlling the temperature at the heating island (T_h).

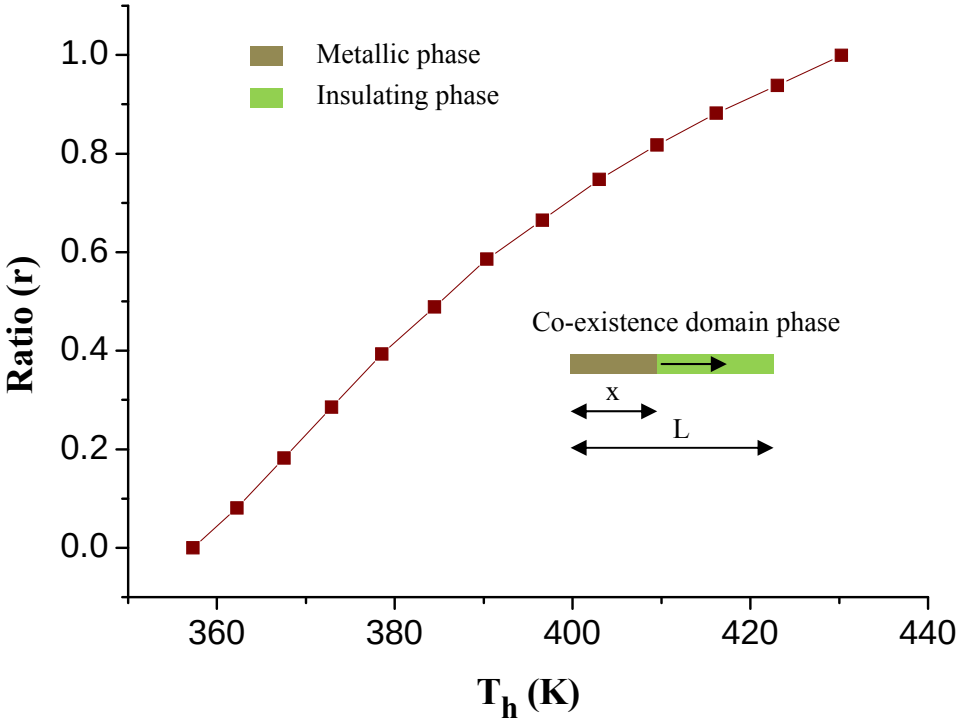

Figure 5.9: The dependence of metallic domain portion ($r = x/L$) on heating temperature (T_h) in the co-existence phase during transition for 210 nm wide VO_2 NW.

As observed in Figure 5.7, when the NW turns back into the insulating phase upon ramping down T_h, the resistance of NW is smaller than the original. The resistance of NW at room temperature after temperature cycling is 1.22 MΩ which is ~94% of that before cycling. The resistance of the NW in insulating phase keeps decreasing with repeated measurements. Figure 5.10a shows such resistance decreasing over four measurements at different times, the 4th sweep (black curve) taken right after the 3rd sweep (green curve). As observed in Figure 5.10a, the resistance in insulating phase when T_h increases in the 4th sweep coincides with that of the NW in insulating phase when T_h decreases in the 3rd sweep. This coincidence indicates that the reduction of resistance in the insulating phase happens when NW is cooled down from high temperature metallic phase. A possible reason for this phenomenon is that some

metallic domains are persistently pinned in the NW during the transition from metallic phase to insulating phase. These metallic domains make the resistance of the NW in insulating phase smaller than before temperature sweep. In addition, more and more such metallic domains are created and pinned in the NW after each measurement causing progressive reduction of resistance. After a certain number of sweeps, we found that the resistance of NW in insulating phase remained unchanged and the resistance – heating temperature curves then became repeatable. This suggests that no further creation of pinned metallic domains in the NW. Figure 5.10b shows the resistance versus T_h for the first measurement and the measurement after structural stabilization. In comparison with the original value, the resistance has reduced significantly (from 1.3 MΩ to 0.435 MΩ) in its stabilized state with large domains of metallic phase pinned in NW. For convenience, from now onward we abbreviate the NW with pinned metallic domains in stabilized state by NW_P, the low temperature insulating phase and the high temperature metallic phase of the NW with pinned metallic domains by I_P phase and M_P phase, respectively.

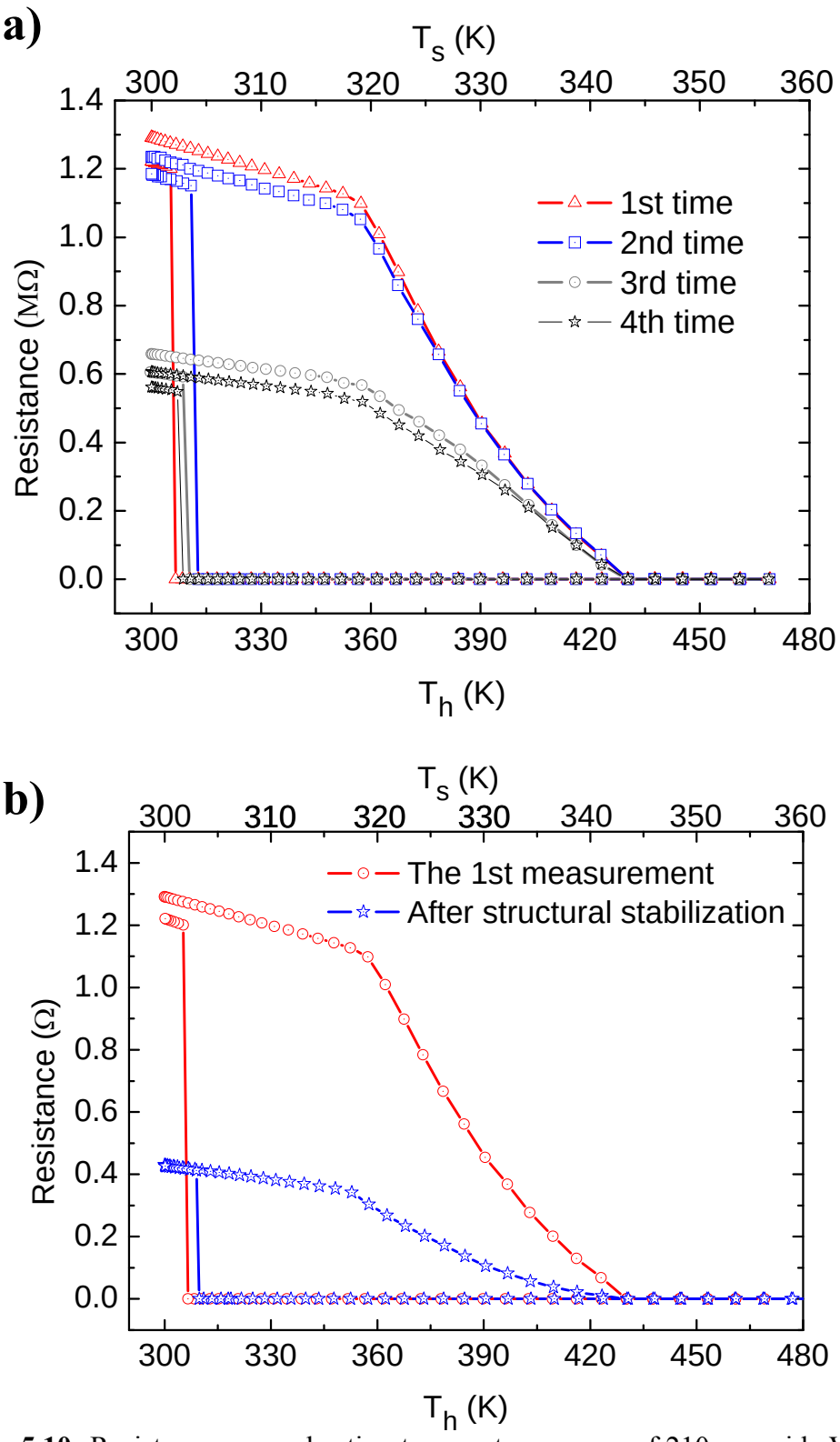

Figure 5.10: Resistance versus heating temperature curves of 210 nm wide VO_2 NW (a) for several measurements and (b) comparison between the original and stabilized states.

Interestingly, the single domain behavior is still maintained in NW_Ps. Figure 5.11 shows the resistance of (a) 210 nm wide and (b) 140 nm wide VO_2 NW_Ps as a function of temperature after stabilization. The temperature in this case was established without a temperature gradient along the NW by heating both membranes simultaneously. The sharp resistance drop at ~350K and abrupt increase at (a) ~ 305 K or (b) ~ 321 K are evidence of sudden change from I_P phase to single-domain M_P phase and vice versa. That phenomenon was observed in all studied VO_2 NWs. The portion of metallic domains pinned inside the NW is different from sample to sample. Herein, we define the portion of metallic domains over the entire NW as

$$P = \frac{V_{M,s}}{V_{NW}} = 1 - \frac{V_{I,s}}{V_{NM}} \tag{5.4}$$

where $V_{M,s}$, $V_{I,s}$, and V_{NW} are the volume of the pinned metallic domains and the insulating domains in NW at room temperature in the stabilized state, and the volume of NW, respectively. Since the resistance of metallic domains is negligible, the resistance measured in Figure 5.11 is the resistance of the insulating domains which is proportional to the volume of those domains. Consequently, the equation 5.4 can be expressed

$$P = 1 - \frac{R_s}{R} \tag{5.5}$$

where R_s and R are the resistances of the NW after stabilization and in the original state, respectively. It can be inferred from our measurement that the portion of pinned metallic domains in the I_P phase in the thinner NW is higher than in the thicker one. For example, at room temperature the pinned metallic domain portion in the 140 nm wide NW_P is ~90% (resistance decreased from 4.16 MΩ to 0.40 MΩ), meanwhile in

the 210 nm wide NW_P the portion is ~67% (resistance decreased from 1.3 MΩ to 0.43 MΩ).

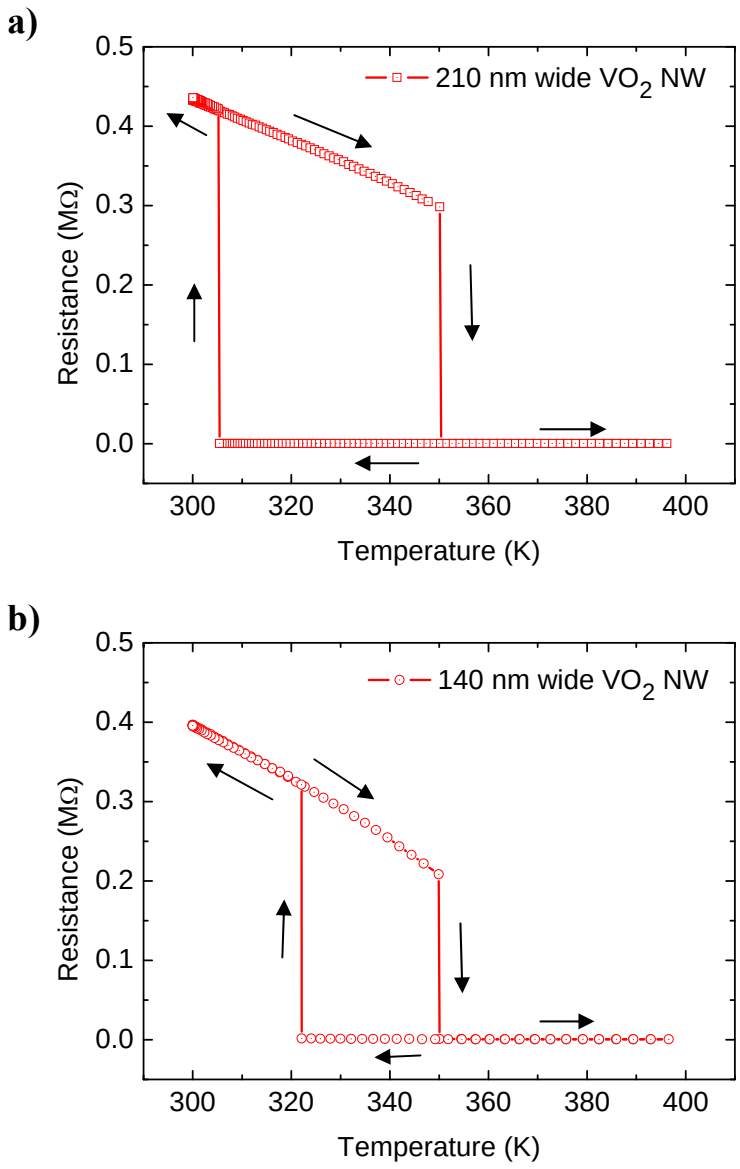

Figure 5.11: Resistance versus temperature of 210 nm (a) and 140 nm (b) wide VO_2 NW_PS, the arrows indicates temperature sweeping direction.

Figure 5.12a shows the room-temperature optical image of part of a NW on the METS device after measurement. The multi-domain structure observed in the

image indicates that some metallic domains are pinned and stabilized along the NW at low temperature. We also used Raman spectroscopy to distinguish the co-existing structure phases at room temperature. Raman spectra were recorded using 532 nm exciting laser in a WITec alpha300R confocal Raman microscope. The spatial resolution is 600 nm and the spectral resolution is 0.9 cm^{-1}. Raman spectra were collected when the incident laser scanned along the NW. Local heating was minimized by using low laser power (< 0.01 mW). Different structural phases of VO_2 NW were identified by their Raman spectra as shown in Figure 5.12b. The Raman spectrum with the peaks (denoted by black dots) at 608 cm^{-1} corresponds to monoclinic (M1) insulating phase. On the other hand, the Raman spectrum with the absence of identifiable M1 peaks corresponds to rutile metallic phase [22, 25]. From Raman spectra acquired along the length of NW, the domains of insulating (M1) and metallic (R) phases were mapped with a resolution of ~600 nm. The schematic diagram of NW_P based on Raman spectra mapping is shown at the right hand side of Figure 5.12b. That structural domain mapping is in good agreement with the observation from optical microscope image (Figure 5.12a).

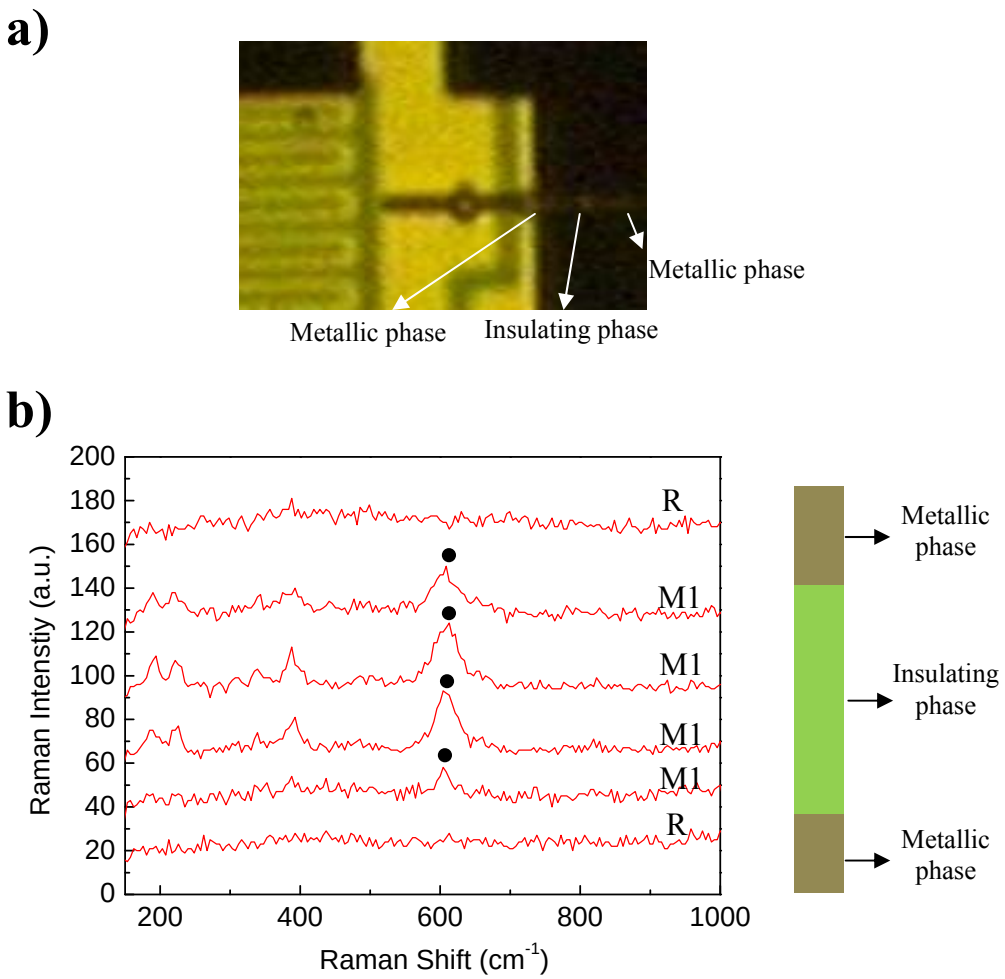

Figure 5.12: (a) Optical microscope image of VO_2 NW on METS device taken at room temperature, and (b) Raman spectra obtained by scanning incident laser along the NW and schematic diagram of NW_P.

The electrical and thermal behavior of VO_2 NW_P must be considered in the processing of VO_2 nanowire-based devices. The metallic-domain pinning effect could also be exploited for devices with new functionalities. Hence, understanding the mechanism behind this effect is necessary and will be discussed below. Zhang *et al.* [25] observed co-existing rutile (metal) and monoclinic (insulating) domains in some post-synthesized free-standing VO_2 nanobeams at room temperature. They found that the yield of nanobeams with rutile domains at room temperature is very sensitive to

the total reactor pressure and growth substrate preparation. The oxygen vacancies and related defects such as interstitial vanadium atoms introducing both extra electrons and internal strain could be the reasons for stabilizing the rutile phase at room temperature. They suggested that the nanobeam geometry with its single crystal form and high surface-area-to-volume ratio may enable the defect distribution to couple to the strain state which could stabilize the rutile phase at low temperature. In contrast to their multiple M-I domains observation on free-standing VO_2 NWs at room temperature right after synthesis, in our experiment the pinned metallic domains were observed in NWs after temperature cycling at one end of NW. Because of temperature gradient along the NW length, the different thermal expansion between different sections of the NW, especially between metallic and insulating domains, could induce thermal stress inside the wire. As discussed above, oxygen vacancies and/or vanadium interstitials may be the factors that delay the transition from metallic phase to insulating phase during cooling. We believe that the thermal stress coupled with such defects create pinning points at which the metallic domains are maintained even at room temperature.

To understand what happens in NWs after temperature ramping we prepared NWs on copper grid for transmission electron microscope (TEM) observation. NWs were dispersed in ethanol and transferred to copper grids by drop-casting. Before TEM inspection, the samples were annealed in forming gas at 530 K for 2 hours. Figure 5.13 shows the TEM images after annealing. As observed in Figure 5.13a, the free end of NW shows featureless contrast, whereas parts that bridged the holey carbon network show many fringes along the length (Figure 5.13b). These fringes reflect the strain contrast which had previously been observed in bent NWs [26]. In a similar manner, in our measurements the NWs were bridged between two membrane-

islands. Thermal stress would certainly exist along the NW length after temperature cycling. Alongside intrinsic defects, pinning centres at which the metallic domains were persistently trapped at room temperature emerge and increase after every temperature cycle until a stable configuration is reached.

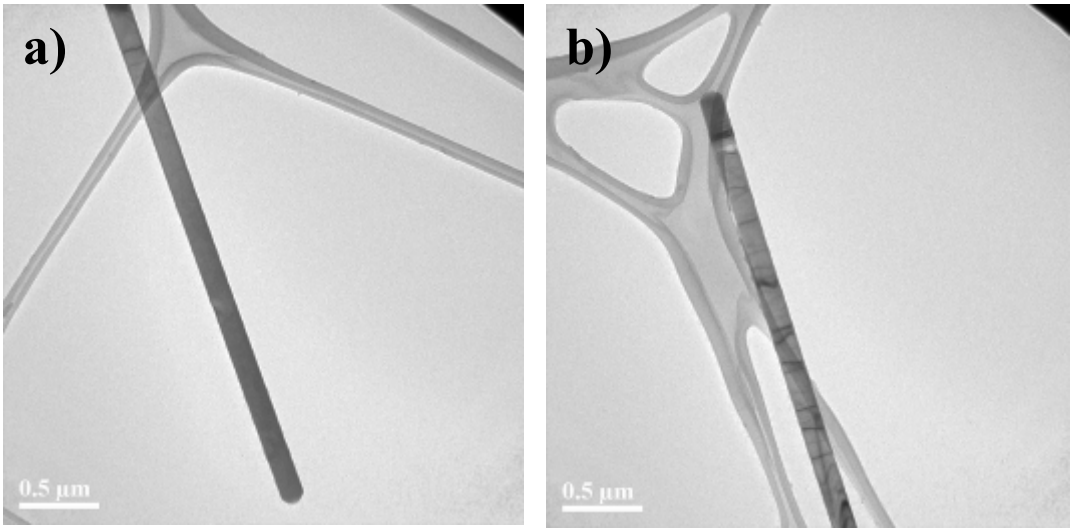

Figure 5.13: TEM images of VO_2 NW on copper grid after annealing in forming gas at 530 K for 2 hours.

Although metallic domains persist at room temperature, decoupling thermal stress and defects may recover the NW from a pinned state. Remarkably, externally applied tensile stress can recover the resistance of NW at room temperature to nearly its original value. We postulate that at certain tensile stress the thermal stress inside NW is relaxed which decouples with the defects. Consequently, the metallic domains are released and turn back to usual insulating phase at low temperature. The details of the experiment and phenomena will be presented in following section.

5.3.3. Electrical properties of VO_2 NWs under external tensile stress and bending

In order to apply tensile stress or bending on NWs, we used two tungsten tips attached to nano-manipulators to pull or push the two membrane-islands attached to the ends of the NW. The experiments were carried out in an SEM chamber. Figure 5.14 shows the SEM image of a VO_2 NW on METS device with 2 tungsten tips positioned for the application of an external force (pulling and pushing). The tensile force was transferred to NWs by pulling apart the centre nitride beams of the two suspended membranes using the tips. On the other hand, pushing these nitride beams will bend the NWs. The SEM images of experimental structure in pulling and pushing tests are shown in Figure 5.15. The tensile force applied on NW is proportional to the distance (x) between two inner nitride beams at the tips-nitride beam contact points (Figure 5.15a) such that by changing x we can vary the applied force on NW. The temperature dependent electrical resistance of the NW was measured for different applied forces. To quantify the force, we used AFM cantilevers of known spring constant instead of tungsten tips to pull the nitride beams. By measuring the cantilever deflection corresponding to each value of x, the applied force can then be calibrated. The details of force quantification and the measurement results are elaborated below.

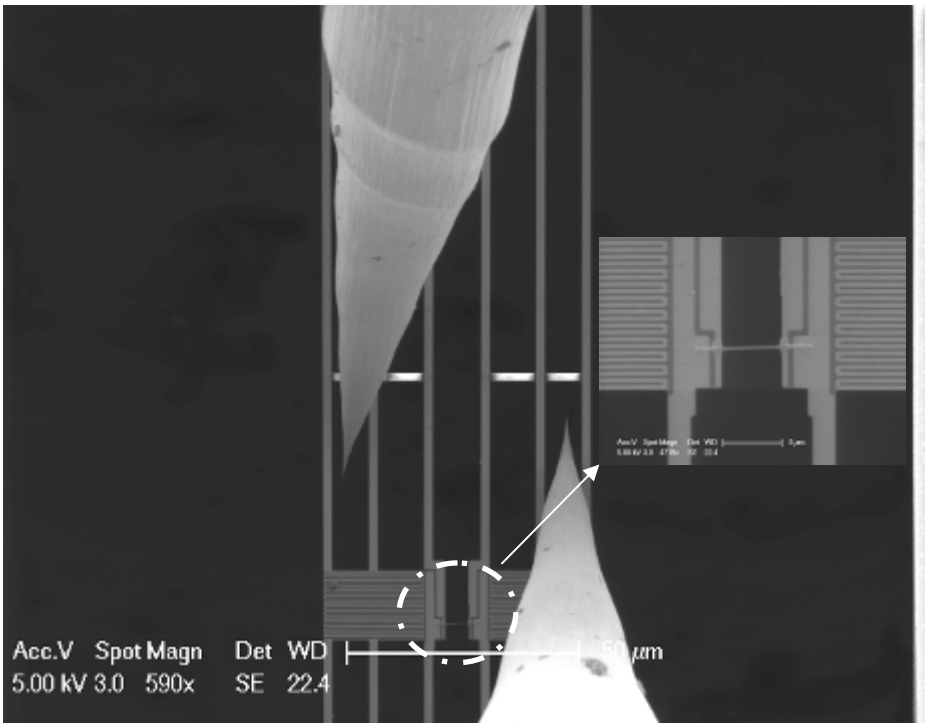

Figure 5.14: SEM image of VO_2 NW sample on METS device with two tungsten tips for external force experiment.

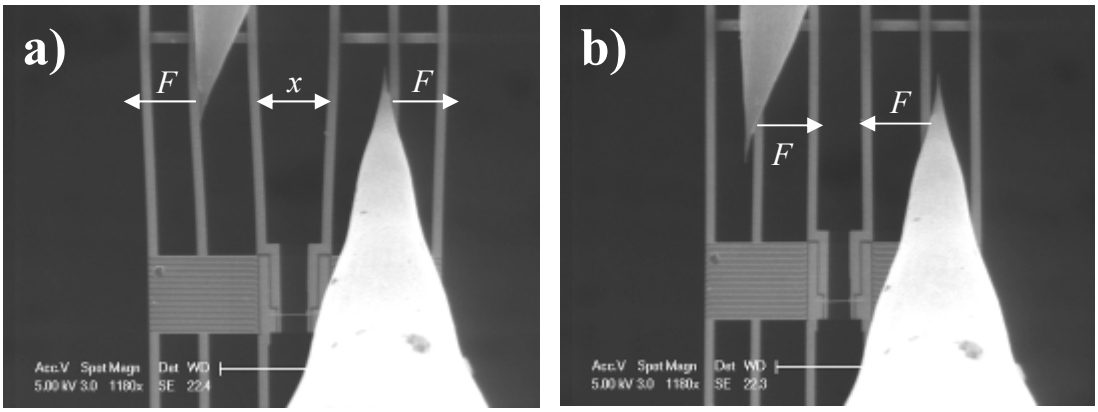

Figure 5.15: SEM images of the structures in (a) pulling, and (b) pushing test.

5.3.3.1. Measurement of applied force

AFM cantilevers of length 222 µm and force constant (*k*) of 40 N/m were used in place of tungsten tips for calibration. A variation of the METS device with an integrated Pt/SiN_x beam that bridges two suspended membranes was employed for

force calibration. Figures 5.16 a and b show the device before and after application of a pulling force. The gap between two inner nitride beams without a pulling force is 10.3 μm. The SEM images of the lower AFM cantilever before and after application of a pulling force are shown in Figures 5.16 c and d, respectively. Figure 5.16e shows the sketches describing the deflection of AFM cantilever in the experiment, in which the deflection can be expressed as:

$$\Delta z = L_0 \times \sin(\theta' - \theta) \tag{5.6}$$

$$\text{with} \quad \sin\theta = \frac{L_P}{L_0} \quad \text{and} \quad \sin\theta' = \frac{L_P'}{L_0} \tag{5.7}$$

where Δz, L_0, L_P, $L_{P'}$, θ, θ' are the deflection, length, projected length before pulling, projected length after pulling, angle to vertical direction before pulling, and angle to vertical direction after pulling of cantilever. L_P and $L_{P'}$ are measured from SEM images as indicated in Figures 5.16 c and d. The force applied on nitride beam corresponding to the deflection Δz is perpendicular to cantilever and is given by

$$F = k \times \Delta z \tag{5.8}$$

where k is the force constant of AFM cantilever. The parallel component of that force, F_{ex}, will transfer to NW (referring to Figure 5.16e) and is expressed as

$$F_{ex} = F \times \cos\theta' \tag{5.9}$$

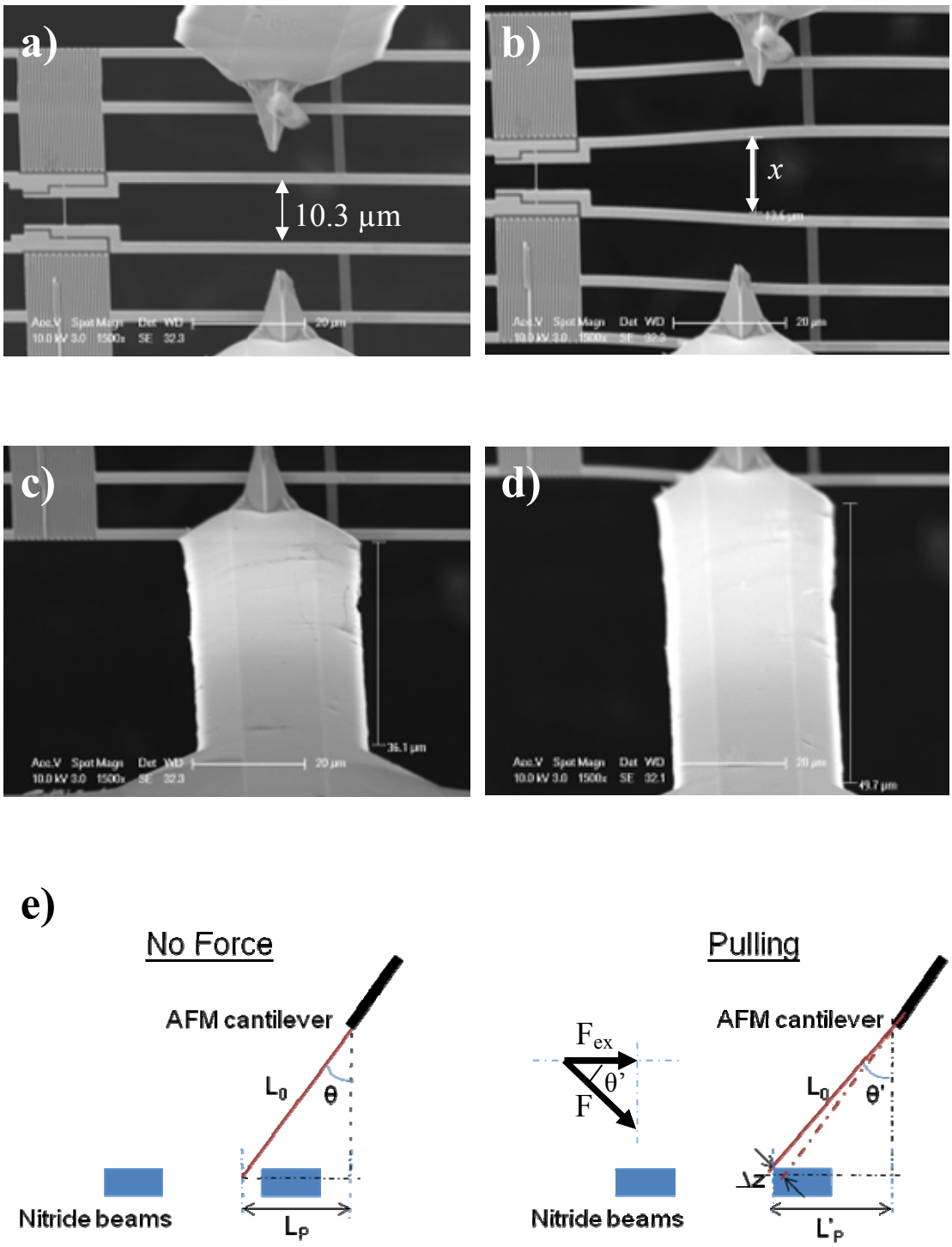

Figure 5.16: SEM images of METS device with integrated Pt/SiN_x beam bridging two suspended membranes before (a) and after (b) pulling by AFM cantilevers; SEM images of bottom cantilever corresponding to before (c) and after (d) pulling; and sketches describing the deflection of cantilever in force quantifying experiment (e).

From this approach, the external force applied on NW can be controlled by the gap distance x. Table 5.2 shows the details of parameters and the external forces F_{ex} applied to the NW corresponding to each value of x. The maximum force is 0.54 mN corresponding to the gap distance of 13.6 µm. The external tensile force increases almost linearly with the gap distance in the measurement range. The linear dependence of F_{ex} on x is clearly shown in Figure 5.17.

Table 5.2: Details of parameters and external forces corresponding to each value of gap distance x

Test #	Gap distance x (µm)	Cantilever projection length L'_P (µm)	Deflection angle θ'-θ (^{0})	Cantilever deflection Δz (µm)	External force F_{ex} (mN)
#1	10.3	36.1	0	0	0
#2	11.5	41.2	1.34	5.17	0.203
#3	12.3	44.2	2.12	8.23	0.323
#4	13.0	47.4	2.97	11.5	0.449
#5	13.6	49.7	3.58	13.8	0.540

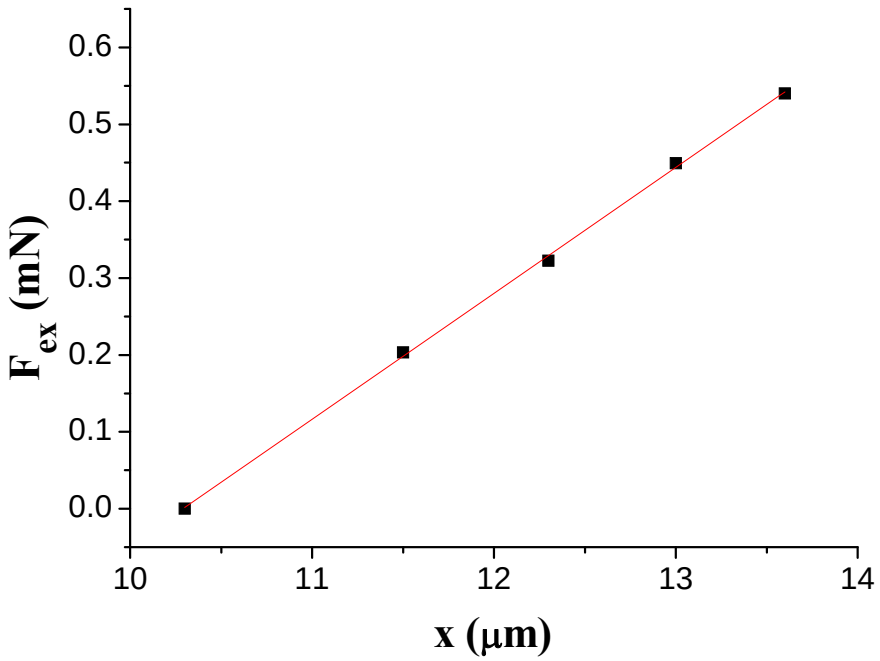

Figure 5.17: Dependence of external tensile force applied on NW on the gap distance between two inner SiN_x beams at the contact points.

5.3.3.2. Properties of NW under external tensile stress

The 210 nm wide VO_2 NW_P described in section 5.3.2 was investigated. The tensile stress was determined based on the applied force and the cross-sectional area of NW. Figure 5.18 shows the temperature dependent electrical resistance measurement at applied tensile stress of 4.6 GPa and 12.2 GPa. The temperature-resistance curve without tensile stress is also presented for comparison. At room temperature, the resistance of NW_P increases from 0.43 MΩ to 0.46 MΩ and 1.1 MΩ corresponding to tensile stress values of 4.6 GPa and 12.2 GPa, respectively. The thermal stress relaxation is postulated to occur which causes the insulating phase to revive from the pinned-metallic state. At 12.2 GPa, the resistance of NW almost recovered to ~85% of the original value which indicates that a large portion of pinned metallic domains return to their original insulating phase. An interesting phenomenon is observed in the NW's resistance behavior with the lower applied tensile stress of 4.6 GPa. Upon heating, the resistance decreases in the same manner as the unstressed wire, but shows an upward jump at $T_{1,R}$ = 330 K (from 0.39 MΩ to 1.0 MΩ) and then gradually decreases in a manner expected of insulating behavior until $T_{1,I\text{-}M}$ = 361 K at which point it drops to the metallic value. Upon cooling, the resistance maintains its metallic value until temperature $T_{1,M\text{-}I}$ = 317 K where it jumps sharply and thereafter follows the trajectory of the heating process. Meanwhile, under the higher tensile stress of 12.2 GPa we observed only the abrupt change at $T_{2,I\text{-}M}$ = 367 K during heating and at $T_{2,M\text{-}I}$ = 334 K during cooling corresponding to transition from insulating phase to metallic phase and from metallic phase back to insulating phase, respectively. Interestingly, the sharp transitions are indicative of single domain behavior in the NW under tensile stress. As discussed previously, the metallic domains are thought to be pinned at low temperature on the assumption that the

thermal stress accompanied by the defects causes the pinning force to maintain the metallic domains. By compensating for thermal stress using a tensile force, one can decouple the thermal stress and the defects. Consequently, the pinned metallic domains will revert to the original insulating phase. At lower tensile stress (4.6 GPa), the change in resistance at low temperature is marginal. However, when the temperature reaches to $T_{I,R}$ ~ 330 K the thermal energy is high enough and combines with tensile stress to overcome the pinning force. As a result, the insulating phase is recovered from pinned metallic domains, which is substantiated by the upward jumps at 330 K in the resistance curve with 4.6 GPa tensile stress (blue curve in Figure 5.18)

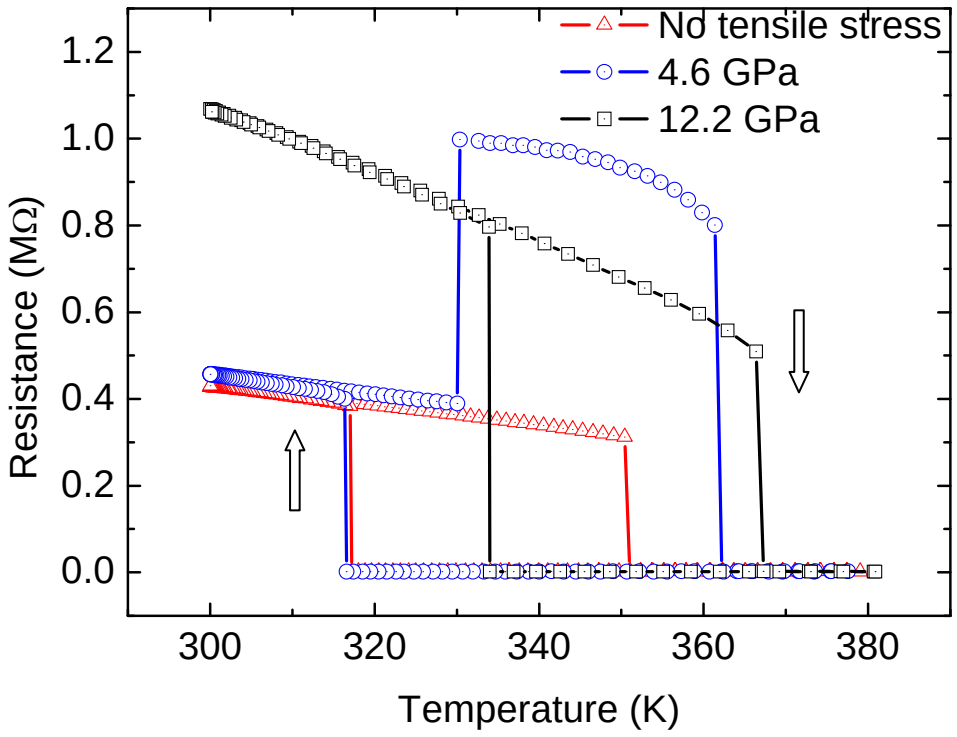

Figure 5.18: Electrical resistance versus temperature curves of 210 nm wide VO_2 NW_P at different external tensile stress (both membrane-islands heating).

Most interestingly, when the applied stress is removed, the temperature dependent resistance is back to its original behavior (red curve in Figure 5.18) which indicates

the relaxation of trapped centres and hence the metallic domains are pinned in the NW once again.

The temperature $T_{I\text{-}M}$, at which the transition from insulating phase to metallic phase happens, increases with an increase in tensile stress. As observed in Figure 5.18, that temperature is 350 K, 361 K, and 367 K for no tensile stress, 4.6 GPa, and 12.2 GPa tensile stress, respectively. An increase in $T_{I\text{-}M}$ with strain had also been observed in VO_2 thin films [27, 28] and a shift of up to 50 K in $T_{I\text{-}M}$ can be also achieved in bulk VO_2 by loading tensile or compressive external uniaxial stress [29, 30].

5.3.3.3. Properties of bent NW

Figure 5.19a shows an SEM image of VO_2 NW on METS device in a bending experiment. The NW_P was bent by pushing two membrane-islands inward using two tungsten tips. The large reduction of the gap between two membranes at the NW's position from 5.09 μm to 4.58 μm should not correspond to compression but bending. The schematic sketch of bent NW is shown in the inset of Figure 5.19b. The bent NW exhibits remarkably different resistance behavior upon temperature cycling as shown in Figure 5.19b. Upon heating half cycles, the resistance starts decrease at temperature ~ 320 K and changes in many discrete steps over a wide temperature range during MIT. At ~350 K, the resistance drops to the metallic value which indicates that the transition is completed and NW turns to M_P phase. In the cooling half cycle, the resistance also changes in many discrete steps during MIT and reach the original value at low temperature. Such behavior typifies multiple M – I domain formation in the NW during the transition, a phenomenon which is also observed in VO_2

nanobeams lying on a SiO_2 substrate [17]. The evidence of multiple M – I domain formation during MIT in bent VO_2 nanobeams was also claimed by other groups [15, 31, 32].

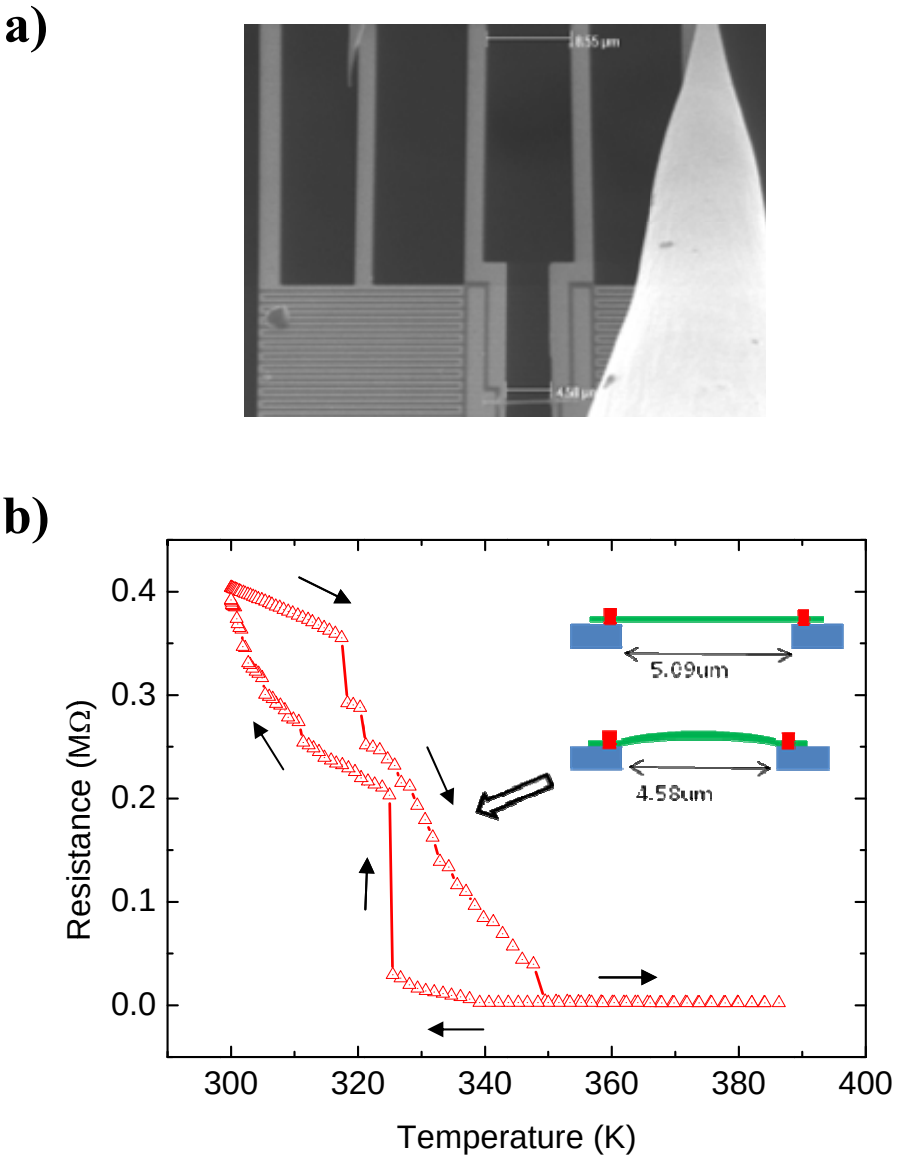

Figure 5.19: (a) SEM image of 210 nm wide VO_2 NW on METS device in bending experiment using two tungsten tips, and (b) Electrical resistance behavior of bent NW as function of temperature (inset: schematic sketches of NW before and after bending).

5.3.4. Effect of surface coating

To further understand the effect of strain/stress on the MIT of VO_2 NWs, we

intentionally coated an amorphous carbonaceous (a-C) layer on the NW's surface by irradiation in the SEM operating at 30kV over a period of 2 hours. The detail of coating method is described in chapter 4 (section 4.3). SEM images of the 210 nm wide NW before and after coating are shown in Figures 5.20 a and b, respectively. The thickness of a-C layer is ~ 40nm as determined from the SEM images. A schematic of the NW core with a-C shell is shown in the inset of Figure 5.20. A four-probe electrical resistance measurement as function of temperature was then performed on such VO_2/a-C core/shell NW. The results show that the resistance of NW remains at its metallic value even at room temperature upon cooling. The phenomenon showed that surface coating can stabilize the M_P phase even at room temperature. To further understand the behavior of NW at lower temperature, a liquid nitrogen cryostat was employed to keep the sample holder stage at a base temperature T_{base} = 280 K. The temperature of sample was then cycled from 280 K to 410 K (Figure 5.20). While single-domain behavior is still observed in the coated NW, the surface coating had significantly affected the electrical properties of NW in the following ways. Firstly, the resistance of NW at I_P phase is further decreased from 0.43 MΩ to 0.2 MΩ at 300 K which suggests that more metallic domains were pinned in NW. Secondly, the transition from I_P phase to M_P phase upon heating happens at a higher temperature $T_{I\text{-}M}$ ~ 357 K. Lastly, upon cooling the NW remains in the M_P phase until temperature $T_{M\text{-}I}$ ~ 291 K at which point the NW turns back to I_P phase abruptly. We postulate that the interfacial strain/stress induced by the mismatch of thermal expansion between VO_2 NW core and a-C shell may be the reason for more metallic domain pinning and wider the hysteresis as observed. It should be highlighted here that the MIT temperature of VO_2 NW can be significantly modified by surface coating.

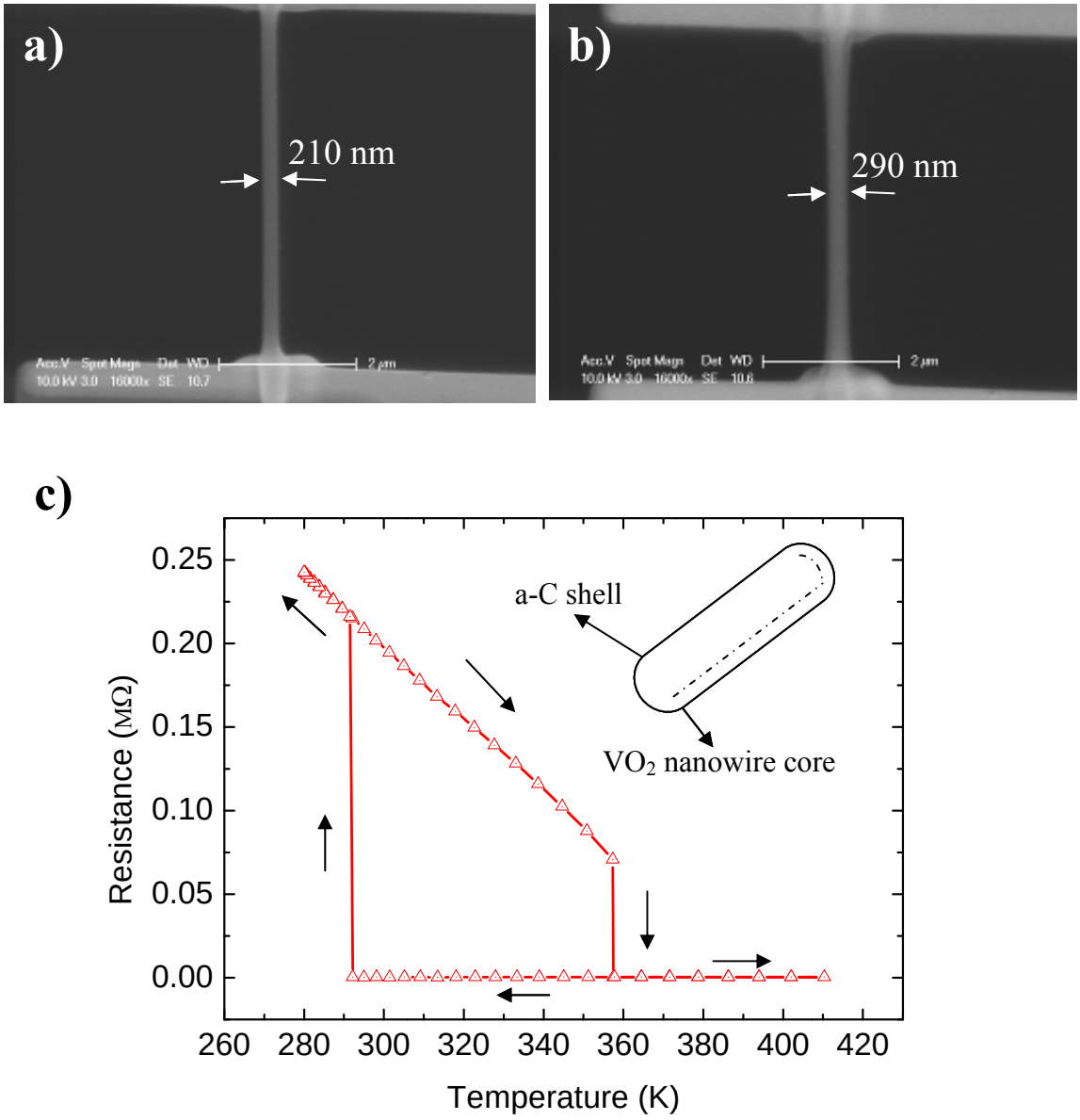

Figure 5.20: SEM images of 210 nm wide VO_2 NW before (a) and after (b) surface coating by a-C, and (c) temperature dependent electrical resistance of VO_2/a-C core/shell NW (inset: schematic sketch of core/shell NW).

5.4. Thermal conductance and thermal conductivity measurement in VO_2 NWs

In this section, we measured thermal conductivity of VO_2 NWs over a wide range of temperature to understand thermal transport in this phase transition materials. Two samples were studied in different temperature range as presented below. The

thermal conductance measurement method and thermal conductivity calculation were described in details in chapter 3. In the low temperature range, the temperature dependent thermal conductivity of 160 nm wide VO_2 NW was measured from 77 K to 300 K. Meanwhile, the thermal conductivity of 140 nm wide VO_2 NW mentioned above correlating with electrical resistance measurement was measured in the vicinity of MIT (from 300 K to 400 K).

5.4.1. Thermal conductivity in low temperature range

Figure 5.21a shows the thermal conductivity (κ) of 160 nm wide VO_2 NW as function of temperature. When temperature increases κ decreases from 11.8 W/m.K (at 77 K) to 4.3 W/m.K (at 300 K). The measured thermal conductivity in VO_2 NW is smaller than that of bulk VO_2 [33] (20 W/m.K at 77 K and 6 W/m.K at 300 K) which can be attributed to size effect. In this temperature range (from 77 K to 300 K), single crystalline VO_2 NW is totally in insulating phase (referring to temperature dependent electrical resistance curve in the inset of Figure 5.21a), hence the contribution of electrons in thermal transport is negligible. Consequently, the dependence of thermal conductivity of VO_2 NW on temperature can be explained by transportation of phonon. The reduction of κ when the temperature increases exhibits the presence of Umklapp scattering of phonons. Normally, Umklapp scattering causes the thermal conductivity varies with temperature as T^{-1} for pure bulk single crystal which was also observed in single crystal bulk VO_2 [33]. However, in our VO_2 NW the thermal conductivity drops approximately according to $\kappa \sim T^{-1.5}$ as observed in Figure 5.21b. The thermal conductivity measurement result for single crystalline VO_2 NW may indicate that besides the boundary scattering and Umklapp scattering, the scattering

from intrinsic point defects (oxygen vacancies and/or vanadium interstitials) also contribute to thermal transport.

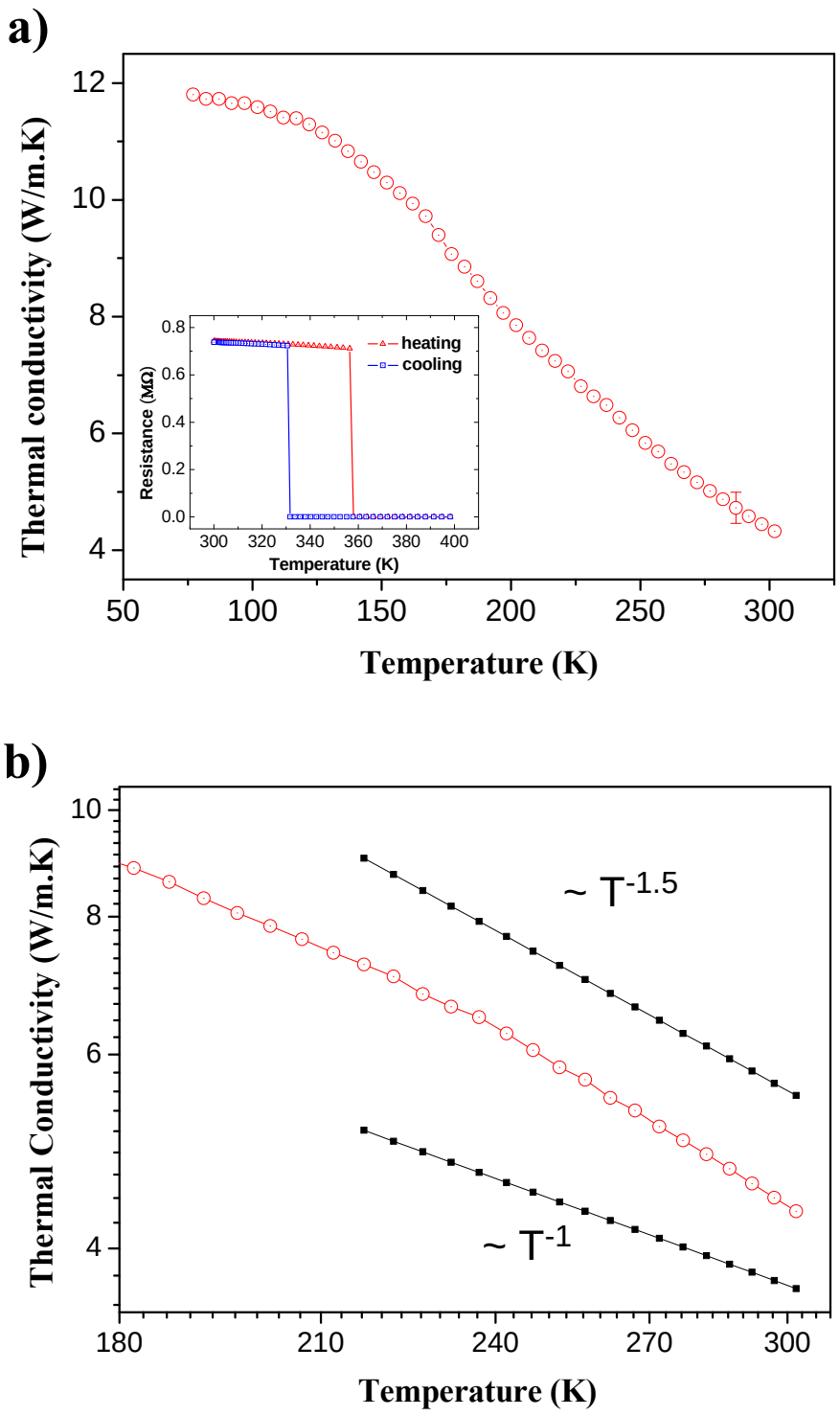

Figure 5.21: (a) Temperature dependence of thermal conductivity of the 160 nm wide VO_2 NW. Inset shows the electrical resistance as function of temperature upon heating and cooling cycle. (b) Log-log scale in temperature range from 180 K to 300 K, the two curves ~ $T^{-1.5}$ and ~ T^{-1} are shown to guide the eyes.

5.4.2. Thermal conductivity in the vicinity of MIT

Thermal transport in the 140 nm wide VO_2 NW_P studied in section 5.2 was investigated in the temperature range from 300 K to 400 K. Figure 5.22a shows the electrical resistance and thermal conductance measurements during temperature heating and cooling half cycles. The abrupt changes in electrical resistance during MIT at $T_{I\text{-}M}$ = 350 K (upon heating) and $T_{M\text{-}I}$ = 321 K (upon cooling) are characteristic of single domain behavior although the NW is now known to have pinned metallic domains; the wire will be considered as homogeneous without affecting the discussion. The correlation between thermal conductance and electrical resistance is clearly observed. Upon heating (red curve in Figure 5.22a), the thermal conductance decreases monotonically from 10.5 nW/K until $T_{I\text{-}M}$ = 350 K at which point it jumps upward from 3.71 nW/K to 4.28 nW/K corresponding to the transition in NW_P from I_P phase to M_P phase. Thereafter, the thermal conductance of NW_P in M_P phase keeps decreasing with increasing temperature and reaches a value of 2.18 nW/K at 400 K. Upon cooling, the thermal conductance tracks the heating curve until $T_{M\text{-}I}$ = 321 K at which point it jumps downward and follows the I_P phase curve. The temperature dependence of thermal conductivity of NW_P in I_P phase and M_P phase across the MIT on a log – log scale is presented in Figure 5.22b. Our observations do not follow the results previously observed in bulk VO_2 samples [33, 34]. There is a negligible change and no observable discontinuity of thermal conductivity across the MIT [34] or thermal conductivity of the metallic phase is observed smaller than that of the insulating phase [33]. Recently, it was observed that the thermal conductivity of the metallic phase is as much as 60% higher than that of the insulating phase in VO_2 thin film [35]. The value observed in our NW is ~15%. The difference may be due to the interaction between substrate and thin film in the experiment of Ref. [35] which is

certainly absent in our suspended NW, and which may affect the results significantly. The increase in thermal conductivity in VO_2 NW can be attributed to the electronic contribution to the total thermal conductivity.

The measured thermal conductance in Figure 5.22b includes both phonon contribution, G_{ph}, and electronic contribution, G_e. The electronic thermal conduction can be related to the electrical resistance by the well-known Wiedemann-Franz law [36]:

$$G_e = \frac{1}{3}\pi^2 (k/e)^2 \frac{T}{R} \tag{5.10}$$

where k is Boltzmann's constant, e is the electronic charge, and T is the absolute temperature. Using Eq. (5.10), the electronic thermal conduction, G_e, can be calculated which varies from 1.82×10^{-2} nW/K to 4.04×10^{-2} nW/K in I_P phase and from 8.8 nW/K to 13.3 nW/K in M_P phase. On the other hand, the measured total thermal conductance of the NW_P in M_P phase is less than 7 nW/K. As a result, the Wiedemann-Franz law may be invalid in our VO_2 NW_P. It is not likely that the scattering of carriers with impurities or defects in the M_P phase is dominant because such scattering is elastic and would tend to validate the Wiedemann-Franz law [36]. We suppose that the pinned metallic domains in NW may be the reasons which make the scattering process inelastic.

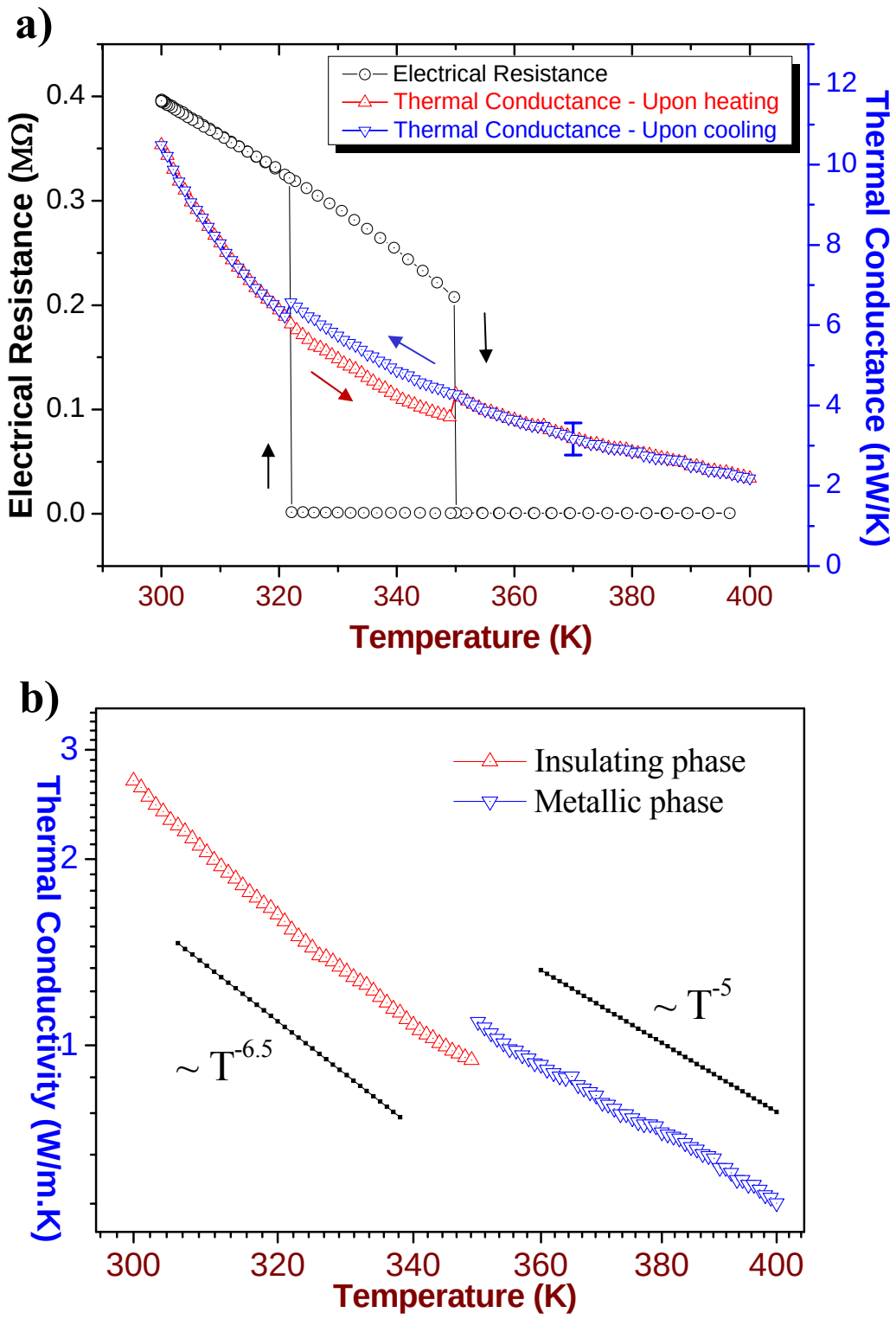

Figure 5.22: (a) Electrical resistance and thermal conductance of 140 nm wide VO_2 NW as function of temperature during heating and cooling half cycles, and (b) temperature dependent thermal conductivity of NW in I_P phase (red curve) and in M_P phase (green curve) in log – log scale, the $\sim T^{-6.5}$ and $\sim T^{-5}$ are shown to guide the eyes.

As observed in Figure 5.22b, the thermal conductivity of the NW in I_P phase decreases faster than that of the NW in M_P phase which further indicates the contribution of electrons in thermal transport. In both regimes, the thermal conductivity decreases very rapidly with increasing temperature, $\kappa \sim T^{-6.5}$ for NW in the I_P phase and $\kappa \sim T^{5}$ for NW in the M_P phase which may be caused by metallic domain pinning effect. The fast decrease of thermal conductivity is also observed in crystals free of imperfections at temperatures well below the Debye temperature in which the lattice thermal conductivity is dominant [37]. The Debye temperature for VO_2 is approximately 750 K which is well above the measured temperature range. Hence, we can conclude that the phonon contribution dominates the thermal transport in our VO_2 NW.

5.5. Summary

In summary, we have prepared single-crystalline VO_2 NWs on METS devices for electrical and thermal property measurements. The electrical resistance behavior was characterized with either uniform temperature throughout the length of the NW, or with a temperature gradient by only heating one end of the NW. In the homogeneous temperature case, the NWs exhibited single-domain behavior with the sharp transitions and hysteresis in temperature dependent electrical resistance curve during temperature cycling. On the other hand, co-existing M-I domain behavior was observed during MIT in the temperature gradient case with the resistance gradually decreasing across MIT during heating. After each measurement, the resistance of NW reduced which suggested pinned metallic domains along the NW at room temperature. Evidences of pinned metallic domains at room temperature were provided by optical

microscopy image and Raman spectroscopy. We suppose that the thermal stress in VO_2 NW (induced during temperature cycling in measurement) together with intrinsic defects (oxygen vacancies and/or vanadium interstitials) would creates pinning centres with certain pinning forces at which the metallic domains were persistently trapped and pinned. Interestingly, the NWs with pinned metallic domains still exhibit the single-domain-like behavior in the electrical resistance measurement with homogeneous temperature sweeping.

Surprisingly, the NW_P can be largely restored to the original insulating wire characteristics by applying sufficiently high tensile stress. With lower tensile stress, the metallic domains can also be released beyond a certain temperature; however the metallic domains were re-pinned in the NW upon cooling. When the tensile stress is removed, the NW returned to its pinned state. The effect of surface coating was also studied. An a-C layer was deposited on NW's surface to form VO_2/a-C core/shell NW. The resistance of core/shell NW was further reduced which indicated that more metallic domains were pinned in such wire. The temperature dependent electrical resistance of the core/shell NW showed single-domain behavior. Interestingly, the core/shell NW remained in M_P phase even at room temperature in the cooling half cycle and only turned back to I_P phase at 291 K.

Thermal conductivity, κ, in low temperature range (77K to 300 K) was measured on 160 nm wide VO_2 NW. κ decreased with temperature as $\sim T^{-1.5}$ which is faster than $\sim T^{-1}$ observed in bulk VO_2 samples. The results indicate that besides boundary scattering and Umklapp scattering, the scattering from intrinsic point defects (oxygen vacancies and/or vanadium interstitials) also contribute to thermal transport in VO_2 NW. The thermal conductivity in the vicinity of MIT was measured

on 140 nm wide VO_2 NW with pinned metallic domains. The thermal conductivity increased by about 15 % across the transition temperature at which point the NW turned from I_P phase to M_P phase. The thermal conductivity decreased very rapidly as $\kappa \sim T^{-6.5}$ for I_P phase regime and $\kappa \sim T^{-5}$ for M_P phase regime indicating the dominance of phonon thermal transport.

References

1. Chudnovskiy, F.; Luryi, S.; and Spivak, B.; "Switching Device Based on First-Order Metal-Insulator Transition Induced by External Electric Field", *Wiley-Interscience, New York*, pp. 148 – 155, 2002.

2. Kim, H. T.; Chae, B. G.; Youn, D. H.; Maeng, S. L.; Kim, G.; Kang, K. Y.; Lim, Y. S.; "Mechanism and Observation of Mott Transition in VO_2-Based Two- and Three- Terminal Devices", *New J. Phys.* Vol. 6, pp. 51 – 59, 2004.

3. Lee, M. J.; Park, Y.; Suh, D. S.; Lee, E. H.; Seo, S.; Kim, D. C.; Jung, R.; Kang, B. S.; Ahn, S. E.; Lee, C. B.; Seo, D. H.; Cha, Y. K.; Yoo, I. K.; Kim, J. S.; and Park, B. H.; "Two Series Oxide Resistors Applicable to High Speed and High Density Nonvolatile Memory", *Adv. Mater.* Vol. 19, pp. 3919 – 3923, 2007.

4. Rini, M.; Hao, Z.; Schoenlein, R. W.; Giannetti, C.; Parmigiani, F.; Fourmaux, S.; Kieffer, J. C.; Fujimori, A.; Onoda, M.; Wall, S.; and Cavalleri, A.; "Optical Switching in VO_2 Films by Below-Gap Excitation", *Appl. Phys. Lett.* Vol. 92, 181904, 2008.

5. Rakotoniaina, J. C.; Mokranitamellin, R.; Gavarri, J. R.; Vacquier, G.; Casalot, A.; and Calvarin, G.; "The Thermochromic Vanadium Dioxide: Role of Stresses and Substitution on Switching Properties", J. *Solid State Chem.* Vol. 103, pp. 81 – 94, 1993.

6. Greenberg, C. B.; "Optically Switchable Thin Films: a Review", *Thin Solid Films* Vol. 251, pp. 81 – 83, 1994.

7. Morin, F. J.; "Oxides Which Show a Metal-to-Insulator Transition at the Neel Temperature", *Phys. Rev. Lett.* Vol. 3, pp. 34 – 36, 1959.

8. Mott, N. F.; *Metal – Insulator Transistion*, 1st ed.; Taylor & Francis: New York, 1974.

9. Eyert, V.; "The Metal-Insulator Transitions of VO_2: A Band Theoretical Approach", *Ann. Phys.* (Leipzig) Vol. 11, pp. 650 – 702, 2002.

10. Biermann, S.; Poteryaev, A.; Lichtenstein, A. I.; and Georges, A.; "Dynamical Singlets and Correlation-Assisted Peierls Transition in VO_2", *Phys. Rev. Lett.* Vol. 94, 026404, 2005.

11. Donev, E. U.; Lopez, R.; Feldman, L. C.; and Haglund, R. F.; "Confocal Raman Microscopy across the Metal−Insulator Transition of Single Vanadium Dioxide Nanoparticles", *Nano Lett.* Vol. 9, pp. 702 – 706, 2009.

12. Qazilbash, M. M.; Brehm, M.; Andreev, G. O.; Frenzel, A.; Ho, P. C.; Chae, B. G.; Kim, B. J.; Yun, S. J.; Kim, H. T.; Balatsky, A. V.; Shpyrko, O. G.; Maple, M. B.; Keilmann, F.; and Basov, D. N.; "Infrared Spectroscopy and

Nano-Imaging of the Insulator-to-Metal Transition in Vanadium Dioxide", *Phys. Rev. B* Vol. 79, 075107, 2009.

13. Ramirez, J.G.; Sharoni, A.; Dubi, Y.; Gomez, M. E.; and Schuller, I. K.; "First-Order Reversal Curve Measurements of the Metal-Insulator Transition in VO_2: Signatures of Persistent Metallic Domains", *Phys. Rev. B* Vol. 79, 235110, 2009.

14. Cao, J.; Fan, W.; Zheng, H.; and Wu, J.; "Thermoelectric Effect Across the Metal−Insulator Domain Walls in VO_2 Microbeams", *Nano Lett.* Vol. 9, pp. 4001 – 4006, 2009.

15. Cao, J.; Ertekin, E.; Srinivasan, V.; Fan, W.; Huang, S.; Zheng, H.; Yim, J. M. L.; Khanal, D. R.; Ogletree, D. F.; Grossman, J. C.; and Wu, J.; "Strain Engineering and One-Dimensional Organization of Metal-Insulator Domains in Single-Crystal Vanadium Dioxide Beams", *Nat. Nanotech.* Vol. 4, pp. 732 – 737, 2009.

16. Varghese, B.; Tamang, R.; Tok, E. S.; Mhaisalkar, S. G.; and Sow, C. H.; "Photothermoelectric Effects in Localized Photocurrent of Individual VO_2 Nanowires", *J. Phys. Chem. C* Vol. 114, pp. 15149 – 15156, 2010.

17. Wu, J.; Gu, Q.; Guiton, B. S.; Leon, N. P.; Ouyang, L.; and Park, H.; "Strain-Induced Self Organization of Metal−Insulator Domains in Single-Crystalline VO_2 Nanobeams", *Nano Lett.* Vol. 6, pp. 2313 – 2317, 2006.

18. Gu, Q.; Falk, A.; Wu,J.; Ouyang, L.; and Park, H.; "Current-Driven Phase Oscillation and Domain-Wall Propagation in $W_xV_{1-x}O_2$ Nanobeams", *Nano Lett.* Vol. 7, pp. 363 – 366, 2009.

19. Wei, J.; Wang, Z.; Chen, W.; and Cobden, D. H.; "New Aspects of the Metal–Insulator Transition in Single-domain Vanadium Dioxide Nanobeams", *Nat. Nanotech.* Vol. 4, pp. 420 – 424, 2009.

20. Longo, J. M.; and Kierkegaard, P.; "A Refinement of the Structure of VO_2", *Acta Chem. Scand.* Vol. 24, pp. 420 – 426, 1970.

21. Zhang, S.; Chou, J. Y.; and Lauhon, L. J.; "Direct Correlation of Structural Domain Formation with the Metal Insulator Transition in a VO_2 Nanobeams", *Nano Lett.* Vol. 9, pp. 4527 – 4532, 2009.

22. Yang, Z.; Ko, C.; and Ramanathan, S.; "Metal-Insulator Transition Characteristics of VO_2 Thin Films Grown on Ge(100) Single Crystal", *J. Appl. Phys.* Vol. 108, 073708, 2010.

23. Verleur, H. W.; Barker, A. S.; and Berglund, C. N.; "Optical Properties of VO_2 Between 0.25 and 5 eV", *Phys. Rev.* Vol. 172, pp. 788 – 798, 1968.

24. Rosevear, W. H.; and Paul, W.; "Hall Effect in VO_2 Near the Semiconductor-to-Metal Transition", *Phys. Rev. B* Vol. 7, pp. 2109 – 2111, 1973.

25. Zhang, S.; Kim, I. S.; and Lauhon, L. J.; "Stoichiometry Engineering of Monoclinic to Rutile Phase Transition in Suspended Single Crystalline Vanadium Dioxide Nanobeams", *Nano Lett.* Vol. 11, pp. 1443 – 1447, 2011.

26. Fu, Q.; Zhang, Z. Y.; Kou, L. Z.; Wu, P.; Han, X. B.; Zhu, X.; Gao, J.; Xu, J.; Zhao, Q.; Guo, W.; and Yu, D.; "Linear Strain-Gradient Effect on the Energy Bandgap in Bent CdS Nanowires", *Nano Res.* Vol. 4(3), pp. 308 – 314, 2011.

27. Muraoka, Y.; Ueda, Y.; and Hiroi, Z.; "Large Modification of the Metal – Insulator Transition Temperature in Strained VO_2 Films Grown on TiO_2 Substrates", *J. Phys. Chem. Solids* Vol. 63, pp. 965 – 967, 2002.

28. Jin, P.; Yoshimura, K.; and Tanemura, J.; "Dependence of Microstructure and Thermochromism on Substrate Temperature for Sputter – Deposited VO_2 Epitaxial Films", *J. Vac. Sci. Technol. A* Vol. 15, pp. 1113 – 1117, 1997.

29. Pouget, J., P.; Launois, H.; Dhaenens, J., P.; Merenda, P.; and Rice, T., M.; "Electron Localization Induced by Uniaxial Stress in Pure VO_2", *Phys. Rev. Lett.* Vol. 35, pp. 873 – 875, 1975.

30. Kikuzuki, T.; and Lippmaa, M.; "Characterizing a Strain – Driven Phase Transition in VO_2", *Appl. Phys. Lett.* Vol. 96, 132107, 2010.

31. Cao, J.; Gu, Y.; Fan, W.; Chen, L. Q.; Ogletree, D., F.; Chen, K.; Tamura, N.; Kunz, M.; Barrett, C.; Seidel, J.; and Wu, J.; "Extended Mapping and Exploration of the Vanadium Dioxide Stress-Temperature Phase Diagram", *Nano Lett.* Vol. 10, pp. 2667 – 2673, 2010.

32. Tselev, A.; Budai, J. D.; Strelcov, E.; Tischler, J. Z.; Kolmakov, A.; and Kalinin, S. V.; "Electromechanical Actuation and Current-Induced Metastable States in Suspended Single-Crystalline VO_2 Nanoplatelets", *Nano Lett.* Vol. 11 (8), pp. 3065 – 3073, 2011.

33. Andreev, V. N.; Chudnovskii, F. A.; Petrov, A. V.; and Terukov, E. I.; "Thermal Conductivity of VO_2, V_3O_5, and V_2O_3", *Phys. Stat. Sol. (A)* Vol. 48, pp. K153 – K156, 1978.

34. Berglund, C. N.; and Guggenheim, H. J.; "Electronic Properties of VO_2 Near the Semiconductor-Metal Transition", *Phys. Rev.* Vol. 185, pp. 1022 – 1033, 1969.

35. Oh, D. W.; Ko, C.; Ramanathan, S.; and Cahill, D. G.; "Thermal Conductivity and Dynamic Heat Capacity Across the Metal-Insulator Transition in Thin Film VO_2", *Appl. Phys. Lett.* Vol. 96, 151906, 2010.

36. Drabble, J. R.; and Goldsmid, H. J.; **Thermal Conduction in Solids**, Pergamon Press, Inc., New York, 1961.

37. Ziman, J. M.; **Theory of Solids**, Cambridge University Press, Cambridge, England, 1964.

Chapter 6: Size and Surface Modification Dependence of Heat Transfer in Silicon Nanowires

6.1. Introduction

In the past decades, silicon nanowires (SiNWs) have been studied intensively because of their promising applications in nano-electronics, energy conversion as well as CMOS compatibility [1 – 13]. The understanding of thermal transport properties of SiNWs is also important for potential applications such as thermoelectric power generation or cooling and thermal management of electronics. In some applications, reducing the thermal conductivity of NWs is one of the requirements to enhance the performance of devices. In thermoelectric application for example, efforts have been tried to reduce the thermal conductivity whilst maintain the electrical conductivity of NWs for the figure of merit enhancement. So far, roughening the surface is an effective way to significantly diminish the thermal conductivity of SiNWs, however the level of the roughness is randomly depended on the synthesize method [11].

In this chapter, we measure the thermal conductivity of single-crystalline SiNWs of various diameters over a wide temperature range. Furthermore, we also study the effect of gallium (Ga) ion beam irradiation using FIB in modifying the surface morphology and consequently the thermal conductance of SiNWs.

6.2. Sample preparation

The single-crystalline SiNWs studied in this work were synthesized via a Vapor-Liquid-Solid (VLS) growth method. The details of NW synthesis are described elsewhere [14, 15]. The synthesized NWs have diameters in the range from several tens of nanometers to several hundred nanometers and lengths up to several tens of microns. Four SiNW samples with diameters of 86 nm, 110 nm, 230 nm and 330 nm were transferred to METS devices for thermal conductance measurement. For all samples, Pt-C composite pads were deposited at two ends of NWs by FIB deposition from a Pt precursor for thermal contact enhancement. SEM images of the prepared samples are shown in Figure 6.1. To derive the thermal conductivity, the length of suspended part of the NW between the two inner electrodes was used. The dimensions of the NWs measured by SEM are presented in Table 6.1.

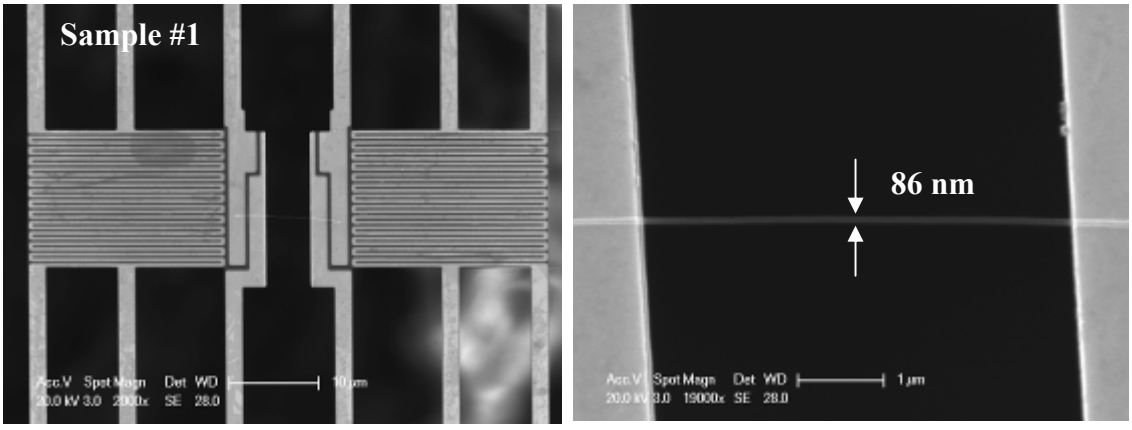

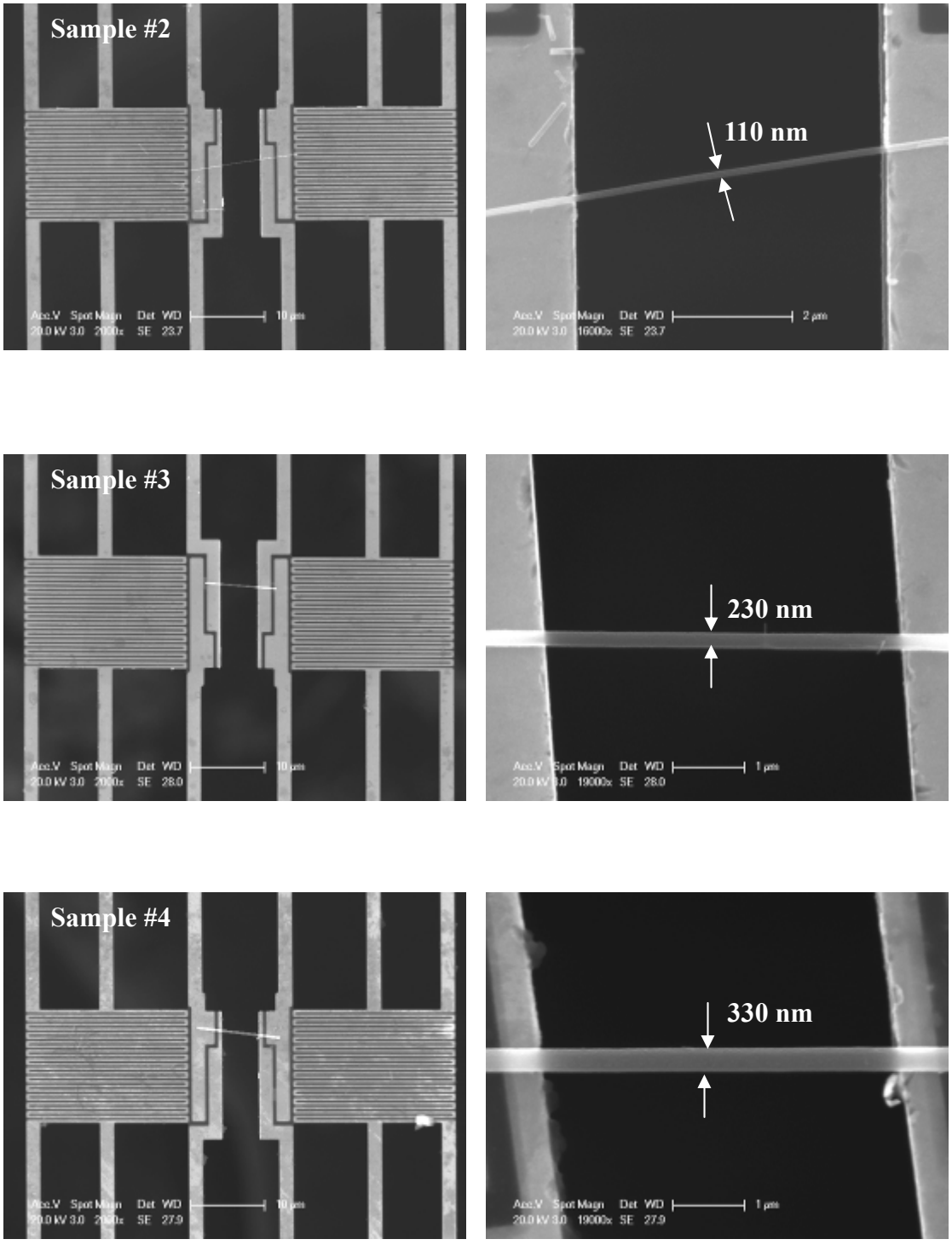

Figure 6.1: SEM images of four prepared SiNWs on METS devices for thermal conductance measurement.

Table 6.1: Dimensions of the SiNWs studied

Sample No.	Diameter (nm)	Length (μm)
#1	86	5.12
#2	110	5.27
#3	230	5.10
#4	330	5.04

6.3. Temperature dependent thermal conductivity of SiNWs

The thermal conductivities were measured from 77 K to 450 K (Figure 6.2). Compared to bulk silicon [16] (Figure 6.3), the thermal conductivities are seen to be much lower. The thermal conductivity of bulk Si increases from a small value at very low temperatures to a peak of about 5200 W/m.K at 25 K, and then decreases gradually. The thermal conductivity of bulk Si is about 140 W/m.K at room temperature. From kinetic theory, the lattice thermal conductivity can be expressed as

$$k = \frac{1}{3} C v l \tag{6.1}$$

where C, v and l are specific heat, phonon group velocity, and phonon mean free path, respectively. At low temperature, the phonon mean free path is limited by the sample size and can be regarded as a constant in bulk. Consequently, the thermal conductivity is proportional to the specific heat C, which depends on the temperature T according to Debye's law:

$$C \cong 234 N k_B (\frac{T}{\theta_D})^3 \tag{6.2}$$

where N, k_B, θ_D are total number of modes, Boltzmann constant, and Debye temperature, respectively. At 25 K, isotope scattering in the sample starts to dominate and limits the thermal conductivity value. Above 25 K, the thermal conductivity gradually decreases because the Umklapp scattering becomes progressively stronger at higher temperatures. For the NWs, we also observe similar behavior of thermal conductivity. As temperature increases the thermal conductivity initially rises to a peak and then gradually decreases. In the case of a NW, boundary scattering is important due to its small diameter. The maximum thermal conductivity values for the 86, 110, and 230 nm diameter NWs are 13.0, 18.8, and 31.9 W/m.K at 167, 170, and 179 K, respectively. Compared with the thermal conductivity of over 5000 W/m.K for bulk Si at 25 K, the peak values for the NWs studied are more than two orders of magnitude smaller. The thermal conductivity values at room temperature for 86, 110, and 230 nm diameter NWs are 8.1, 11.7, and 20.0 W/m.K, respectively. Moreover, for the NWs, the peaks occur at much higher temperatures compared to bulk Si. Table 6.2 summarizes the thermal conductivity characteristics of samples #1 to #3.

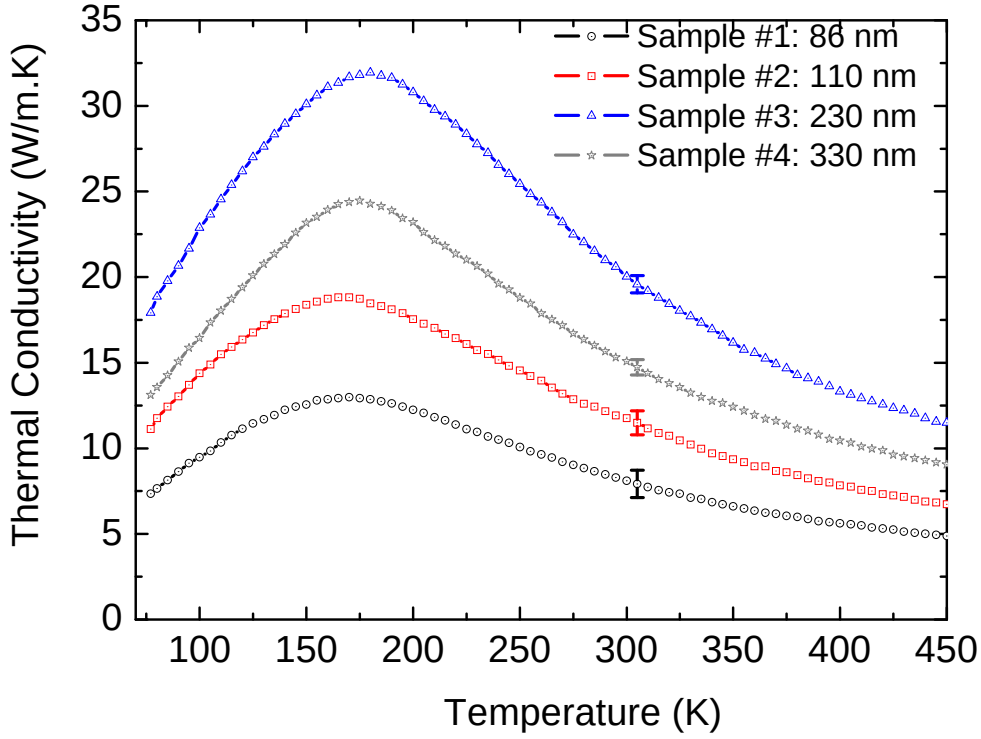

Figure 6.2: Temperature dependent thermal conductivity of four studied SiNWs.

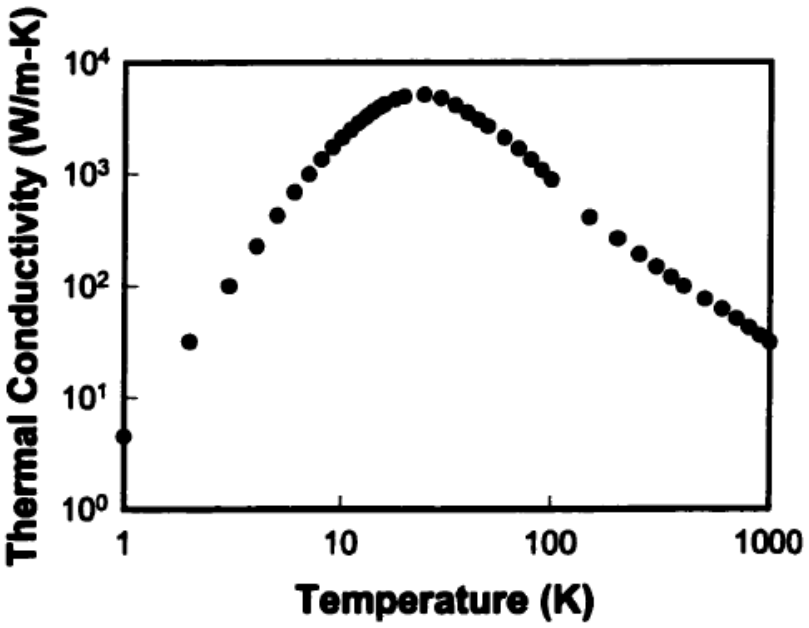

Figure 6.3: Experimental data of temperature dependent thermal conductivity of bulk Si [16].

Table 6.2: Summary of thermal conductivity at 300K, maximum thermal conductivities and corresponding temperatures for SiNW samples #1, #2, and #3.

Sample No.	Diameter (nm)	Thermal conductivity at 300K (W/m.K)	Maximum thermal conductivity (W/m.K)	Temperature of the peak value (K)
#1	86	8.1	13.0	167
#2	110	11.7	18.8	170
#3	230	20.0	31.9	179

We observed an unexpected thermal conductivity result for sample #4 with diameter of 330 nm (Figure 6.2). Normally, the thermal conductivity of a thicker NW should be higher, but the thermal conductivity of SiNW #4 is smaller than that of SiNW #3 with a diameter of 230 nm. We suspect that the contact thermal resistance is the reason for this anomalous result. For NWs with diameter less than ~ 200 nm, the thermal contact resistance of NWs bonded with Pt-C composite pads is negligible compared to the total measured thermal resistance (Chapter 4). However, for thicker NWs, the thermal contact resistance becomes increasingly significant and could reduce the total measured thermal conductance significantly. To investigate this problem, we used the SREP technique (Chapter 3) to probe the thermal resistance along SiNW #4 across the contacts. Figure 6.4 shows the SEM image of SiNW #4 bonded by Pt-C pads with the thermal resistance profile along the NW superimposed. As inferred from Figure 6.4, the total thermal resistance of SiN_x membrane and contact is ~ 2×10^6 (K/W) which is comparable to the thermal resistance of suspended part of the NW. As a result, the measured thermal resistance is much higher than the actual resistance of NW itself which leads to lower measured thermal conductance, and consequently lower measured thermal conductivity.

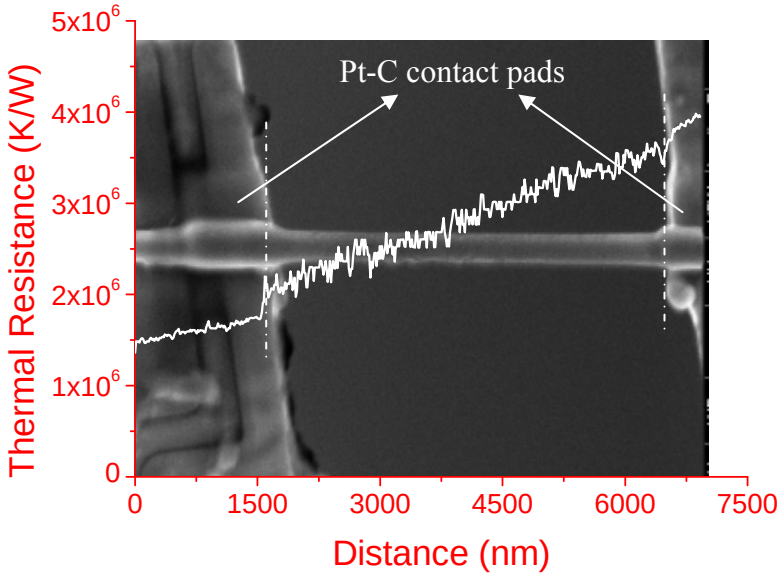

Figure 6.4: SEM image of 330 nm diameter SiNW (sample #4) bonded by Pt-C pads and thermal resistance profile along the NW length obtained by SREP technique.

The thermal conductivities of samples #1, #2, and #3 as function of temperature in low and high temperature ranges are plotted on a log–log scale in Figure 6.5. In the low temperature range (77 to 120 K) the thermal conductivity scales approximately linearly with temperature for all samples which deviates from the Debye T^3 law. On the other hand, in the high temperature range (260 to 450 K) the thermal conductivity decreases with temperature approximately close to $T^{-1.5}$. The observation of temperature dependent thermal conductivities of NWs in the low temperature range is similar to results reported for thin SiNWs with various diameters [17], but over a lower temperature range (20 to 100K). This phenomenon is not a result of ballistic and quantized phonon transport in 1-D channels [17, 18].

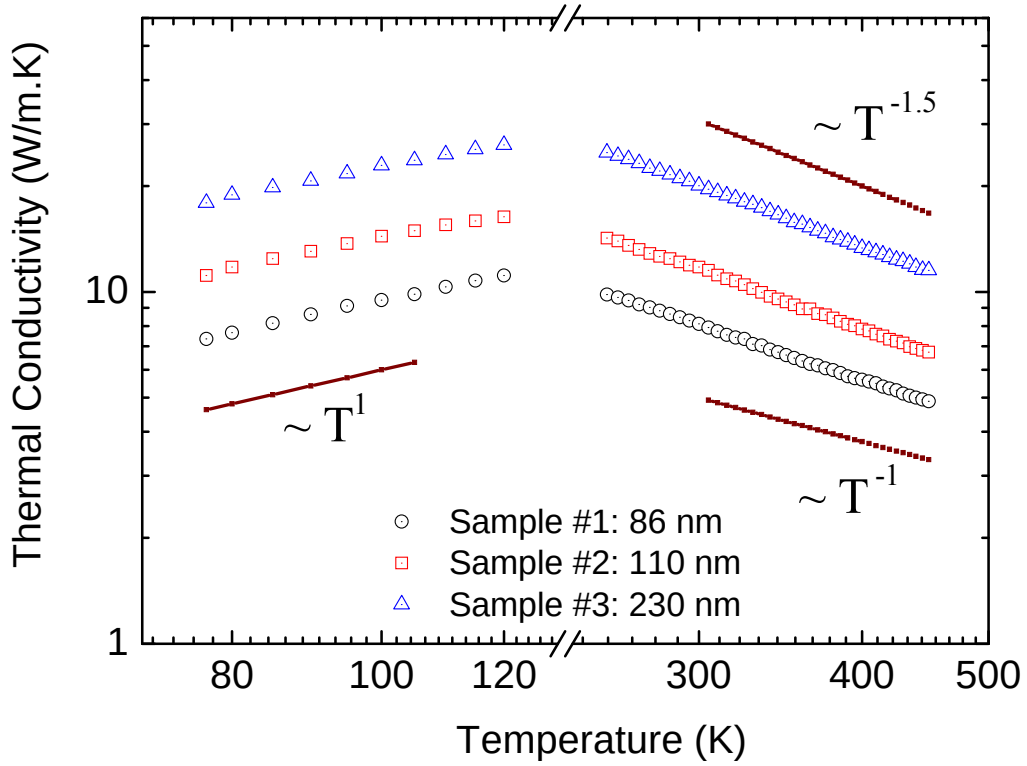

Figure 6.5: Thermal conductivity of SiNW sample #1, #2, and #3 as function of temperature in log-log scale, the curves ~ T^{1}, T^{-1}, and $T^{-1.5}$ are shown to guide the eyes.

The deviation from Debye law observed in all NW samples at low temperature indicates that besides phonon boundary scattering, some other effects could play important roles. The frequency-dependent scattering model has been employed to explain the linear dependence of thermal conductance on temperature at low temperature for thin SiNWs [17]. At low temperature, there is a competition between two phonon transmission regimes: the specularly scattered modes which give a mean free path that scales according to ω^{-4}, and the other modes which have mean free path of d (NW's diameter). The contribution from the sum of the two phonon groups results in the linear temperature dependence of thermal conductance at low temperature. Although this model was suggested to be valid for sufficiently thin NWs

(less than 60 nm) for which the contribution from the specularly scattered modes is significant [17], we believe that the model can be applied to thicker SiNWs (up to ~ 200 nm as observed in our experiments – Figure 6.5).

Interestingly, in the high temperature region the thermal conductivity drops approximately as ~ $T^{-1.5}$ which is faster than the pure Umklapp scattering trend in bulk crystal (~ T^{-1}). The steeper dependence of thermal conductivity on temperature can be attributed to isotope scattering. This observation is also close to the Callaway model's prediction for lattice thermal conductivity [19].

6.4. Size dependent thermal conductivity of SiNWs

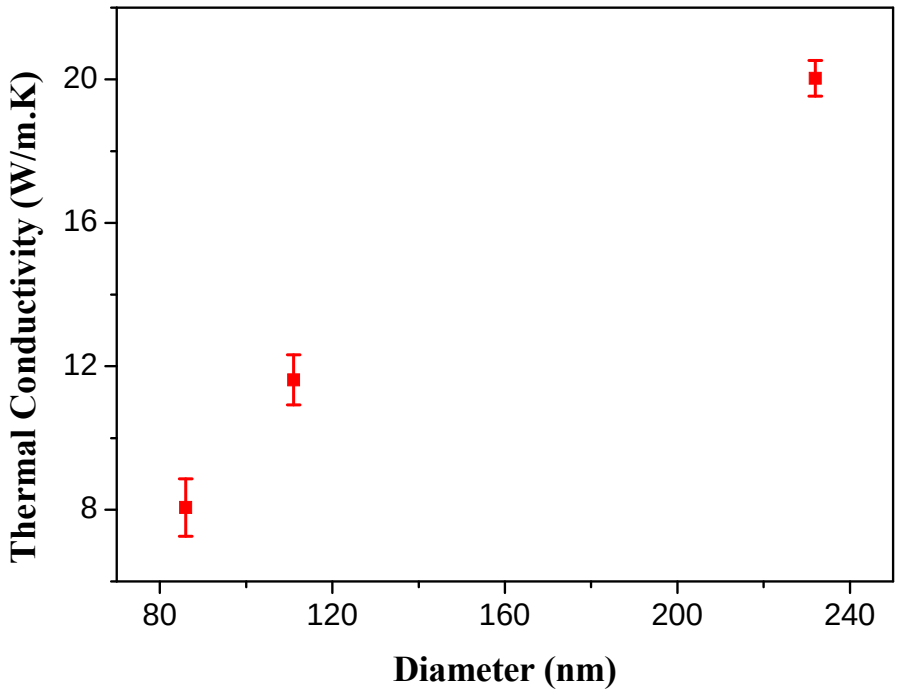

Figure 6.6: Thermal conductivity of SiNW as a function of diameter at room temperature.

The dependence of thermal conductivity on the diameter of SiNWs is shown in Figure 6.6. Since boundary scattering is stronger in thinner NW, the thermal conductivity decreases with decreasing diameter. From our experimental results, the thermal conductivity decreases from ~20.0 to ~8.1 W/m.K corresponding to a decrease in diameter from 240 to 86 nm. In this diameter range, the slope extracted from the curve in Figure 6.6 is ~ 7.7×10^6 ($W/m^2.K$) which is close to the value (8.1×10^6 $W/m^2.K$) reported in SiNWs using Monte Carlo simulation for the same diameter range [6].

6.5. Effect of focused ion beam (FIB) irradiation on thermal conductance and surface morphology of SiNWs

In order to reduce the thermal conductivity of NWs, modifying the wire's surface morphology is one of the effective ways. We exposed sample #1 (86 nm diameter), and sample #3 (230 nm diameter) to a 30keV gallium (Ga) ion beam using a FIB. After an initial thermal conductance measurement, each NW was exposed with cumulative doses of ions between measurements. The exposure experiment was performed under the defocused beam with following conditions: ion beam energy of 30 keV, the ion current of 10 pA, and the dwell-time of 0.3 μs. Figure 6.7 shows the temperature dependent thermal conductance of the SiNWs before and after FIB exposure at different ion beam doses.

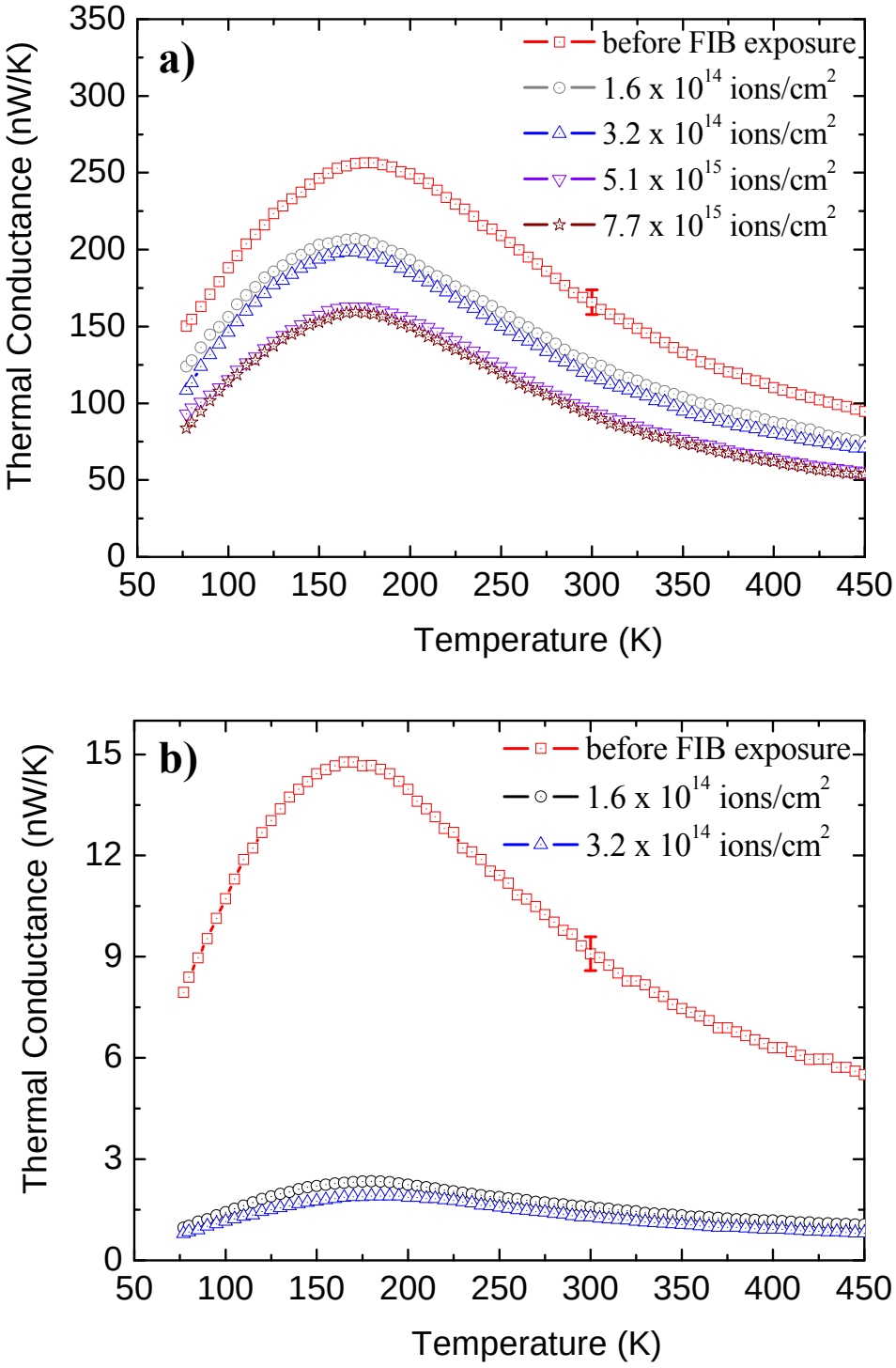

Figure 6.7: Thermal conductance of (a) 230 nm and (b) 86 nm diameter SiNWs measured before and after FIB exposure with different doses.

For the thicker SiNW (230 nm in diameter, Figure 6.7a), the overall thermal conductance of wire decreases significantly with increasing dose level up to 7.7×10^{15}

ions/cm^2. The qualitative temperature dependence is not affected – the thermal conductance first increases and then decreases after reaching the peak at around 170 K for all dose levels. In contrast, for the thinner SiNW (86 nm in diameter, Figure 6.7b), the thermal conductance of wire decreases dramatically even with a relatively low dose of 1.6×10^{14} ions/cm^2. The results reveal that the crystal nature was mostly vanished in NW even with low dose level. It has been observed that the surface of silicon was damaged and turned to the amorphous form under ion bombardment [20 – 23]. The mechanism responsible for the damage can be understood as following. In irradiation, the energetic ions penetrate the silicon surface; they suffer elastic collisions with the lattice atoms which lead to atomic displacements. These displaced atoms can initiate their own sequences of collisions which creates the collision cascade. With high enough energy of incident ions the damage will occur in the form of defects, dislocations or amorphous regions within the cascade volume. It is clear that the heterogeneous nucleation of damage can occur around the track of the incident ions. The depth of induced amorphous layer depends on the energy and dose level of the incident ion beam. Figure 6.8 shows the dependence of thermal conductance of (a) 230 nm and (b) 86 nm diameter SiNWs on dose levels at 300 K. From Figure 6.8a, the thermal conductance of the thicker wire declines rapidly from 175 nW/K and almost reaches an asymptotic value of 90 nW/K at 7.7×10^{15} ions/cm^2.

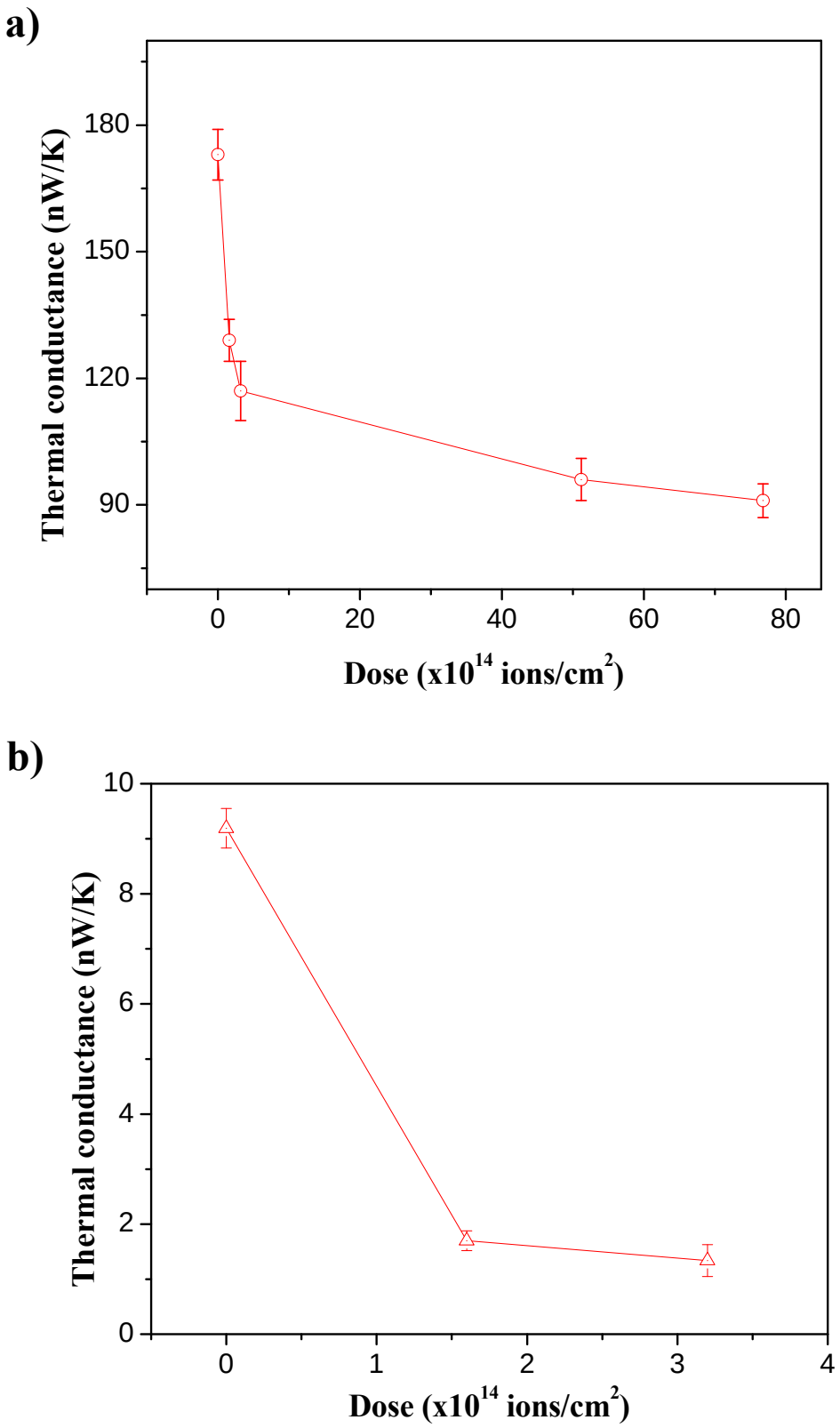

Figure 6.8: Thermal conductance as function of dose level at 300 K of (a) 230 nm and (b) 86 nm diameter SiNWs.

On the other hand, the thermal conductance of thin wire reaches saturation even at a low dose of 1.6×10^{14} ions/cm^2 (Figure 6.8b). The reduction of thermal conductance can be attributed to two reasons: the shrinkage of the crystalline core due to creation of an amorphous layer on the surface, and phonon scattering at the amorphous shell – crystalline core interface. The higher the dose level is the thinner the crystalline core becomes hence the thermal conductance decreases significantly. However, the fact that the conductance saturates beyond a certain dose level indicates that the depth of the amorphous region is ultimately not determined by the dose. The collision cascade and the formation of damaged regions are simulated using the Stopping and Range of Ions in Matter (SRIM) software. Figure 6.9a shows the Ga ion trajectory (red curve) and the damaged region (green curve) in silicon at different dose levels. The depth of damaged region increases from ~53 nm to ~83 nm as the dose increases from 1.6×10^{14} ions/cm^2 to 7.7×10^{15} ions/cm^2 but does not change significantly beyond this dose. For the 230 nm diameter wire for example, the portion of crystalline core under high dose ion beam irradiation remains relatively large (~ 2/3 of wire's volume). Hence the behavior of thermal conductance of irradiated NWs with temperature is that of pure crystalline NWs as observed in Figure 6.7a. Whilst for the thinner wire (diameter of 86 nm) the entire NW was mostly damaged. Consequently, the thermal conductance decreased dramatically as observed in Figure 6.7b. Figure 6.9b shows the schematic sketches of the portion of damaged region in thin and thick irradiated NWs with the same dose.

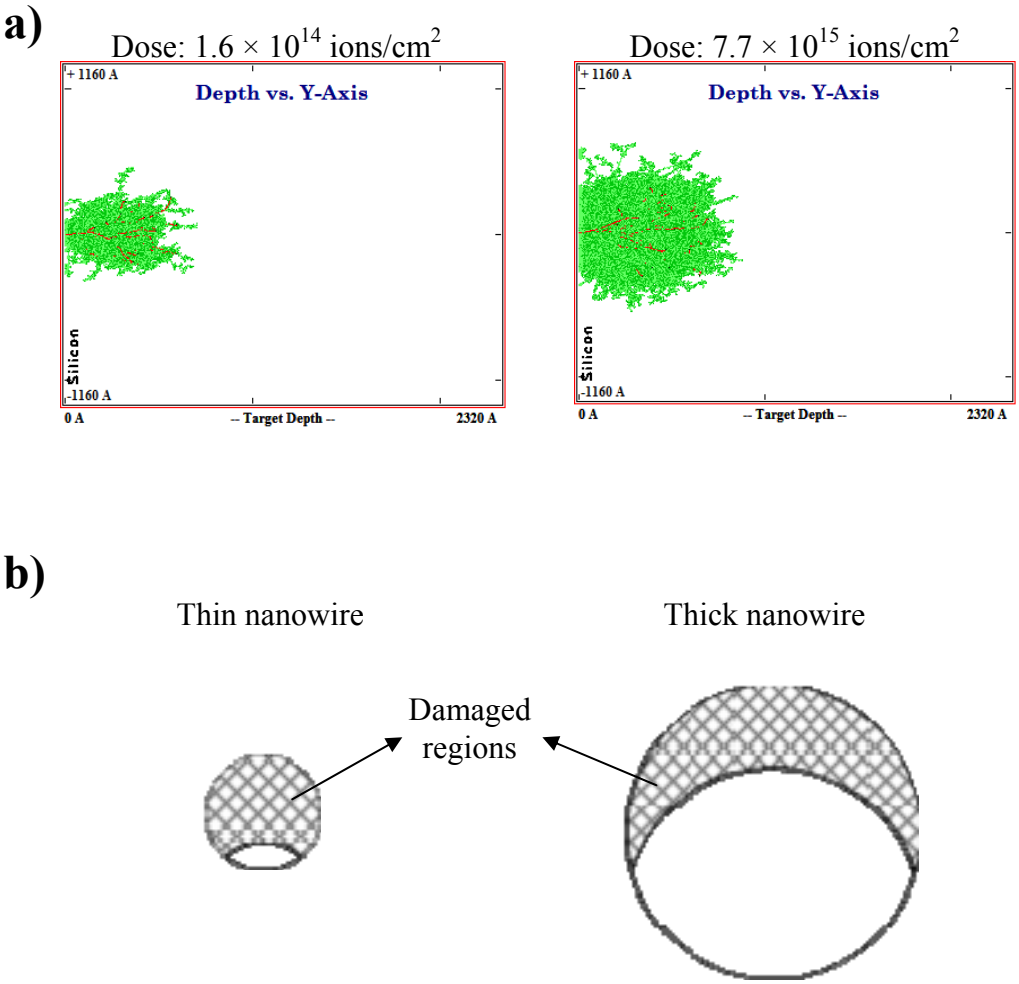

Figure 6.9: (a) The SRIM simulation of the Ga ion trajectory (red curve) and the damage cascades (green curve) in silicon under ion beam irradiation with different doses, and (b) schematic sketches of the portion of damaged region in thin and thick SiNWs with the same dose.

To further elucidate the morphology of the irradiated SiNWs, cross-sectional TEM images were taken. A new batch of SiNWs was dispersed on SiO_2/Si substrate and was exposed to Ga ion beam at selected areas. The substrate with irradiated SiNWs was then cut in thin lamellae using FIB such that the cutting planes were perpendicular to the SiNWs. Finally, the thin lamellae were transferred to a Cu grid for TEM imaging. A schematic of the substrate lamella with a cross-section of the SiNWs is shown in Figure 6.10a, in which a-C layers were deposited for wire

protection during lamella etching. Figure 6.10b shows a TEM image of the lamella with some SiNWs on the top surface. The SiNWs in dash-dotted rectangle on the left hand side of Figure 6.10b were exposed to FIB irradiation at a dose of 8×10^{14} ion/cm^2. Meanwhile, the dose applied to the SiNWs in dash-dotted rectangle on the right hand side was 3×10^{15} ion/cm^2.

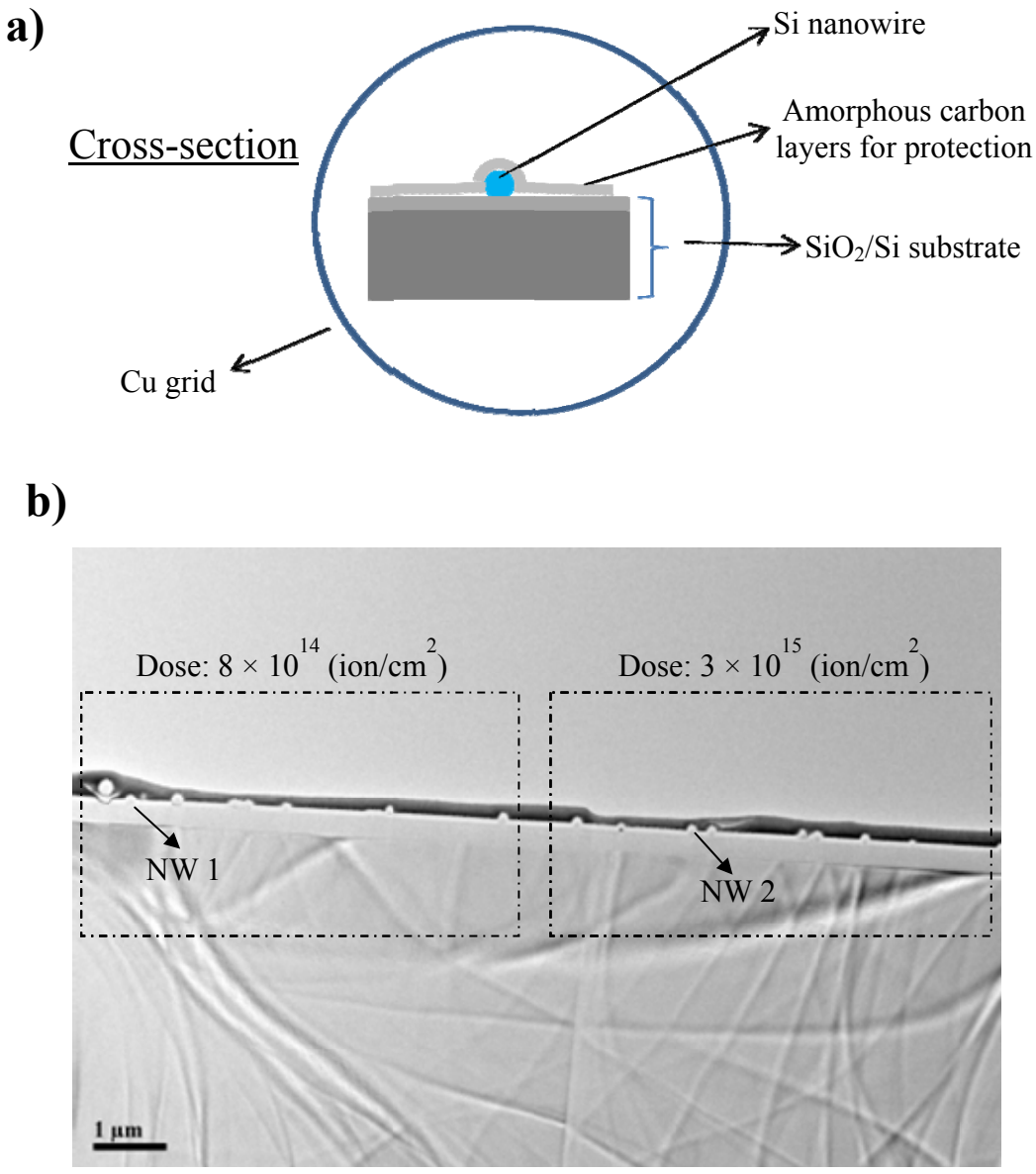

Figure 6.10: (a) The sketch of the substrate lamella with cross-sectional surface of SiNWs, and (b) a TEM image of such lamella with some SiNWs on top surface.

The cross-sectional TEM images of SiNWs in exposed region with low (NW 1) and high (NW 2) ion beam dose of 8×10^{14} and 3×10^{15} ion/cm^2 are shown in Figures 6.11 a and b, respectively. It is clearly observed that, with high ion dose, most of the irradiated NW cross-section turned to amorphous silicon (a-Si) and only small part of NW remained crystalline (c-Si) (Figure 6.11b). The lattice structure of remaining crystalline part in Figure 6.11b is clearly seen in the high magnification TEM image (Figure 6.12). The interface separating the amorphous zone and crystalline zone is not sharply defined but is graded from a structured lattice to a disordered morphology. This can be understood by considering the endpoint of the ion trajectory where the concentration of displaced atoms (point defects) is lower than a critical value at which the damaged crystal can transform to amorphous phase. It had been shown that heavily damaged crystalline silicon transforms to an amorphous state when about 10% of the atoms have been displaced from their lattice sites [20]. Such the transition interface between amorphous and crystalline regions might be an effective phonon scattering boundary that can significantly reduce the thermal conductance of irradiated SiNWs, especially for thin wires.

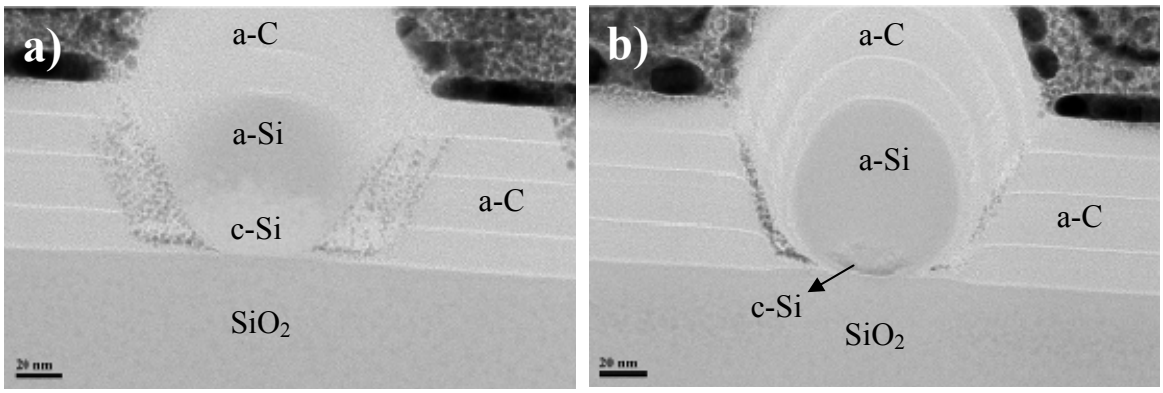

Figure 6.11: Cross-sectional TEM images of irradiated SiNW with (a) low ion beam dose of 8×10^{14} ion/cm^2, and (b) high ion beam dose of 3×10^{15} ion/cm^2.

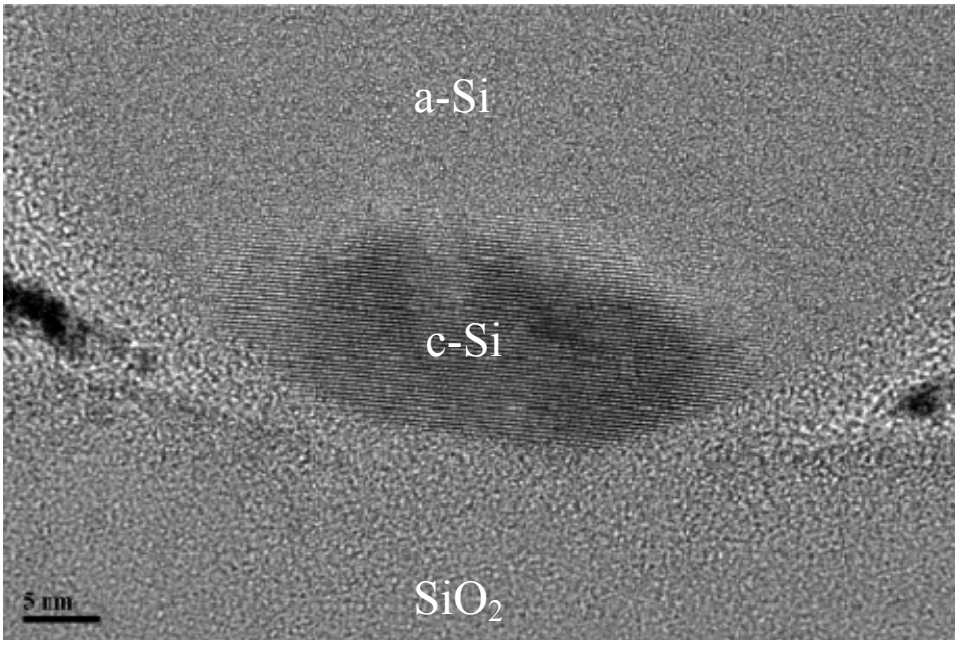

Figure 6.12: High magnification TEM image of remained crystalline part of irradiated SiNW with high ion beam dose of 3×10^{15} ion/cm^2.

6.6. Summary

The thermal conductivities of SiNWs of various diameters were measured over a range of temperature spanning 77 to 450 K. The thermal conductivity first increases with temperature and then decreases after reaching a maximum at a certain temperature T_{peak}. In the low temperature range (from 77 to 120 K) the thermal conductivity increases almost linearly with temperature, with is a significant deviation from Debye's law ($\sim T^3$). On the other hand, in the high temperature range beyond T_{peak} the thermal conductivity decreases approximately as $\sim T^{-1.5}$. Furthermore the dependence of thermal conductivity on the diameter of SiNWs has been investigated, and it was found that the thermal conductivity decreases significantly as the diameter shrinks, which indicates the dominance of boundary scattering in thin wires.

The thermal conductance of SiNWs decreases dramatically after exposure to

Ga ion irradiation. The thermal conductance of NWs decreases as the ion dose increases and reaches a saturated value at a certain dose level. SRIM simulation results and TEM images show that an amorphous region was created in irradiated SiNWs due to the collision cascade between the incident ions and the lattice atoms. The severe reduction in the thermal conductance is attributed to the shrinkage of the crystalline part of the SiNW and the phonon boundary scattering at the amorphous – crystalline interface.

References

1. Li, D.; Wu, Y.; Kim, P.; Shi, L.; Yang, P.; and Majumdar, A.; "Thermal Conductivity of Individual Silicon Nanowires", *Appl. Phys. Lett.* Vol. 83, pp. 2934 – 2936, 2003.

2. Li, D.; Wu, Y.; Fan, R.; Yang, P.; and Majumdar, A.; "Thermal Conductivity of Si/SiGe Superlattice Nanowires", *Appl. Phys. Lett.* Vol. 83, pp. 3186 – 3188, 2003.

3. Volz, S. G.; and Chen, G.; "Molecular Dynamics Simulation of Thermal Conductivity of Silicon Nanowires", *Appl. Phys. Lett.* Vol. 75, pp. 2056 – 2058, 1999.

4. Zou, J.; and Balandin, A.; "Phonon Heat Conduction in a Semiconductor Nanowire", J. Appl. Phys. Vol. 89, pp. 2932 – 2938, 2001.

5. Mingo, N.; "Calculation of Si Nanowire Thermal Conductivity Using Complete Phonon Dispersion Relations", *Phys. Rev. B* Vol. 68, 113308, 2003.

6. Chen, Y.; Li, D.; Lukes, J. R.; and Majumdar, A.; "Monte Carlo Simulation of Silicon Nanowire Thermal Conductivity", *J. Heat Trans.* Vol. 127, pp. 1129 – 1137, 2005.

7. Ponomareva, I.; Srivastava, D.; and Menon, M.; "Thermal Conductivity in Thin Silicon Nanowires: Phonon Confinement Effect", Nano Lett. Vol. 7, pp. 1155 – 1159, 2007.

8. Shi, L. H.; Yao, D. L.; Zhang, G.; and Li, B.; "Large Thermoelectric Figure of Merit in $Si_{1-x}Ge_x$ Nanowires", Appl. Phys. Lett. Vol. 96, 173108, 2010.

9. Yang, N.; Zhang, G.; and Li, B.; "Violation of Fourier Law of Heat Conduction in Nanowire", *Nano Today* Vol. 5, pp. 85 – 90, 2010.

10. Zhang, G.; Zhang, Q. X.; Bui, C. T.; Lo, G. Q.; and Li, B.; "Thermoelectric Performance of Silicon Nanowires", Appl. Phys. Lett. Vol. 94, 213108, 2009.

11. Hochbaum, A. I.; Chen, R.; Delgado, R. D.; Liang, W.; Garnett, E. C.; Najarian, M.; Majumdar, A.; and Yang, P.; "Enhanced Thermoelectric Performance of Rough Silicon Nanowires", Nature Vol. 451, pp. 163 – 167, 2008.

12. Cui, Y.; and Lieber, C. M.; "Functional Nanoscale Electronic Devices Assembled Using Silicon Nanowire Building Blocks", *Science* Vol. 291, pp. 851 – 853, 2001.

13. Boukai, A. I.; Bunimovich, Y.; Tahir-Kheli, J.; Yu, J. K.; Goddard, W. A.; and Heath J. R.; "Silicon Nanowires as Efficient Thermoelectric Materials", *Nature* Vol. 451, pp. 168 – 171, 2008.

14. Whang, S. J.; Lee, S. J.; Yang, W. F.; Cho, B. J.; Liew, Y. F.; and Kwong, D. L.; "Complementary Metal-Oxide-Semiconductor Compatible Al-Catalyzed Silicon Nanowires", *Electronchem. Solid State Lett.* Vol. 10, pp. E11 – E13, 2007.

15. Yang, W. F.; Lee, S. J.; Liang, G. C.; Eswar, R.; Sun, Z. Q.; Kwong, D. L; "Temperature Dependence of Carrier Transport of a Silicon Nanowire Schottky-Barrier Field-Effect Transistor", *IEEE Trans. Nanotech.* Vol. 7, pp. 728 – 732, 2008.

16. Touloukian, Y. S.; **Thermophysical Properties of Matter**, 1970, New York, IFI/Plenum, Vol.2, 1970.

17. Chen, R.; Hochbaum, A. I.; Murphy, P.; Moore, J.; Yang, P.; and Majumdar, A.; "Thermal Conductance of Thin Silicon Nanowires", *Phys. Rev. Lett*. Vol. 101, 105501, 2008.

18. Schwab, K.; Henriksen, E. A.; Worlock, J. M.; and Roukes, M. L.; "Measurement of the Quantum of Thermal Conductance", *Nature* (London) Vol. 404, pp. 974 – 977, 2000.

19. Callaway, J.; "Model for Lattice Thermal Conductivity", *Phys. Rev.* Vol. 113, pp. 1046 – 1051, 1958.

20. Washburn, J.; Murty, C. S.; Sadana, D.; Byrne, P.; Gronsky, R.; Cheung, N.; and Kilaas, R.; "The Crystalline to Amorphous Transformation in Silicon", *Nucl. Instr. Methods* Vol. 209/210, pp. 345 – 350, 1983.

21. Holland, O. W.; Fathy, D.; Narayan, J.; and Oen, O. S.; "Dose Rate Effects in Silicon during Heavy Ion Irradiation", *Nucl. Instrum. Methods Phys. Res.* Vol. B10/11, pp. 565 – 568, 1985.

22. Bischoff, L.; Teichert, J.; and Hausmann, S.; "Dwell-Time Dependence of Irradiation Damage in Silicon", *Nucl. Instrum. Methods Phys. Res.* Vol. B178, pp. 165 – 169, 2001.

23. Titov, A. I.; Belyakov, V. S.; and Azarov, A. Y.; "Formation of Surface Amorphous Layers in Semiconductors under Low-Energy Light-Ion Irradiation: Experiment and Theory", *Nucl. Instrum. Methods Phys. Res.* Vol. B212, pp. 169 – 178, 2003.

Chapter 7: Conclusions and Future Work

In this thesis, we have conducted experimental studies of thermal transport in various kinds of nanowires (NWs) to elucidate phonon transport in quasi one-dimensional nanostructures. The electrical and thermal properties and the interesting correlation between them in metal-insulator-transition VO_2 NWs were also studied in the vicinity of the transition temperature. All the measurements were performed using a home-made measurement set-up and micro-electro-thermal system (METS) devices.

METS devices with different configuration were fabricated on SOI wafers using photolithography patterning with high resolution masks. The fabricated METS device consists of two suspended membrane-islands with Pt coil patterns. The Pt coils could serve as a heater to increase the temperature and/or resistance thermometer to monitor the temperature change in the membrane-islands. Individual NWs were picked up and placed between two adjacent suspended membranes using a tungsten tip mounted on a nano-manipulator. Pt pads were deposited at the NW-electrode contacts by electron beam induced deposition in a dual beam FIB to reduce both thermal contact resistance and electrical contact resistance in the thermal and electrical measurements. The experimental set-up and measurement schemes were developed which make it possible to simultaneously measure the thermal, electrical conductance, and the thermoelectric power coefficient of the NW samples.

Thermal conductivities of individual single crystalline ZnO NW with diameters of 70, 84, 120, 166, and 209 nm were measured over a temperature range of 77 – 400K. The measured thermal conductivities of the ZnO NWs are more than one order of magnitude lower than that of bulk ZnO. With decreasing diameter, the

corresponding thermal conductivity is reduced over the entire measured temperature range due to phonon boundary scattering. It is found that the thermal conductivity is approximately linear with the cross-sectional area of the NWs in the measured diameter range. The temperature for the peak in thermal conductivity is between 120 and 150 K, which is much higher than the corresponding temperature for the bulk ZnO. The results show that boundary scattering is dominant until the peak temperature, and Umklapp scattering, which reduces the thermal conductivity with temperature, becomes important and comes to dominate at higher temperature. Beyond the peak temperature, the thermal conductivity decreases with temperature as T^{α}, with α in the range of 1.42 – 1.49, indicating strong impurity scattering (including isotope scattering) and Umklapp scattering at intermediate and high temperatures. The thermal conductivities of the ZnO NWs are found to be insensitive to the surface a-C coating but greatly degraded by ion irradiation at even low dose. Further experiments for greater insight into impurity (isotope) scattering in ZnO NWs should be carried out. Measurements could be carried out on ZnO NWs synthesized with different isotopes. The isotope disorder in ZnO NWs might affect the thermal conductivity dramatically.

The experimental results of both thermal and electrical properties of single crystalline VO_2 NWs have shown many interesting phenomena in the vicinity of metal-insulator-transition (MIT) temperature. For studies conducted where the temperature along the NW is uniform, the NWs exhibit single domain behavior with sharp hysteresis in the temperature dependent electrical resistance curve. On the other hand, with a temperature gradient is created between two ends of NW, co-existing M-I domains were observed during the metal-insulator transition. The reduction in electrical resistance after several measurements with temperature cycling at one side

of the NW indicates that the metallic domains were pinned inside the NW even at low temperature. We postulate that the thermal stress in VO_2 NW (induced during temperature cycling in measurement) together with intrinsic defects (oxygen vacancies and/or vanadium interstitials) create pinning centre with certain pinning forces at which the metallic domains were persistently trapped and pinned. Interestingly, a strong external tensile stress applied uniaxially to the NW can mostly recover the resistance, which indicates that the pinned metallic domains have been released. The decoupling between thermal stress and the defects by applying external tensile stress might be the reason for such a recovery phenomenon. However, more measurements need to be carried out *in situ* under a high resolution optical microscope or TEM in order to find out what exactly happens in the pinning and recovery phenomena. Thermal conductance measurements in the low temperature range (77 – 300 K) for 160 nm wide VO_2 NW showed that the thermal conductivity of that NW decreases approximately with temperature as $\sim T^{-1.5}$ over the whole temperature range. The thermal conductivity measured on 140 nm wide VO_2 NW with pinned metallic domains increases by about 15% across the MIT temperature which is different from that observed in bulk VO_2, the latter showing minimal changes

We have measured the thermal conductivity of Si NWs with diameters of 86, 110, and 230 nm over the temperature range of 77 – 450 K. The thermal conductivity scales linearly with temperature in the temperature range of 77 K to 120 K, which is opposed to the T^3 dependence predicted by Debye's model for phonon transport. Meanwhile, in the high temperature range beyond the peak temperature, the thermal conductivity decreases approximately with temperature as $T^{-1.5}$. The thermal conductivity decreases significantly for smaller diameter, which indicates strong boundary scattering in thin wires. Under ion beam irradiation, an amorphous region

was created on the surface of the NW due to the collision cascade between the incident ions and the lattice atoms. We observed significant reduction of thermal conductance of the wires, which is attributed to the shrinkage of the crystalline part of the NW and the enhanced phonon boundary scattering at the amorphous – crystalline interface. It is worth carrying out the experiment for highly doped p- or n-type Si NWs. In which by applying the ion beam irradiation method, one can dramatically reduce the thermal conductivity of highly-doped Si NWs. Meanwhile, the electrical conductivity might not be changed much because the mean free path of electrons is much smaller than that of phonons. Consequently, the figure of merit of NWs could be enhanced for thermoelectric applications.

Furthermore, fabrication and study electrical and thermal transport of very thin ZnO, Si, and VO_2 NWs with diameters in the range of 5 – 20 nm should be carried out. At such small scale, anomalous phenomena in thermal transport such as quantized thermal conductance might be observed.

Appendix A: ZnO NW synthesis

The ZnO NWs used in this study were synthesized via a vapor transport process [A.1] in a sealed horizontal tube furnace (Carbolite CTF 12/75/700). ZnO (99.99%, Aldrich) and graphite (< 20 μm, synthetic, Aldrich) powders in a weight ratio of 1:1 were thoroughly ground in a mortar and 0.40 g of the powder mixture was placed at the bottom of a one-end-closed small quartz tube. Si (100) wafers pre-deposited with a 200 nm ZnO seed layer using RF magnetron sputtering (Denton Discovery 18) were used as substrates and were placed nearer to the open end of the quartz tube. The small quartz tube was then inserted into a large alumina work tube; such that the closed end containing the powder mixture was at the centre of heating zone, and the open end faced gas in-flow. The furnace was initially evacuated to a base pressure of 2.0×10^{-2} mbar, before Ar carrier gas mixed with 0.25% O_2 by volume at a total flow rate of 80 sccm was passed. The pressure in the alumina work tube was then raised to 2.0 mbar by partially closing a backing valve. The furnace was heated up to 900^0C within 40 min and kept at that temperature for 30 minutes for ZnO NW growth. The local temperature at the Si substrate during growth was approximately 800^0C. Upon completion, the furnace was allowed to cool down to room temperature and the Si wafer covered with ZnO NWs was taken out for analysis. The growth setup and furnace heating process are shown in Figure A.1a and Figure A.1b, respectively. Side-view imaging of the as-grown NW arrays revealed that the ZnO NWs generally grew upwards from the substrate with an average length of 25 μm as shown in Figure A.2.

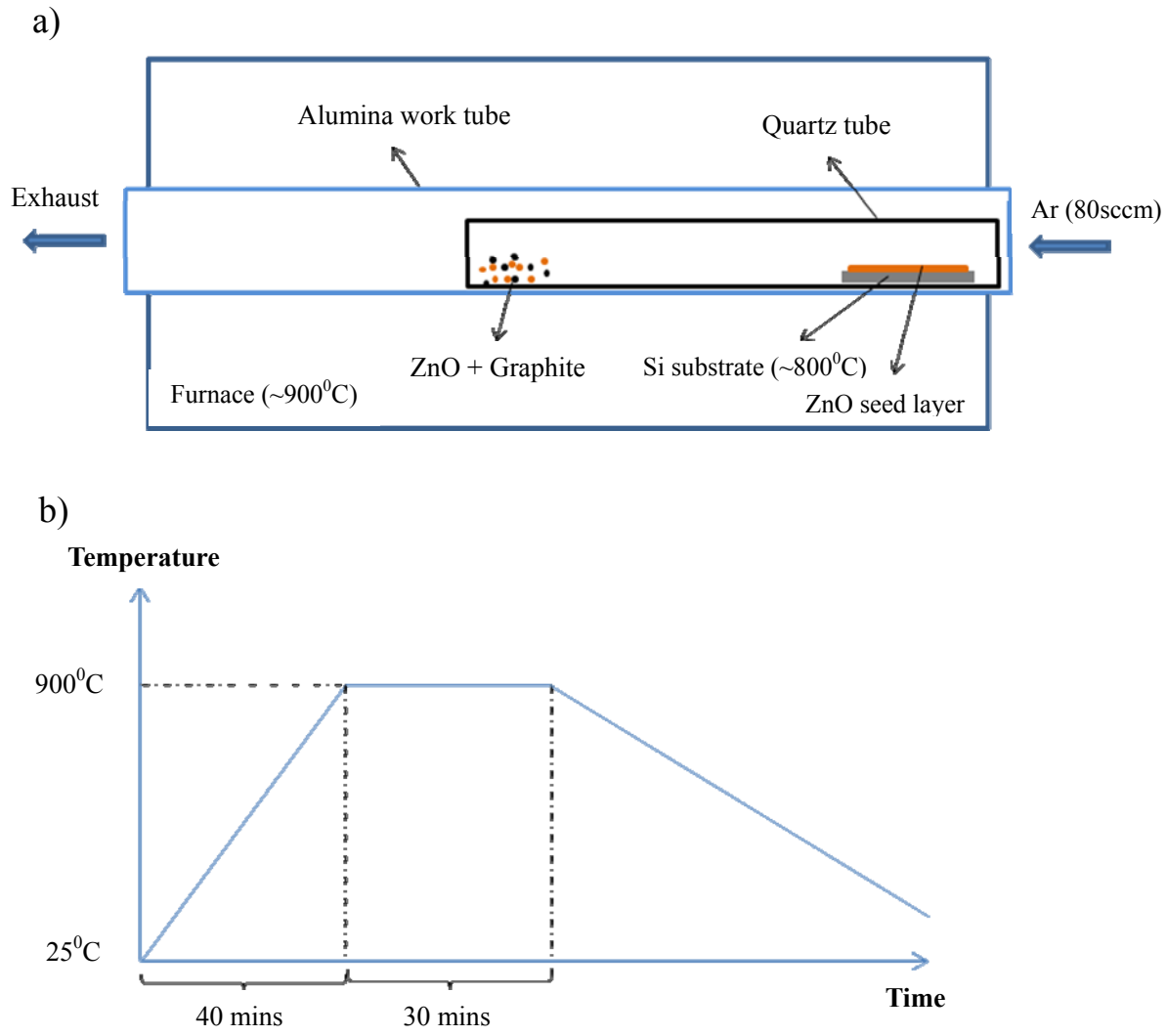

Figure A.1: (a) Schematic of ZnO NW growing setup, and (b) Temperature heating profile of the furnace

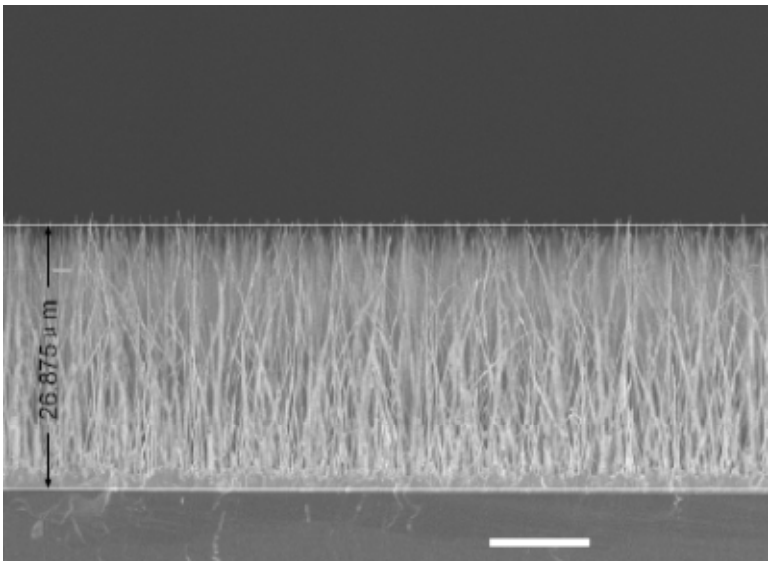

Figure A.2: Side view SEM image for vertical ZnO NW array. Scale bar is 10 µm

References

[A.1]. Deng, S. Z.; Fan, H. M.; Wang, M.; Zheng, M. R.; Yi, J. B.; Wu, R. Q.; Tan, H. R.; Sow, C. H.; Ding, J.; Feng, Y. P.; Loh, K. P.; "Thiol-Capped ZnO Nanowire/Nanotube Arrays with Tunable Magnetic Properties at Room Temperature", *ACSNano* Vol.4, pp. 495 – 505, 2010.

Appendix B: VO_2 NW synthesis and characterization

Single-crystalline VO_2 NWs were synthesized using a catalyst-free chemical vapor deposition route. The details of the material synthesis and characterization of the VO_2 NWs have been described elsewhere [B.1, B.2]. V_2O_5 powder (Sigma Aldrich) was used as source material in conversion-evaporation and condensation process to synthesize VO_2 wires. The synthesis was carried out in a horizontal tube furnace in flowing Ar carrier gas (99.9%). A porcelain boat loaded with V_2O_5 powder (~0.2 g) was kept inside a quartz tube of diameter ~1.5 cm. Cleaned <100> Si wafer (0.5 cm × 0.5 cm) were placed downstream inside a quartz tube ~ 1–3 cm away from the source powder. The quartz tube was loaded inside the ceramic tube of the furnace with the source powder at the high temperature zone. The ceramic tube was evacuated to a base pressure of 1×10^{-2} mbar before flowing Ar gas at a rate of 300 – 500 sccm and the pressure was regulated and maintained at ~ 2 mbar. The temperature of the furnace was ramped to ~ 870 ± 20°C at a rate of 20°C/min. The system was maintained at 870 ± 20°C for typically 1 – 2 hours before natural cooling to room temperature. Figure B.1a shows a schematic diagram of VO_2 NW growth via the conversion-evaporation and condensation process while the temperature profile of the tube furnace is shown in Figure B.1b. The growth of VO_2 NWs is seen to follow a vapor – solid route in which V_2O_5 undergoes evaporation and evaporative decomposition to various vanadium oxides at temperatures above 700^{o}C. Oxides which are unstable at the growth temperatures were carried downstream by the carrier gas, whereas the stable VO_2 re-crystallizes in the high temperature zone of the reaction tube. During temperature ramping and at the early state of the growth, the domain islands which seed the NW growth were formed on the Si substrate. At the growth temperature, more VO_2 vapor flux would be generated and deposited onto the

seed crystals to commence the growth of NW.

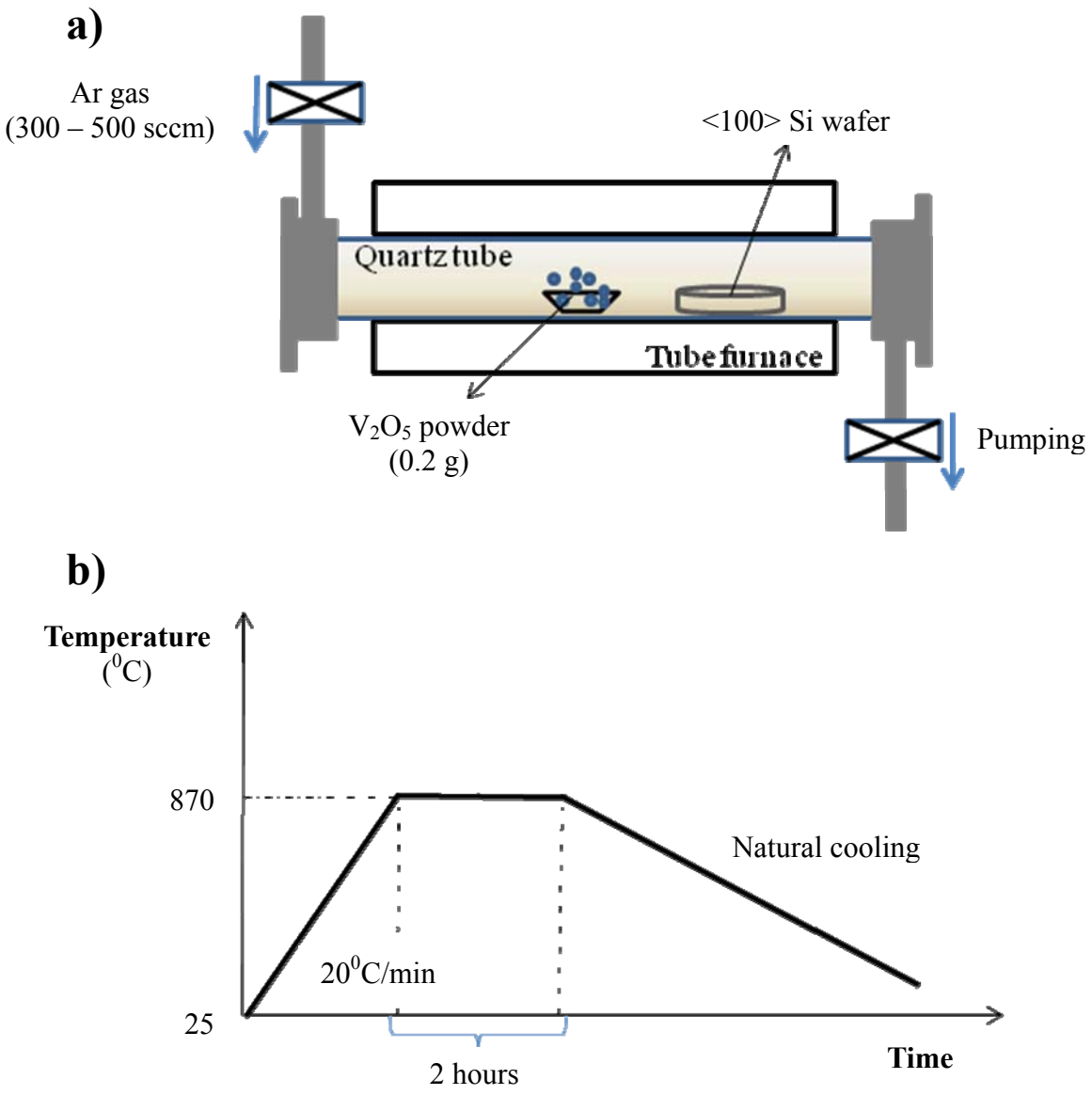

Figure B.1: (a) Schematic diagram of VO_2 NW growth in tube furnace, and (b) Temperature heating procedure of tube furnace.

The morphology of the VO_2 NWs was examined using scanning electron microscopy (SEM). Figure B.2 shows a representative SEM image of VO_2 NWs grown at 870^oC on Si substrate. The image shows that the NWs were predominantly straight with well-defined facets. The close-up SEM images (as shown in Figure B.2 inset) have further revealed that these as-synthesized VO_2 NWs also exhibit rectangular cross sections with smooth and well faceted side walls. The typical lateral sizes of the VO_2 NWs were in the range of 80 – 500 nm and the length of NWs was from few micrometers to few ten micrometers (5 – 30 μm).

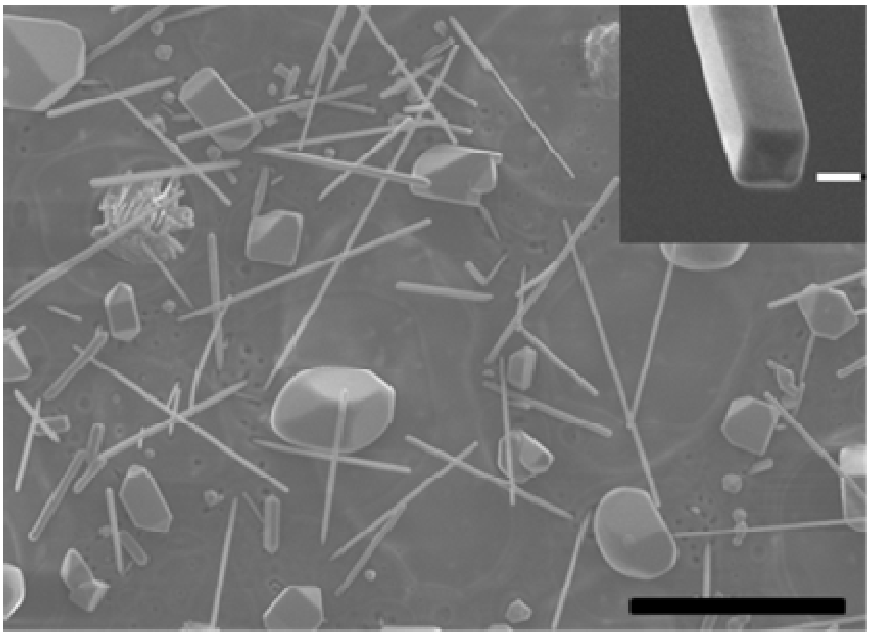

Figure B.2: SEM image of VO_2 NWs grown at 870^oC on Si substrate, scale bar: 10 μm. Inset: Close-up SEM image of a single VO_2 NW, scale bar: 300 nm.

The structure of the VO_2 NWs was further investigated using X-ray diffraction (XRD) [B.1]. The XRD pattern recorded at room temperature of the as-synthesized NWs grown on Si substrate is shown in Figure B.3. The peaks observed at $2\theta \approx 27.8^o$ and

57.5° in the XRD pattern are consistent with (011) and (022) Bragg reflection planes of the room temperature monoclinic structure of VO_2, respectively, which demonstrates clearly that the NWs are highly crystalline and preferentially oriented grown.

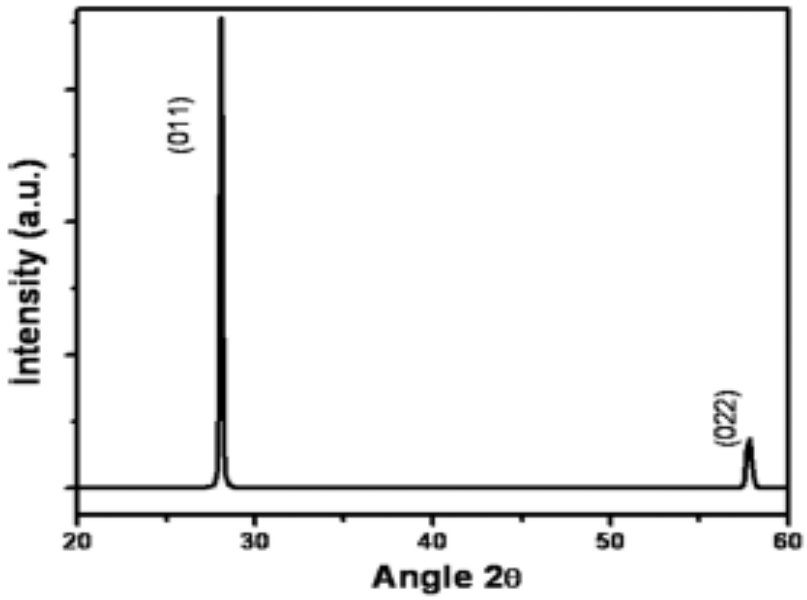

Figure B.3: X-ray diffraction pattern of as-synthesized VO_2 NWs showing highly crystalline structure and preferentially oriented growth [B.1].

References

[B.1]. Varghese, B.; Tamang, R.; Tok, E. S.; Mhaisalkar, S. G.; and Sow, C. H.; "Photothermoelectric effects in localized photocurrent of individual VO_2 nanowires", *J. Phys. Chem. C* Vol. 114, pp. 15149 – 15156, 2010.

[B.2]. Xie, R.; Bui, C. T.; Varghese, B.; Zhang, Q.; Sow, C. H.; Li, B.; and Thong, J. T. L.; "An electrically tuned solid-state thermal memory based on metal-insulator trasistion of single-crystalline VO_2 nanobeams", *Adv. Func. Mater.* Vol. 21, pp. 1602 – 1607, 2011.

Appendix C: Publications

I. Publications which are the outcome of the thesis

1. Cong-Tinh Bui, Rongguo Xie, Minrui Zheng, Qingxin Zhang, Chorng Haur Sow, Baowen Li, and John T. L. Thong, *Diameter Dependent Thermal Transport of ZnO Nanowires and its Correlation with Surface Coating and Defects*, **Small** DOI:10.1002/smll.201102046 (2011).

2. Rongguo Xie , Cong-Tinh Bui , Binni Varghese , Qingxin Zhang , Chorng Haur Sow , Baowen Li , and John T L Thong, *An Electrically Tuned Solid-State Thermal Memory Based on Metal–Insulator Transition of Single-Crystalline VO_2 Nanobeams*, **Advanced Functional Materials** 21, 1602 – 1607 (2011).

II. Related publications which are not part of the thesis

3. Ziqian Wang, Rongguo Xie, Cong-Tinh Bui, Dan Liu, Xiaoxi Ni, Baowen Li, and John T.L. Thong, *Thermal Transport in Suspended and Supported Few-Layer Graphene*, **Nano Letters** 11, 113-118 (2011).

4. Gang Zhang, Qingxin Zhang, Cong-Tinh Bui, Guo-Qiang Lo, and Baowen Li, *Thermoelectric Performance of Silicon Nanowires*, **Applied Physics Letters** 94, 213108 (2009).

5. Xiangfan Xu, Yu Wang, Kaiwen Zhang, Xiangming Zhao, Sukang Bae, Martin Heinrich, Cong-Tinh Bui, Rongguo Xie, John T. L. Thong, Byung Hee Hong, Loh Kian Ping, Baowen Li, Barbaros Ozyilmaz, *Phonon Transport in Suspended Single Layer Cu-CVD Graphene*, **International Conference on Materials for Advanced Technologies**, 26th Jun to 1st Jul 2011, Suntec City Convention Centre, Singapore.